BROOKHAVEN NATIONAL LABORATORY

December, 1989 BNL --43818

Hadron Production in Relativistic Heavy Ion Interactions and the search for the Quark-Gluon Plasma Course prepared for the Winter School on Quark-Gluon Plasma December 5-16, 1989 Puri, Orissa, INDIA

M. J. TANNENBAUM

Brookhaven National Laboratory
Upton, N.Y.11973

ABSTRACT

The course starts with an introduction, from the experimentalist's point of view, of the challenge of measuring Relativistic Heavy Ion interactions. A review of some theoretical predictions for the expected signatures of the quark gluon plasma will be made, with a purpose to understand how they relate to quantities which may be experimentally measured. A short exposition of experimental techniques and details is given including charged particles in matter, momentum resolution, kinematics and Lorentz Transformations, calorimetry. (Students may find it convenient use a book on experimental physics for reference.) Principles of particle identification including magnetic spectrometers, time of flight measurement. Illustrations using the E802 spectrometer and other measured results. Resolution smearing of spectra, and binning effects. Parent to daughter effects in decay, with $\pi^0 \rightarrow \gamma\gamma$ as an example.

The experimental situation from the known data in $p-p$ collisions and proton-nucleus reactions is reviewed and used as a basis for further discussions. The "Cronin Effect" and the "Seagull Effect" being two arcana

worth noting. Then, selected experiments from the BNL and CERN heavy ion programs are discussed in detail.

Examples of subjects to be covered include NA5 and NA35 calorimeters and E_T distributions. Beam line calorimeters and what they measure—WA80. Electromagnetic calorimetry and the systematics of E_T distributions in $p-p$, $p+A$, and $A+A$ reactions (AFS and R110; E802 and NA35). The fireball model and $dE_T/d\eta$; comparison to multiplicity density, $dn/d\eta$ measurements in emulsions (E808). Comparison to $p-p$ results. Summary of experimental situation with some discussion of popular theoretical models from a critical and skeptical viewpoint. Inclusive particle production in $p-p$, $p+A$ and $A+A$ interactions, systematics of the representation of these distributions as a function of P_T, m_T or a Boltzmann distribution.

The conlcusion will be view to the future: Heavy Beams and then on to RHIC.

Hadron Production in Relativistic Heavy Ion Interactions and the Search for the Quark-Gluon Plasma

M.J. TANNENBAUM
Brookhaven National Laboratory*
Upton, N.Y. 11973, USA

1. Introduction

High energy collisions of nuclei provide the means of creating nuclear matter in conditions of extreme temperature and density. At large energy density, or baryon density, a phase transition is expected from a state of nucleons containing confined quarks and gluons to a state of "deconfined" (from their individual nucleons) quarks and gluons covering the entire volume of nuclear matter, or a volume that is many units of the characteristic length scale. This state is expected to be in thermal and chemical equilibrium. In the terminology of high energy physics, this is called a "soft" process, related to the QCD confinement scale

$$\Lambda_{\rm QCD}^{-1} \sim (0.1 GeV)^{-1} \sim 2\, fm$$

This state is called the Quark-Gluon-Plasma (QGP)[1,2].

A schematic drawing of a relativistic heavy ion collision is shown in Figure 1. Two energy regimes are discussed for the QGP[3]. At lower energies, typical of the AGS, the colliding nuclei are expected to stop each other, leading to a Baryon-Rich system. This will be the region of maximum baryon density. At very high energy, 100 to 200 GeV per nucleon pair in the center of mass, the nuclear fragments will be well separated from a central region of particle production. This is the region of the Baryon-Free or Gluon plasma.

There has been considerable work over the past few years in making quantitative predictions for the QGP. A recent calculation of a phase diagram for "isentropic expansion trajectories for a hadronizing QGP" [4] is shown in figure 2. The transition temperature from a state of hadrons to the QGP varies, from $T_c = 140$ MeV at zero baryon density, to zero temperature at a critical baryon density ~ 6.5 times the normal nuclear density:

$$\rho_0 = 0.15\,\text{nucleons}/fm^3 \ .$$

Predictions for the transition temperature are constrained to a relatively narrow range $140 < T_c < 250\,$MeV, while the critical baryon or energy density is prediected to be 5 to 20 times the normal density[5].

From the point of view of an experimentalist there are two major questions in this field. The first is how to relate the thermodynamical properties (temperature, energy density, entropy...) of the QGP or hot nuclear matter to properties that can be measured in the laboratory. The second question is how the QGP can be detected.

* This research has been supported in part by the U.S. Department of Energy under Contract DE-AC02-76CH00016

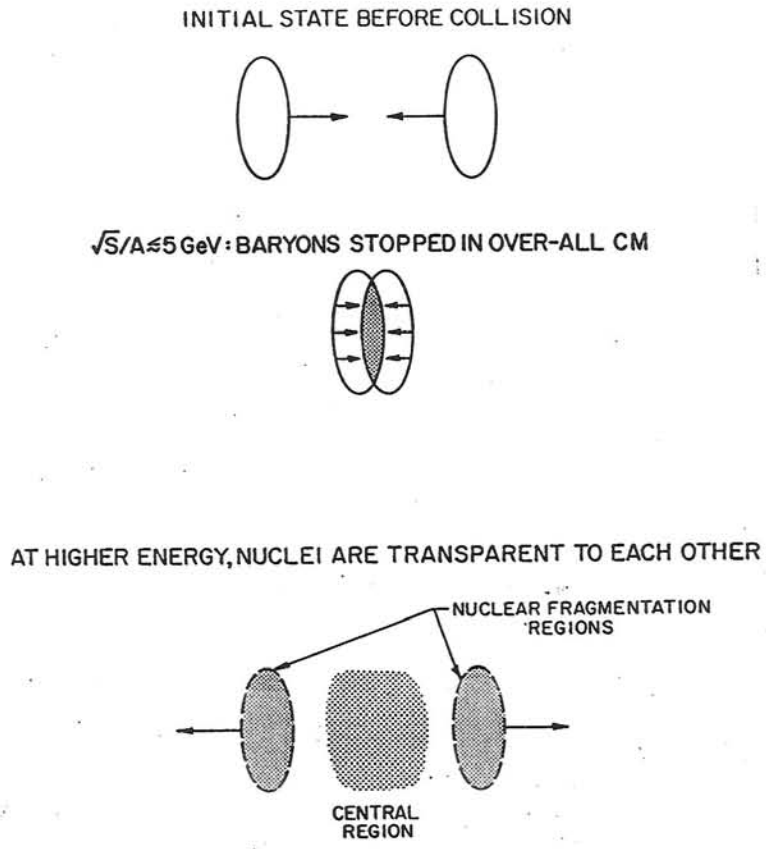

Fig. 1: Schematic of Relativistic Heavy Ion Collision from RHIC Conceptual Design Report BNL 51932(1986)

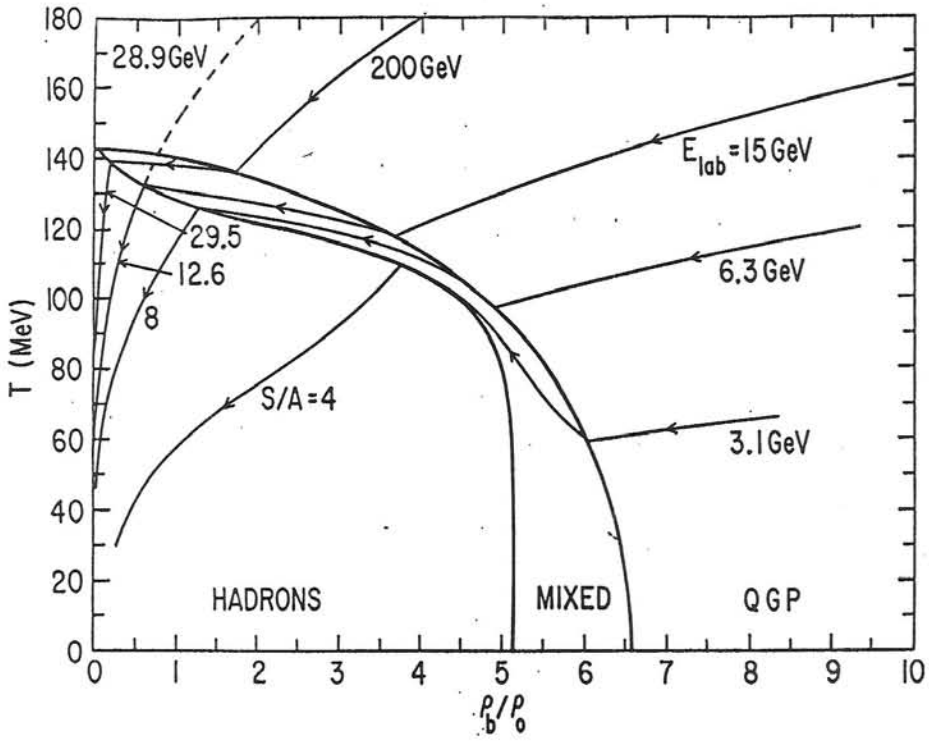

Fig. 2: Phase Diagram of nuclear matter from U. Heinz et al.[5]

2. Observables

The challenge of RHI collisions can be understood from Figure 3, which is a streamer chamber photograph of a 200 GeV/u oxygen projectile colliding with a lead nucleus[6]. It would appear to be a daunting task to reconstruct all the particles in such events. Consequently, it is more common to use single-particle or multi-particle inclusive variables to analyze these reactions.

A single particle inclusive reaction involves the measurement of just one particle coming out of a reaction. For any particle, the momentum can be resolved into transverse (p_T) and longitudinal (p_L) components; and in many cases the mass (m) of the particle can be determined. The longitudinal momentum is conveniently expressed in terms of the rapidity (y):

$$y = \ln\left(\frac{E + p_L}{m_T}\right) \tag{2.1}$$

$$\cosh y = E/m_T \qquad \sinh y = p_L/m_T \tag{2.2}$$

where

$$m_T = \sqrt{m^2 + p_T^2} \quad \text{and} \quad E = \sqrt{p_L^2 + m_T^2} \tag{2.3}$$

In the limit when ($m \ll E$) the rapidity reduces to the pseudorapidity(η)

$$\eta = -\ln\tan\theta/2 \tag{2.4}$$

$$\cosh\eta = \csc\theta \qquad \sinh\eta = \cot\theta \tag{2.5}$$

where θ is the polar angle of emission. The rapidity variable has the useful property that it transforms linearly under a Lorentz transformation so that the invariant differential single particle inclusive cross section becomes:

$$\frac{Ed^3\sigma}{dp^3} = \frac{d^3\sigma}{p_T dp_T dy d\phi} \tag{2.6}$$

where

$$dy = \frac{dp_L}{E}. \tag{2.7}$$

In the region near the projectile or target rapidity, the Feynman x fragmentation variable is also used:

$$x_F = 2p_L/\sqrt{s} \tag{2.8}$$

where $\sqrt{s}$ is the center-of-mass energy of the collision.

The transverse momentum distributions can be determined for the different particles, and typically the average transverse momentum, $< p_T >$ is taken as a measure of the temperature, T. The charged particle multiplicity, either over all space, or in resricted intervals of rapidity, is taken as a measure of entropy.

A convenient description of high energy collisions is provided by the charged particle density in rapidity, dn/dy. A classical measurement in a streamer chamber from $p-p$ collisions at the CERN ISR[7] is shown in figure 4. Regions of nuclear fragmentation take up the first 1-2 units around the projectile and target rapidity and if the center-of-mass energy is sufficiently high, a central plateau is exhibited. Another, similar variable is the transverse energy density in

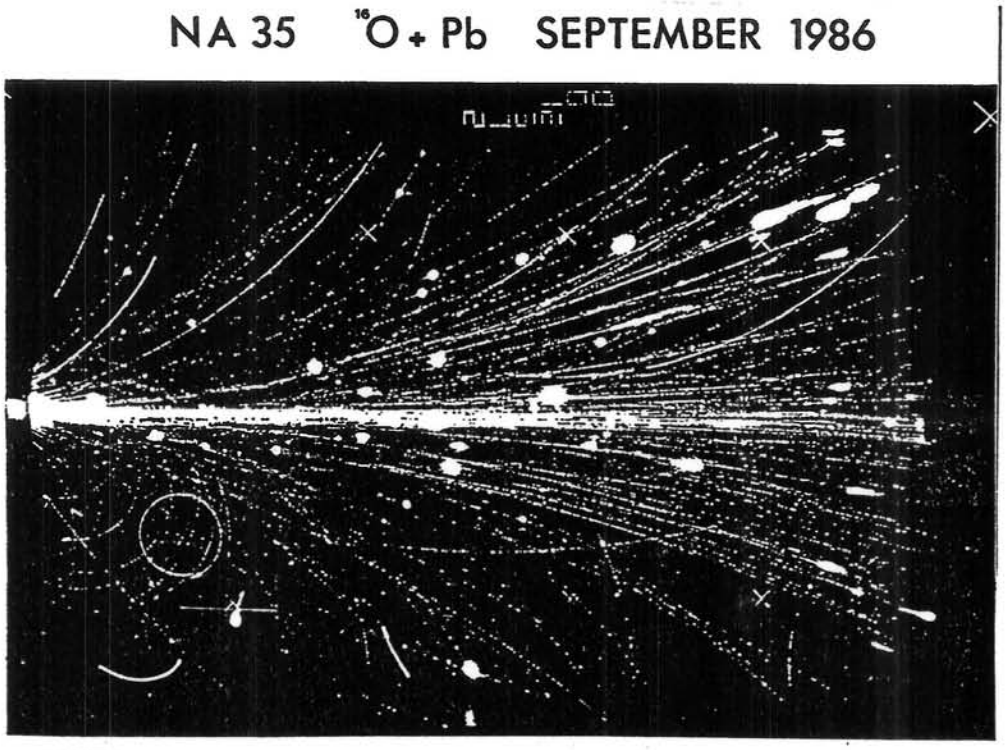

Fig. 3: Streamer chamber photograph[6] of a $^{16}O + Pb$ collision at 200 GeV/nucleon.

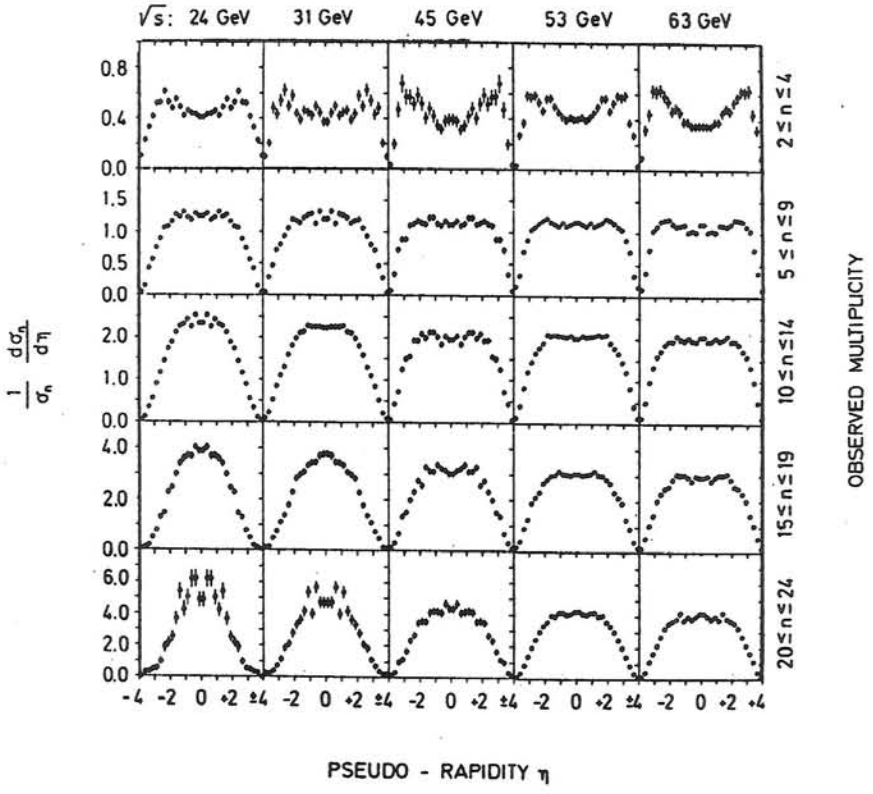

Fig. 4: Measurements in a streamer chamber at the CERN ISR of the normalized charged particle densities (corrected for acceptance up to $|\eta| \simeq 4$) in various intervals of the total observed multiplicity, as a function of the c.m. energy, $\sqrt{s}$, of the $p - p$ collisions [7].

rapidity or $dE_T/dy \sim < p_T > \times dn/dy$. This is thought to be related to the co-moving energy density in a longitudinal expansion, and according to Bjorken[7] is proportional to the energy density in space ϵ:

$$\epsilon_{Bj} = \frac{d < E >}{dy} \frac{1}{2\tau_0 \pi R^2} \tag{2.9}$$

where τ_0, the formation time, is usually taken as 1 (or $\frac{1}{2}$!) fm, πR^2 is the effective area of the collision, and $d < E > /dy$ is the co-moving energy density.

3. Signatures of the Quark-Gluon Plasma

One of the more interesting signatures proposed for the QGP is that it could trigger a catastrophic transition from the metastable vacuum of the present universe to a lower energy state[9], " a possibility naturally occurring in many spontaneously broken quantum field theories " . A more likely outcome is that the existence of the QGP will be inferred from a comprehensive and systematic set of experimental data exhibiting several striking features or "anomalies", "which can be interpreted in a unified way as manifestations of QGP production" [10]. Examples of the features expected for the QGP and signatures to find them are given below:

a) Characteristic Temperature Entropy Curve[11]:

Note that this curve (Figure 5) has the features of a phase transition with which we are all familiar. The $< p_T >$, acting as temperature, increases with increasing entropy (dn/dy); then as the phase transition takes place (e.g. water changing to steam) the temperature remains constant and begins rising again when the transition to the new phase is complete.

b) Plasma Droplets Caused by Deflagration[12]:

These would be manifested by large fluctuations in dn/dy or dE_T/dy covering a range of $\sim$1 unit on an event by event basis. The hope would be to observe the other plasma signatures only in the region of the fluctuation and not in the other regions.

c) Thermal Equilibrium :

One of the best probes of thermal equilibrium is lepton pair production[13]. There are two characteristic features of thermal production of lepton pairs. The number of lepton pairs per unit of rapidity is proportional to the square of charged particle density, and furthermore this ratio is proportional to the transition temperature T_c :

$$\frac{dN_{e^+e^-}\left(m_{ee} > 200MeV\right)/dy}{\left[dn/dy\right]^2 \times 10^{-7}} \simeq 15\, T_c\,(GeV)$$

Also, the p_T and mass dependence of the cross section are not independent but depend only on the transverse mass m_T. This means that at any fixed value of m_{ee}, the $< p_T\,(m_{ee}) >$ is linearly proportional to m_{ee}.

d) Volume of Thermal Matter :

The size of the thermal source is thought to be measured by identical particle interferometry using the GGLP effect[14]. When two identical pions occupy nearly the same coordinates in phase space, the amplitudes interfere constructively due to the symmetry of the wave-function imposed by Bose-Einstein statistics. The characteristic momentum difference leading to decorrelation in momentum space can be measured, and is taken to be the fourier transform of the size of an extended source in position space. It should be noted that dynamical effects due to final state

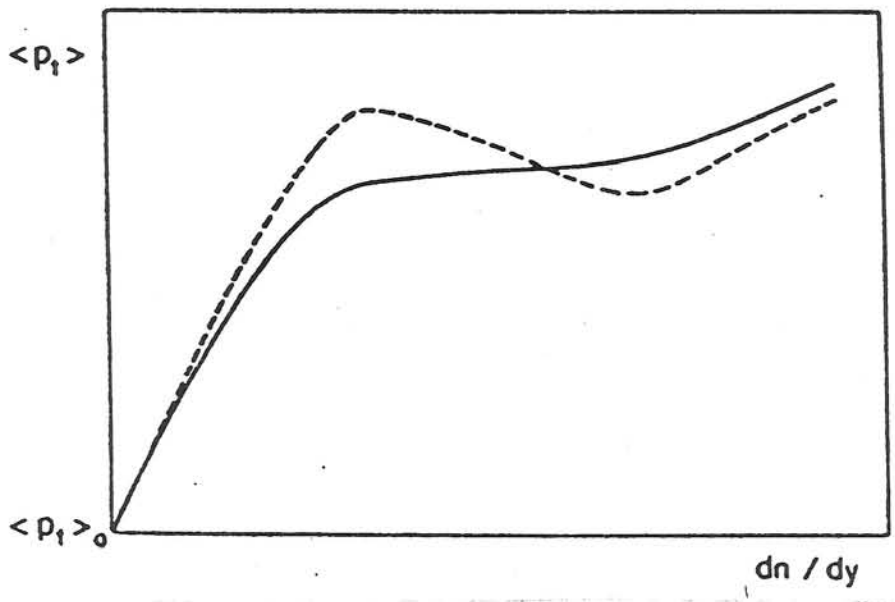

Fig. 5: Characteristic Temperature-Entropy Curve for phase transition[11]

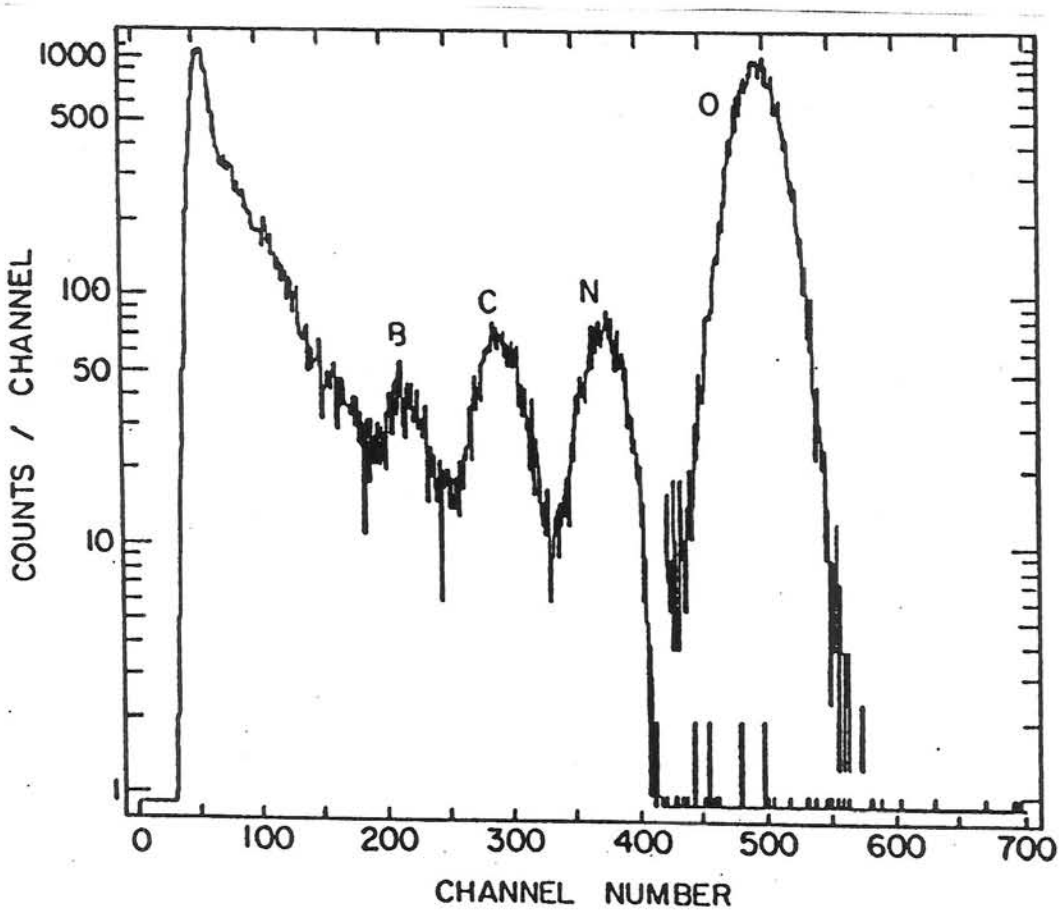

Fig. 6: Spectrum in Bullseye Counter from AGS-E802. The $^{16}_{8}O$ peak is obtained from a sample of non-interacting beam particles, and superimposed onto the spectrum for a detected interaction.

interactions can be large, and make the interpretation of such measurements a very specialized subject[15].

e) Chemical Equilibrium[16,17]:

In the QGP there will be gluons, quarks and anti-quarks. They will continuously react with each other via the QCD subprocesses:

$$g\,g \rightarrow q\,q \qquad q\,q \rightarrow g\,g \qquad q\,q \rightarrow q'\,q'$$

where q' represents a different flavor quark (u, d or s). After several interactions have taken place, the reaction rates and the abundances of the gluons and the different flavor quarks (and anti-quarks) will become equilibrated, so that they no longer change with time. This is called chemical equilibrium. Since the transition temperature T_c is comparable to the strange quark mass ~150 MeV, the strange quarks $s, \bar{s}$ should have the same abundance as the $u, \bar{u}$ and $d, \bar{d}$ in the gluon plasma. In the baryon-rich plasma, the $s, \bar{s}$ will be enhanced compared to u and d, since $u, \bar{u}$ and $d, \bar{d}$ are "Pauli" blocked by valence u and d quarks.

The principal probe of chemical equilibrium is the particle composition. For instance, the abundance of strange mesons and baryons as well as anti-baryons should be quite different in a QGP than in a hadron gas or in an ordinary nuclear collision

f)Deconfinement :

It has been proposed[18] that J/Ψ production in A+A collisions will be suppressed by Debye screening of the quark color charge in the QGP. The J/Ψ is produced when two gluons interact to produce a $c, \bar{c}$ pair which then resonates to form the J/Ψ. In the plasma the $c, \bar{c}$ interaction is screened so that the $c, \bar{c}$ go their separate ways and eventually pick up other quarks at the periphery to become *open charm*. This would be quite a spectacular effect since the naive expectation is that J/Ψ production, being a pointlike process, should go like $A \times A$ in an A+A collision, and thus would be enhanced relative to the total interaction cross section, which increases only as $A^{2/3}$.

Another signature of deconfinement has recently been proposed[19]. If one could start off with a correlated two-quark object ("diquark") which then becomes deconfined due to the the formation of a QGP, the predictions of the effect of Debye screening should contain fewer uncertainties than in the case of J/Ψ suppression. It is suggested that the proton is composed of a quark-diquark bound system and that proton production at large transverse momenta in $p-p$ collisions is the result of hard scattering of diquarks. Hence, a **decrease** in the yield of protons and other baryons at large transverse momenta is predicted, in the case of QGP production, which should be directly related to the deconfinement of diquarks due to Debye screening. It is argued that such an effect is not likely to occur in dense hadronic matter. However, there is also the possibility[20] that a system of diquarks may be the preferred configuration of quark matter at temperatures and densities just above the deconfinement transition. This may lead to a diquark enhancement and an *increase* in large p_T baryon production... Clearly this subject quite interesting and requires further analysis.

4. Relation to Experimental Techniques

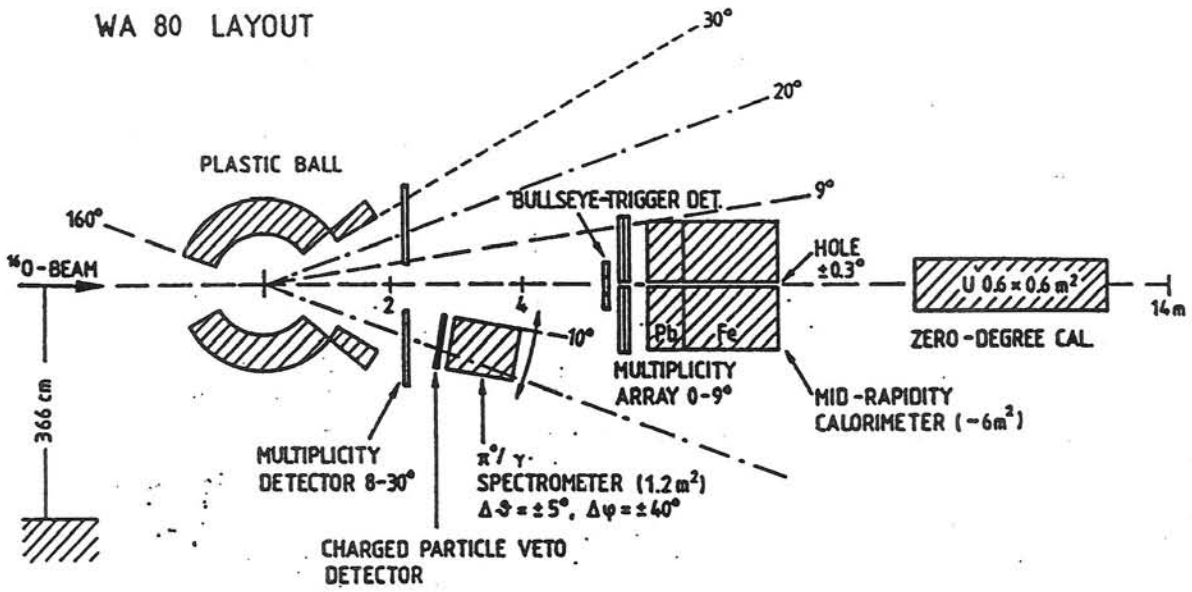

Experiment WA80: Study of Relativistic Nucleus-Nucleus Collisions at the CERN SPS

Fig. 7: WA80

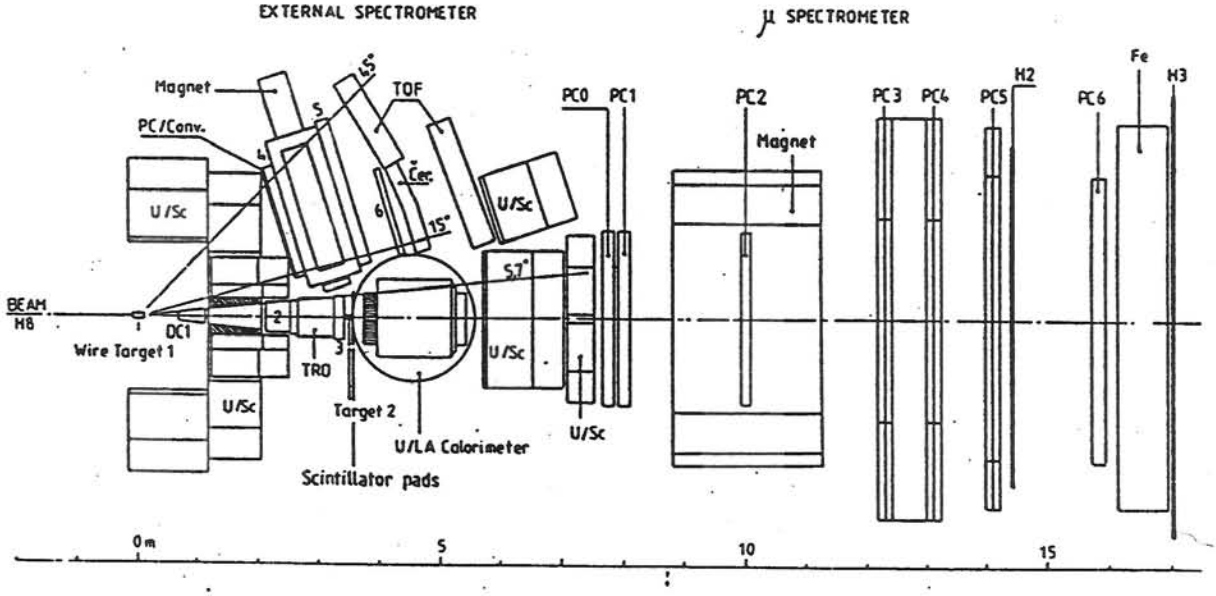

Experiment NA34/2: Study of High Energy Densities over Extended Nuclear Volumes via Nucleus-Nucleus Collisions at the SPS

Fig. 8: NA34

Each of the probes of the QGP tends to have a different experimental technique associated with it. In all cases the multiplicities in nuclear collisions are so large that all the detectors used are very highly segmented. For measuring the charged multiplicity or dn/dy, a segmented multiplicity detector is used, usually an array of proportional tubes with pad readout, or a silicon pad array. For measuring transverse energy flow, dE_T/dy, a hadron calorimeter is used. Some groups use an electromagnetic shower counter for this purpose. This has the advantage of being smaller, cheaper and higher in resolution than a full hadron calorimeter; but has the disadvantage of being biased, since only π^0 and η^0 mesons are detected (via their two photon decay). Nuclear fragmentation products are detected by calorimeters in the projectile direction and by E, dE/dx scintillator arrays in the target fragmentation region. The particle composition and transverse momentum distributions are measured using magnetic spectrometers with particle identification. Typically, time-of-flight, gas and aerogel Cerenkov counters, and dE/dx are used to separate pions from kaons, protons, deuterons, etc. Drift chambers are generally utilized for charged particle tracking, although streamer chambers and time projection chambers (TPC) are also in use. Lepton pair detectors are very specialized, and usually combine magnetic spectrometers with lepton identification (muons by penetration, and electrons by "gas" and "glass").

One of the specific problems in this field is how to detect, with minimum bias, when a nucleus-nucleus collision has taken place. Two techniques are used. The first is to put a calorimeter at zero degrees to determine whether the projectile has the full beam energy or has lost some energy. The second uses a so-called bullseye counter downstream of the target, sized just large enough to detect all the beam particles. The bullseye also measures the charge of the beam particles since the pulse height is proportional to Z^2. If a particle misses the bullseye, or the charge changes, this is taken as an indication of a nuclear interaction (see Fig. 6).

With that quick overview of the experimental techniques, the following "photo album" of the first round of experiments at CERN and Brookhaven should be easier to comprehend. The CERN heavy ion program has provided ^{16}O and ^{32}S beams at 60 and 200 GeV/u and will possibly improve the source to provide ^{207}Pb beams. There are 5 major experiments: WA80 (Figure 7), NA34 (Figure 8), NA35 (Figure 9), NA36 (Figure 10), and NA38 (Figure 11). The BNL heavy ion program has provided ^{16}O and ^{28}Si beams at 14.6 GeV/c per nucleon and is scheduled to accelerate ^{197}Au beams to 11.7 GeV/c per nucleon in 1992. A major improvement is planned for 1996 when the Relativistic Heavy Ion Collider (RHIC) is scheduled to begin operation. RHIC will provide colliding beams, covering the full mass number spectrum, with center-of-mass energies from 5 to 200 GeV per nucleon pair. At present, there are 3 major RHI experiments at the BNL-Tandem-AGS: E802 (Figure 12), E810 (Figure 13) and E814 (Figure 14).

5. Some Details of Experimental Technique and Analysis

Although it is beyond the scope of these lectures to give a full course in experimental physics, a few topics will be mentioned here which will be of use for the detailed discussions of the experimental results to follow.

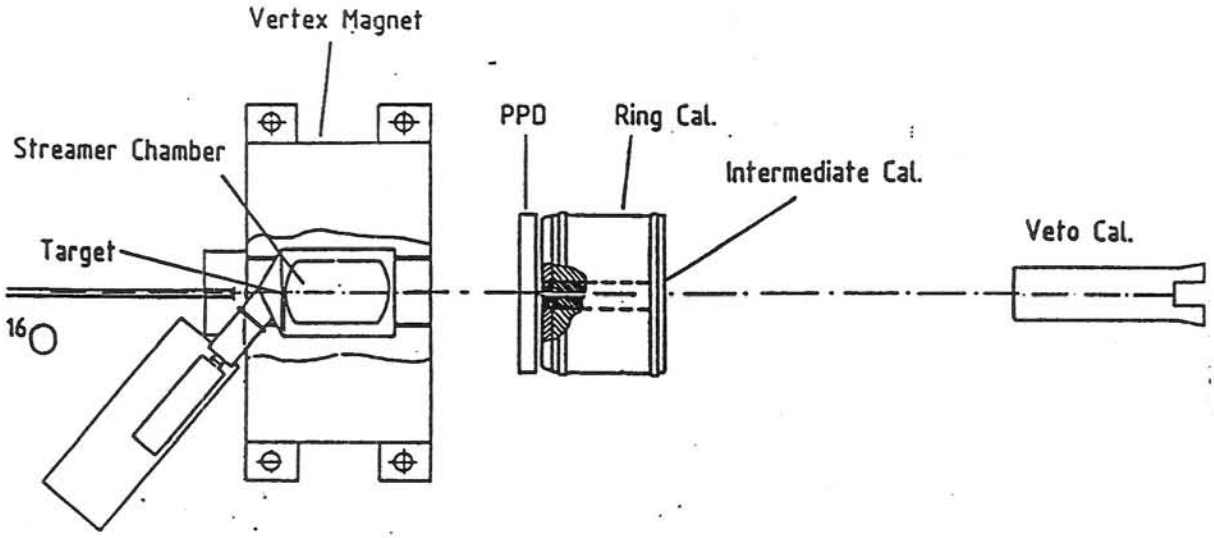

Experiment NA35: Study of Relativistic Nucleus-nucleus Collisions

Fig. 9: NA35

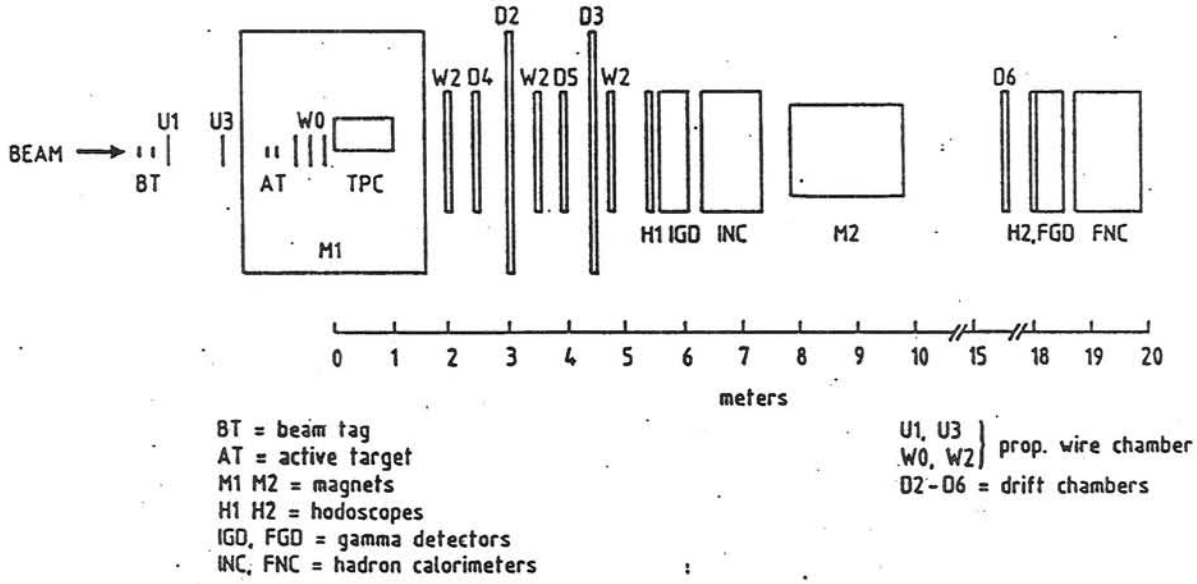

Exepriment NA36: Production of Strange Baryons and Antibaryons in Relativistic Ion Collisions

Fig. 10: NA36

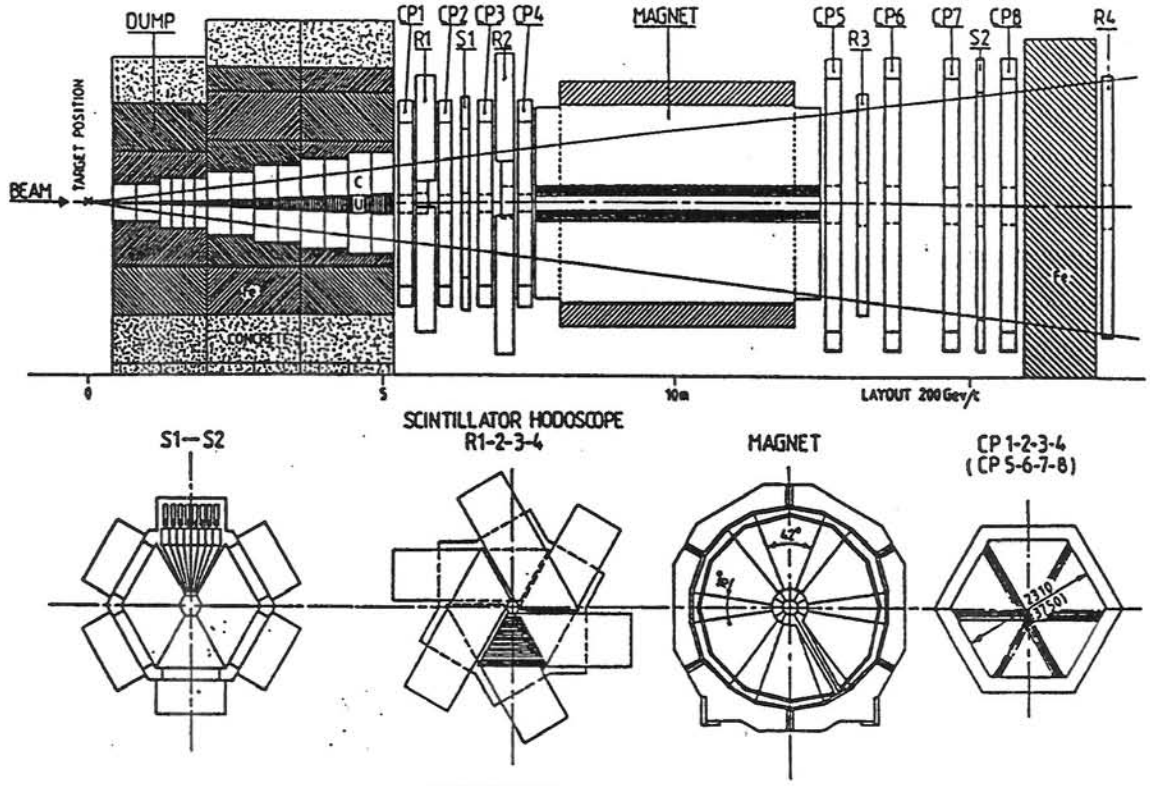

Fig. 11: NA38—Study of High-Energy Nucleus-Nucleus Interactions with the Enlarged NA10 Dimuon Spectrometer

BNL-TANDEM-AGS PROGRAM

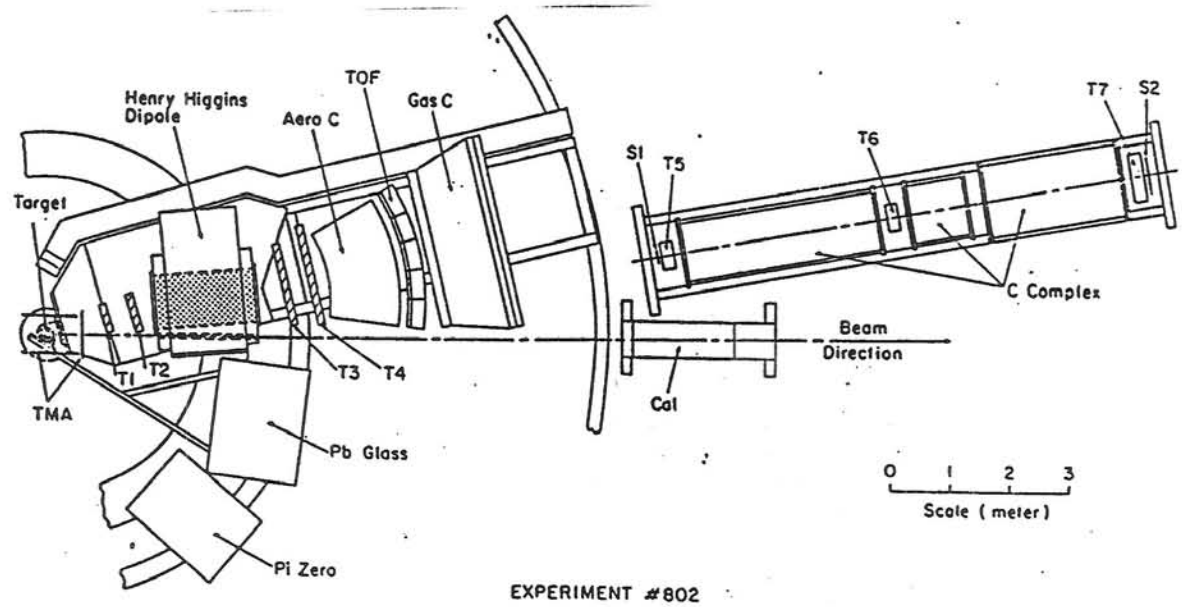

Fig. 12: E802—Studies of Particle Production at Extreme Baryon Densities in Nuclear Collisions at the AGS

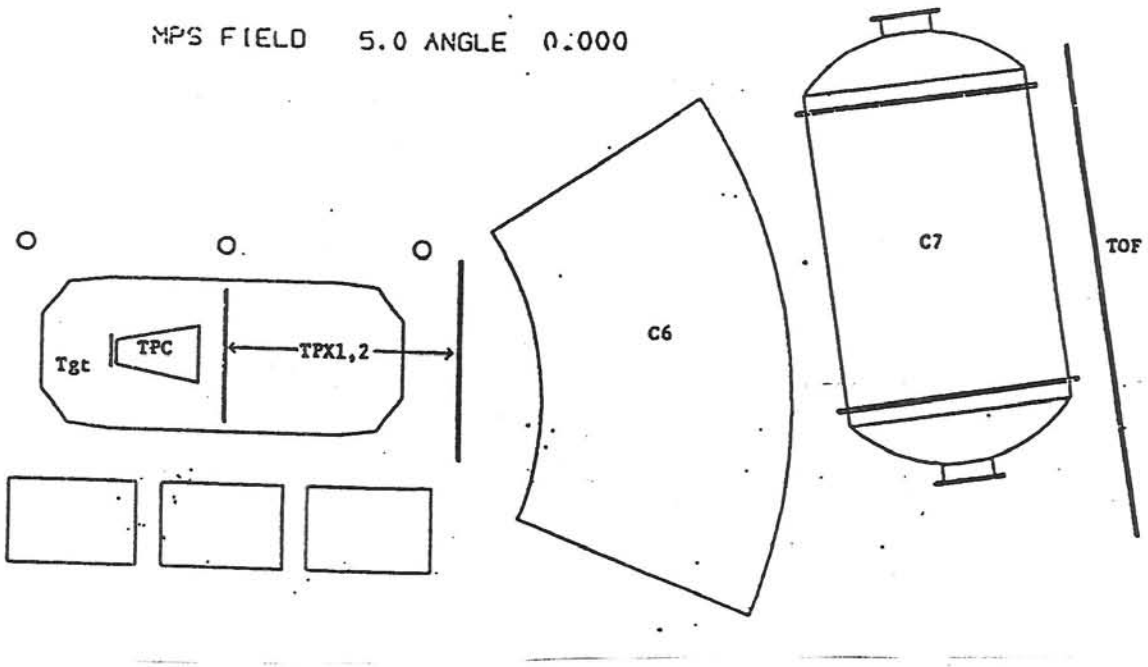

Fig. 13: E810—A Search for Quark Matter (QGP) and other New Phenomena Utilizing Heavy Ion Collisions at the AGS

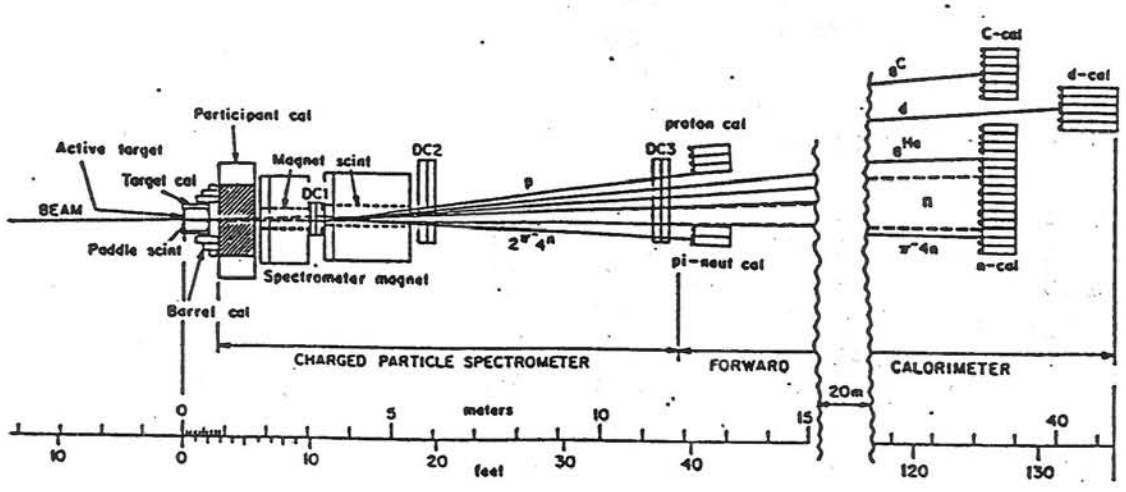

Fig. 14: E814—Study of Exotic Nuclear States Via Coulomb or Diffractive Projectile Excitation

5.1 Passage of charged particles through matter

The electric charge of a particle passing through matter[21] causes an electromagnetic force to be exerted on the atomic electrons of the material and causes them to be ejected from the atom, or **ionized**. The energy gained by the ions is lost by the incident particle, which slows down as it passes through matter, leaving a wake of ion-pairs in its path. Detection of these ion-pairs forms the basis of most charged particle detectors.

This is true for all particles except high energy electrons, which are so light that they essentially lose all their energy by radiation (Bremsstrahlung) due to interaction with the highly charged target nuclei. The probability for an electron of energy E to emit a photon of energy k, in range dk in passing through a thickness of material x is:

$$d\mathcal{P} = \frac{x}{X_o}\frac{dk}{k} \times F(k/E) \tag{5.1}$$

For thin radiators,

$$F(k/E) = \left[1 + (1-k/E)^2 - \frac{2}{3}(1-k/E)\right] \simeq 1,$$

so that the energy lost by electrons per unit length of material to photon emission can be written

$$-\frac{dE}{dx} \equiv k\frac{d\mathcal{P}}{dx} \simeq \frac{\int_0^E dk}{X_o} = \frac{E}{X_0}. \tag{5.2}$$

From this equation, it is clear that the **radiation length,** X_o is the length over which the energy of an incident electron is degraded to a fraction $1/e$ of its original value. The radiation length is inversely proportional to Z^2, where Z is the atomic number (nuclear charge) of the medium, and X_o is usually tabulated in units of $gm\ cm^{-2}$ (strictly $\rho \times X_o$ where ρ is the density of the medium). The **critical energy** of a medium is defined as the energy of elctrons for which dE/dx by ionization loss and radiation are equal. Thus, for electrons above the critical energy, typically 10 to 40 MeV, the dominant source of energy loss is by radiation.

For heavier particles (starting with the muon) ionization loss is predominant (until the TeV regime). The rate of this loss is given by the Bethe-Bloch formula, which takes the form of a kinetic factor which depends only on the velocity of the incident particle, $\beta = v/c$, times another factor with a slight β and $\log Z$ dependence:

$$\frac{-dE}{dx} = \frac{D\, n_e\, Z_p^2}{\beta^2}\mathcal{F}(\beta, \ln Z)\ ,$$

where D is a constant. The important features of the ionization loss are that it depends on the square of the charge of the incident particle Z_p, and linearly on n_e the number of electrons per unit volume in the target, because it is the result of coulomb scattering of the incident particle by the atomic electrons in the target. Apart from the dominant $1/\beta^2$ dependence, the ionization loss is slowly varying, with a broad minimum; and it is usually sufficiently accurate to represent the ionization loss of an incident particle of charge Z_p, invariant mass m and momentum P as:

$$\frac{-dE}{dx} = \left[1 + \left(\frac{mc}{P}\right)^2\right] \times Z_p^2 \times \frac{dE}{dx}\Big|_{\text{min}} \tag{5.3}$$

Thus, for fixed momentum, heavy particles have a larger ionization loss. As the momentum becomes much larger than the mass of the particle, the ionization loss reduces to a constant

value for all particles, represented as the charge of the particle squared times $dE/dx|_{\rm min}$, the **minimum ionization** for singly charged particles, which is typically 1 to 2 MeV/$gm\ cm^{-2}$.

In contrast to the elastic scattering of the incident particle by the atomic electrons in a medium, which results in significant energy transfer due to the light mass of the atomic electrons, elastic scattering of the incident particle by the highly charged atomic nuclei results in negligible energy transfer, since the nuclei are heavy. However the incident particle suffers a very large number of very small angle Coulomb elastic scatterings with the target nuclei, in passing through a medium, resulting in a smearing of the angles of the incident particles by a random walk process, **Multiple Scattering**. The angular distribution for small angle scattering is given by the famous Rutherford formula, from which the mean squared scattering angle can be derived. After passing through a thickness x of material, the root mean squared multiple scattering angle in space (polar angular deflection) of a particle of momentum P, velocity β is:

$$\theta|_{\rm rms} = \sqrt{<\theta^2>} = \frac{21.1 MeV/c}{(P\beta)} Z_p \sqrt{\frac{x}{X_o}} \tag{5.4}$$

Note that the multiple scattering increases as the square root of the number of radiation lengths (X_o) traversed. Although multiple scattering has nothing to do with radiation, the fact that the medium dependence of both processes scales as the number of radiation lengths is because both are Coulomb interactions with the target nuclei.

5.2 Strongly Interacting Particles—hadrons

In addition to the electromagnetic interactions which predominate in the target, an incident hadron may also suffer an occasional nuclear interaction. This is usually represented by a **nuclear interaction length** λ_I. For an interaction cross section σ_I, the probably of suffering a nuclear interaction in a thin slab of material is just the interaction cross section (cm^2) times the number of target nuclei per cm^2 presented by the slab of material. If the thickness is x, measured in $gm\ cm^{-2}$, where $x = t \times \rho$, t is the thickness of material in cm, and ρ is the density of the material in $gm\ cm^{-3}$, then

$$\mathcal{P} = \sigma_I \times \frac{N_o \rho t}{A} \equiv \frac{x}{\lambda_I}$$

so that

$$\frac{1}{\lambda_I} = \frac{N_o \sigma_I}{A} \tag{5.5}$$

and λ_I is in $gm\ cm^{-2}$. Here N_o is Avogadro's number, the number of atoms per A grams of material of atomic weight A, and $\frac{N_o \rho t}{A}$ is the number of atoms per cm^2 in the slab of material. Note that nuclear interaction lengths are usually tabulated for incident nucleons. When an incident nucleus is involved, experimenters should usually check the computation themselves.

5.3 Passage of photons through matter

Photons are uncharged, and so do not have any long range electromagnetic forces. Thus, photons do not suffer ionization loss or multiple scattering when passing through a material. However, photons couple directly to electric charge with a "pointlike" coupling. Thus, when a photon does interact, it is usually catastrophic, resulting in the absorption or loss of the

photon. The three major electromagnetic processes via which photons interact in matter are: photoelectric effect and Compton scattering with the atomic electrons; and pair production from the highly charged nuclei. For energies below $\sim 1\,MeV$, the atomic phenomena are dominant and photons are strongly absorbed in material, with the absorbtion being inversely proportional to the energy: the lower the energy, the stronger the absorption. Above a few MeV, photopair production becomes dominant, with a cross section that increases logarithmically with the photon energy until **complete screening** by the atomic electrons sets in and the cross section saturates. The interplay of these phenomena has the experimentally important consequence that photons of energies near the critical energy, typically 5 to 30 MeV, have the minimum absorption in matter, and thus can travel relatively long distances in a solid medium. Many of the troublesome mysterious backgrounds (or *albedo*) in experiments are caused by these photons near the critical energy, for which detectors are relatively transparent.

For high energy photons, the pair production process is very strongly related to the Bremsstrahlung process for high energy electrons. The probablilty of a high energy photon to pass through a thickness x of material without undergoing pair production[22] is

$$\mathcal{P}_{\rm NC} = \exp\left(-\frac{7}{9}\frac{x}{X_o}\left[1-\zeta\right]\right) \tag{5.6}$$

where $\mathcal{P}_{\rm NC}$ is the nonconversion probability, X_o is the radiation length, and $\zeta \lesssim 0.05$. Here the radiation length comes in because radiation and pair production are really just two aspects of the same process.

5.4 Electromagnetic Showers, Electromagnetic Calorimeters

In actual fact the concept of single Bremsstrahlung or pair production is only valid for very thin radiators or converters, $x \ll X_o$. For thick radiators, $x \gtrsim 10X_o$, an electromagnetic cascade shower develops. An incident photon converts into an e^+e^- pair, then each member of the pair radiates photons, these photons in turn convert, making more electrons, etc. At first the number of electrons in the shower increases with the depth, and then decreases roughly exponentially. The total depth of the shower increases logarithmically with the energy. It is as if the incident electron or photon gets converted by radiative processes into electrons and positrons at the critical energy, which then stop radiating and lose the rest of their energy by ionization. The measurement of electromagnetic showers forms the basis of high resolution electron and photon detectors, or in today's jargon, **Electromagnetic Calorimeters.**

There are two classes of shower counters: sampling or total absorption. In a sampling counter, layers of high Z plates such as Pb or U create the showers, and the ionization is detected or sampled in layers of active material such as liquid argon or plastic scintillator. In a total absorption shower counter (TASC) there is only one high Z medium which both creates the showers and detects them. The showers are detected either by scintillation or Cerenkov light. The most popular scintillating TASC are made of NaI or CsI. These counters have the best energy resolution and are used over the range from keV to TeV photons. A much cheaper, and hence very popular, TASC is the Lead Glass (PbGl) Cerenkov counter. Lead Glass for particle detection contains $\sim 55\%$ PbO by weight, or about twice that of high quality crystal used in glassware and chandeliers. The radiation length of Lead Glass (SF-5) is about 2.4 cm,

the critical energy is 15.8 MeV and the index of refraction is 1.67. The electrons in the shower are detected by Cerenkov radiation. The number of Cerenkov photons per unit length saturates very quickly for particles above the threshold $\beta_t = 1/n = 0.6$ so that electrons at the critical energy travel to the end of their range while emitting a constant amount of Cerenkov radiation per unit length.

An extimate of the energy resolution of a PbGl counter can be made by assuming that the incident electron or photon of energy E gets converted into electrons at the critical energy E_c, which then each emit a constant amount of Cerenkov light, represented by n_C detected Cerenkov photons, in coming to the end of their range. In this simple model, all fluctuations are ignored except in the statistics of the total number N of detected Cerenkov photons:

$$N = n_C \times \frac{E}{E_c}$$

Then,

$$\frac{\sigma_E}{E} = \frac{1}{\sqrt{N}} = \sqrt{\frac{E_c/n_C}{E}} = \frac{\sqrt{0.0158GeV\,/n_C}}{\sqrt{E\,(GeV)}} = \frac{13\%/\sqrt{n_C}}{\sqrt{E\,(GeV)}}$$

The actual energy resolution of clear Lead Glass, where absorption of the Cerenkov photons is not important is (in r.m.s)

$$\frac{\sigma_E}{E} = \frac{4\%}{\sqrt{E\,(GeV)}}$$

implying a few detected Cerenkov photons per critical energy electron. In real life, lead glass gets radiation damaged and turns brown...

5.5 Hadron Calorimeters

At sufficiently high energies, $\gtrsim 10$ GeV, hadron interactions in thick absorbers $x \gg \lambda_I$ create cascade showers. At these high energies, multiparticle production dominates inelastic hadron reactions. Thus, a shower develops as an incident hadron suffers an inelastic interaction, many new hadrons are produced, they in turn interact, etc. (It is interesting to point out here that multiple hadron interactions inside a nucleus do not in general produce cascade showers and this is an important difference in the microscopic and macroscopic physics of hadron interactions with nuclei). Hadron showers are not nearly as elegant as electromagnetic showers and in general the fluctuations are much worse. The typical resolution for a hadron calorimeter[23] is:

$$\frac{\sigma_E}{E} = \frac{64\%}{\sqrt{E\,(GeV)}}$$

Also, since the nuclear interaction length of most materials is much longer that the radiation length, hadron calorimeters tend to be very large objects.

6. Measurement of the Momentum of a Charged Particle

The previous discussion on the intertactions of charged particles in matter led to the method of **energy** measurements of electrons, photons, and hadrons by total absorption counters or calorimeters. The **momentum** of charged particles is more conventionally measured by a magnetic spectrometer.

A particle with charge e momentum P in a uniform magnetic field B undergoes uniform circular motion with radius:

$$r = \frac{P\,c}{e\,B}.$$

In practical units, r=3 meters for P=1 GeV/c and B=1.111... Tesla, for unit charged particles like those encountered by particle physicists. This is the principle of particle accelerators and solenoidal magnetic spectrometers: once the B field is given, the momentum determines the radius (or vice versa). In fixed target experiments, a magnetic spectrometer usually takes the form of a magnet with a rectangular shaped field region (see figure 15). The magnetic field deflects the charged particle, and the momentum is determined from the measured deflection. Taking the z direction, normal to the face of the magnet, and the magnetic field in the y direction, the particle deflection is in the $x-z$ plane, the plane of the drawing of figure 15. The vector equation:

$$\mathbf{F} = \frac{d\mathbf{P}}{dt} = \frac{e}{c}\mathbf{v}\times\mathbf{B}$$

leads to no change in the y component of momentum since B is in the y direction but leads to the coupled equations for P_x and P_z the x and z components of momentum:

$$\frac{dP_x}{dt} = -\frac{e}{c}v_z\,B_y \qquad \frac{dP_z}{dt} = \frac{e}{c}v_y\,B_z$$

Since B acts perpendicular to the momentum, the magnitide of the momentum is conserved, so it is sufficient to integrate the x–component equation:

$$\Delta P_x = -\frac{e}{c}\int_{\text{traj}} B_y\,v_z\,dt = -\frac{e}{c}\int B\,dz \tag{6.1}$$

This leads to the usual description of a magnetic spectrometer as having a transverse momentum kick $= \int B dz$=300 MeV/c per Tesla meter, for unit charged particles. For highly charged particles, this quantity is simply multiplied by Z_p (i.e. $Z_p\times$ 300 MeV/c per Tm).

6.1 Momentum Resolution of a Magnetic Spectrometer

In the limit of small y–component of momentum, Eq. (6.1) reduces to

$$\Delta\sin\theta = \sin\theta_2 - \sin\theta_1 = \frac{\int B\,dz}{P} \tag{6.2}$$

from which it should be apparent that $1/P$ is the quantity determined from a measurement of the difference in $\sin\theta$. Thus, the error in the quantity $1/P$ is related to the error in measurement of $\Delta\sin\theta$, which we may assume is normally distributed with standard deviation σ_{meas}:

$$\Delta\,(1/P) = \frac{\Delta P}{P^2} = \frac{\sigma_{\text{meas}}}{\int B\,dz} \tag{6.3}$$

Measurement error usually dominates at high momentum, when the bending angle is small. At low momenta, multiple scattering usually dominates. For relativistic particles, the angular uncertainty due to multiple scattering (Eq. (5.4)) is inversely proportional to P, leading to the neat relation when plugged into Eq. (6.3) :

$$\left.\frac{\Delta P}{P}\right|_{\text{ms}} = \frac{15\,MeV/c\,\sqrt{x/X_o}}{\int B\,dz} \tag{6.4}$$

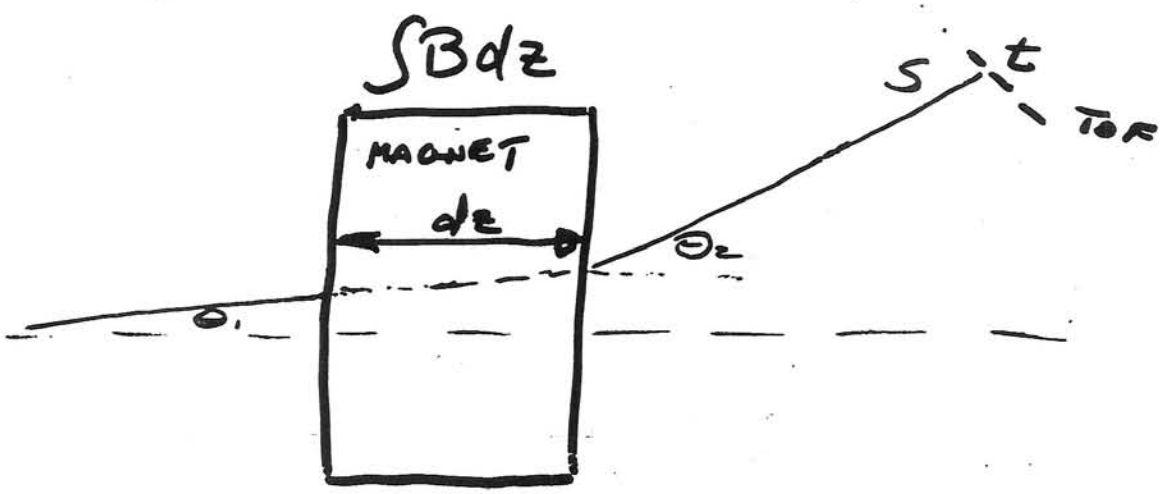

Fig. 15: The trajectory of a charged particle in a magnetic spectrometer. The magnetic field is normal to the page

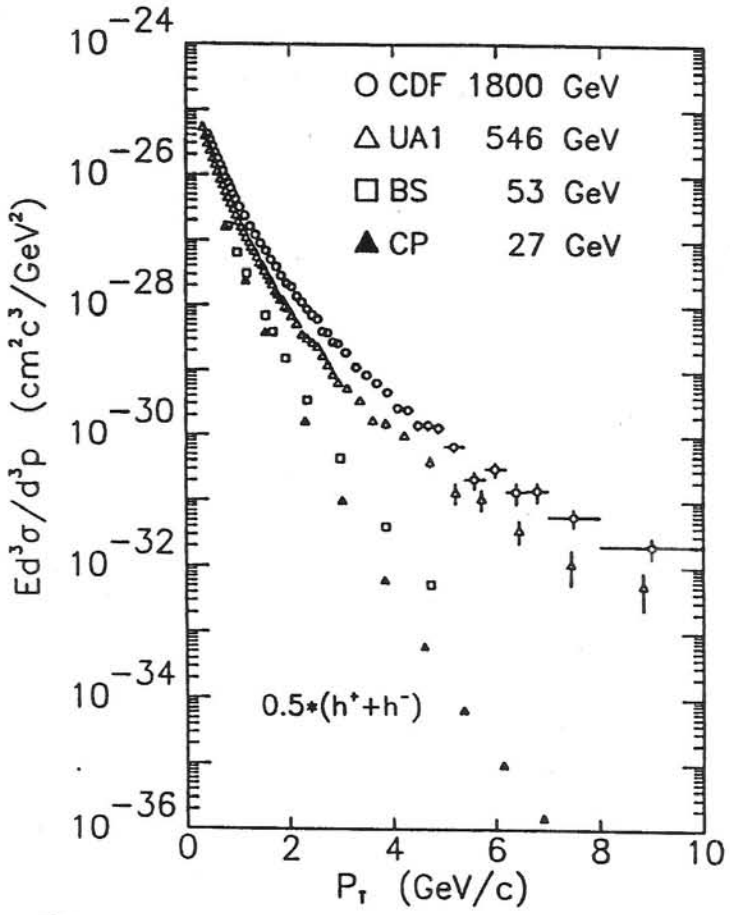

Fig. 16: The transverse momentum dependence of invariant cross sections of charged-averaged hadrons $\left(h^+ + h^-\right)/2$, near y_{cm}^{NN}, in nucleon-(anti)nucleon collisions over the available range of c.m. energies. Typical data shown are from fixed target ($\sqrt{s} = 27$ GeV), ISR (53 GeV), CERN SPS collider (546 GeV), and FERMILAB collider (1800 GeV) [32].

where the 21.2 MeV/c from Eq. (5.4) is divided by $\sqrt{2}$ to obtain the 15 MeV/c in Eq. (6.4), since only the component of multiple scattering in the bend plane affects the momentum resolution. Finally, since the uncertainties of multiple scattering and measurement error are uncorrelated so that they add in quadrature, the uncertainty in momentum measurement, the **momentum resolution**, is usually quoted in the form:

$$\frac{\Delta P}{P} = \sqrt{(a)^2 + (b\,P)^2} \tag{6.5}$$

where the first term is due to multiple scattering in the spectrometer and the second term is from measurement error.

6.2 Resolution Smearing of a Momentum Spectrum

Suppose that x_o is a quantity to be measured, e.g. momentum, which is distributed with a steeply falling distribution, exponential for example:

$$d\mathcal{P}\,(x_o) = f\,(x_o)\;dx_o = e^{-bx_o}dx_o$$

Further suppose that the true quantity x_o is measured with a Gaussian resolution function so that the result of the measurement is the quantity x, where

$$\mathcal{R}\,(x, x_o)\;dx = \text{Prob}\,(x)\,|_{x_o}\,dx = \frac{1}{\sqrt{2\pi\sigma^2}} \exp -\frac{(x-x_o)^2}{2\sigma^2}\,dx$$

The result for the measured spectrum is simply

$$f\,(x)\;dx = \int_{x_o=x-\infty}^{x_o=x+\infty} dx_o\; f\,(x_o)\;\text{Prob}\,(x)\,|_{x_o}\,dx$$

$$f\,(x) = \frac{1}{\sqrt{2\pi\sigma^2}} \int dx_o\, \exp -bx_o\;\exp -\frac{(x-x_o)^2}{2\sigma^2}$$

Complete the square:

$$f\,(x) = e^{-bx}\,e^{\frac{b^2\sigma^2}{2}} \times \frac{1}{\sqrt{2\pi\sigma^2}} \int_{x_o=x-\infty}^{x_o=x+\infty} dx_o\, \exp -\frac{\left(x-b\sigma^2-x_o\right)^2}{2\sigma^2} \tag{6.6}$$

The result, since the Gaussian is normalized over ($-\infty, +\infty$), is simply

$$f\,(x) = e^{\frac{b^2\sigma^2}{2}} \times e^{-bx} = e^{-b\left(x-b\sigma^2/2\right)} \tag{6.7}$$

There are some important implications of this deceptively simple formula. It can be interpreted in two ways: the measured spectrum is shifted higher than the true spectrum by $\Delta x = b\sigma^2/2$; or equivlalently, the measured spectrum at a true quantity x_o is higher than the true spectrum by a factor $\exp\left(b^2\sigma^2/2\right)$. Also, the steeper is the spectrum (larger b), the larger is the effect of the resolution smearing. This is a consequence of the fact that as the spectrum becomes steeper, it is relatively less probable to get larger values of the quantity of interest from the distribution itself, compared to the fluctuations due to resolution.

As in most of these discussions, real life is considerably more complicated than the simple examples. Clearly, the momentum resolution is not Gaussian, with a constant σ for all momenta, as assumed above, but depends on the true momentum x_o as in Eq. (6.5). Thus, Eq. (6.6) doesn't integrate so neatly. In general a non-exponential tail is produced at higher (measured) momenta. Also, the momenta spectra of particles are not in general exponential. However, it remains true that the steeper is the spectrum, at any value of momentum, the larger is the effect of the momentum resolution.

6.3 Shift in a Spectrum due to the effects of Binning

In addition to the effect of momentum resolution in smearing a measured spectrum from the true distribution, unintended shifts may be introduced into measured (momentum) spectra by experimenters if the effects of binning are neglected. To clarify this point, again consider a steeply falling spectrum in a quantity x_o

$$d\mathcal{P}(x_o) = f(x_o)\, dx_o\,.$$

One would like to measure the differential distribution $f(x_o)$. However the real world intrudes and what is actually measured is the integral of the distribution in small intervals (bins): e.g. for a bin of width Δ centered at the value x_o

$$F(x_o, \Delta) = \int_{x_o - \frac{\Delta}{2}}^{x_o + \frac{\Delta}{2}} f(x)\, dx$$

Typically, the differential distribution in a bin is estimated by dividing by the bin width:

$$\overline{f(x_o)} \equiv \frac{F(x_o, \Delta)}{\Delta}$$

Clearly, in the limit of zero bin width, $\Delta \to 0$, the measured distribution approaches the true distribution. For the case of wide bins, there is a reasonable procedure (not always followed) of plotting the value $\overline{f(x_o)}$ at a value of $\overline{x_o}$ shifted from the center of the bin, typically to a slightly lower value for a falling spectrum. **If this procedure is not followed, then the experimental spectrum will be higher than the true spectrum.** Especially, in the case of steeply falling spectra, not correcting for the effect of bin width can cause an apparently upward shift in the normalization.

To calculate the correct plotting point, we have to know the shape of the true spectrum, although an exponential is usually a good approximation in any individual bin. The plotting point $\overline{x_o}$ is chosen so that it lies on the true curve, or in mathematics:

$$\overline{f(x_o)} \equiv \frac{1}{\Delta} \int_{x_o - \frac{\Delta}{2}}^{x_o + \frac{\Delta}{2}} f(x)\, dx \equiv f(\overline{x_o})$$

For an exponential, $f(x) = A \exp(-bx)$, the solution is straightforward:

$$\overline{f(x_o)} = \frac{A\, f(x_o)}{b\Delta} \left[e^{\frac{b\Delta}{2}} - e^{\frac{-b\Delta}{2}} \right]$$

To get the correct solution, the exponentials must be expanded to second order in the small quantity:

$$e^z - e^{-z} = 2\left[z + z^3/3!\right] \simeq 2\,z\,e^{\frac{z^2}{3!}},$$

whereupon

$$\overline{f(x_o)} = A\,e^{-bx_0}\,e^{\frac{b^2\Delta^2}{24}} = f(\overline{x_o})$$

and the place to plot the point is slightly shifted from the center of the bin

$$\overline{x_o} = x_o - \frac{(b\Delta)^2}{24}.$$

As a general rule, beware of any experimental measurement of a falling spectrum where the points are plotted at the centers of the bins!

7. Lorentz Transformations, Kinematics, Spectra of Decay Products

In addition to measuring the spectra of primary particles, experimentalists are forced quite often to deal with the spectra of unstable particles which can only be inferred from their decay products. Two examples are

$$\pi^0 \to \gamma + \gamma \qquad \Lambda^0 \to p + \pi^-$$

Lorentz transformations and Kinematics also play a real role in the daily life of an experimentalist, since we can not always position our equipment in the desirable rest frame.

7.1 Lorentz Transformations

Consider a particle of vector momentum $\mathbf{P}$, energy E, in a particular rest frame, and invariant mass m. The **four-vector** momentum p of this particle will be denoted:

$$p = (\mathbf{P}, iE)$$

in units where the speed of light c is taken as unity. The four-dot product of two four-momentum vectors p_1 and p_2 is denoted:

$$\begin{aligned} p_1 \cdot p_2 &\equiv \mathbf{P_1} \cdot \mathbf{P_2} - E_1 E_2 \\ &= P_1 P_2 \cos\theta - E_1 E_2 \end{aligned}$$

where $\mathbf{P_1} \cdot \mathbf{P_2}$ is the dot product of the 3-momentum vectors, P_1 and P_2 are the moduli of the 3-vectors and θ is the angle between them. The squared modulus of a 4-vector is denoted

$$p^2 = p \cdot p = P^2 - E^2 = -m^2$$

and is invariant under a Lorentz Transformation.

We are often obliged to deal with particles in difference reference frames. Let a particle of invariant mass m have a four momentum

$$p^* = (\mathbf{P}^*, iE^*)$$

as measured in a coordinate system moving with a velocity β relative to the reference system in which the particle four momentum is

$$p = (\mathbf{P}, iE)$$

The **Lorentz Transformation** relates the momentum components in the reference frame to those measured in the moving coordinate system:

$$\begin{aligned} E &= \gamma\,(E^* + \beta P_L^*) \\ P_L &= \gamma\,(P_L^* + \beta E^*) \\ P_T &= P_T^* \end{aligned} \tag{7.1}$$

where $P_L = P\cos\theta$, $P_T = P\sin\theta$, $P_L^* = P^*\cos\theta^*$, $P_T^* = P^*\sin\theta^*$ are the components of momentum, longitudinal and transverse to the direction of motion, in the respective frames; θ and θ^* are the angle of the particle relative to the direction of motion in the two frames, and

$$\gamma = \frac{1}{\sqrt{1-\beta^2}} \tag{7.2}$$

Note that the transverse momentum, P_T, is conserved between the two frames, as is the **transverse mass**, $m_T = \sqrt{P_T^2 + m^2}$, while the energy and longitudinal momentum are **boosted**. The transformation of the angle relative to the direction of motion in the two frames is immediataly obtained from Eq. (7.1):

$$\tan\theta = \frac{P_T}{P_L} = \frac{\sin\theta^*}{\gamma\,(\cos\theta^* + \beta/\beta^*)} \tag{7.3}$$

where $\beta^* = P^*/E^*$ is the velocity of the particle in the moving frame.

The simplicity of the rapidity variable Eq.(2.1) becomes apparent when the Lorentz Transformation between the two frames is expressed in this variable. Let

$$y = \ln\left(\frac{E+P_L}{m_T}\right) = \frac{1}{2}\ln\left(\frac{E+P_L}{E-P_L}\right) \tag{7.4}$$

denote the rapidity of the particle in the reference frame, y^* be the rapidity of the particle measured in the moving frame and Y be the rapidity of the moving system:

$$Y = \frac{1}{2}\ln\left(\frac{1+\beta}{1-\beta}\right) \tag{7.5}$$

Then it follows from substituting Eq. (7.1) in Eq. (7.4) that

$$y = Y + y^* \tag{7.6}$$

The details are left as an exercise for the student.

7.2 Transformation to the rest system of a particle

The rest system of a particle is defined as the system in which the particle is at rest, i.e $P^* = 0$, $E^* = m$. It is then easy to see that the rest system of the particle moves with the particle velocity (as seen in the moving system):

$$\begin{aligned} E &= \gamma m \\ P &= \gamma\beta m \end{aligned}$$

7.3 Two particle collisions—the lab and c.m. systems

The description of a two particle collision is a useful exercise in relativistic kinematics. In the laboratory system, an incident particle with momentum $\mathbf{P}_1$, energy E_1 and mass m_1 collides with a particle with mass m_2, at rest. The four vectors are:

$$p_1 = (\mathbf{P}_1, iE_1) \qquad p_2 = (0, im_2)$$

In the center of mass (c.m.) system the momenta of the particles are equal and opposite, and the four-vectors are:

$$p_1^* = (\mathbf{P}_1^*, iE_1^*) \qquad p_2^* = (-\mathbf{P}_1^*, iE_2^*)$$

The transformation between the lab and c.m. systems is given in terms of the four-vector total momentum of the system $p_1 + p_2$, which is conserved in a collision. The modulus of the total four-momentum is a Lorentz Invariant quantity, which is the same in all reference systems (before and after the collision because of four-momentum conservation):

$$-s \equiv (p_1 + p_2)^2 = -(E_1^* + E_2^*)^2 \tag{7.7}$$

It is clear that $\sqrt{s}$ is the total energy in the c.m. system, which is the same as the invariant mass of the c.m. system. In terms of the lab quantities:

$$s = m_1^2 + m_2^2 + 2E_1 m_2 \tag{7.8}$$

An important point to notice is that the Lorentz transformation of the sum of four-vectors is identical to the sum of the Lorentz transformations of the four-vectors. It is then immediately apparent, using the total four-momentum vector of the collision, that the c.m. rest frame has an invariant mass $\sqrt{s}$ and moves in the laboratory system (along the direction of $\mathbf{P}_1$) with a velocity corresponding to:

$$\gamma^{\rm cm} = \frac{E_1 + m_2}{\sqrt{s}} \qquad \text{and} \qquad Y^{\rm cm} = \cosh^{-1}\gamma^{\rm cm}$$

Another useful quantity is $Y^{\rm beam}$, the rapidity of the incident particle in the laboratory system

$$Y^{\rm beam} = \cosh^{-1}\frac{E_1}{m_1}$$

Note that for equal mass projectile and target:

$$Y^{\rm cm} = Y^{\rm beam}/2$$

7.4 Two body decay of a heavy particle into light particles

This is a more advanced example of the transformation to a rest system, which has some interesting experimental applications. Consider a heavy particle which decays to two light particles. Examples would include:

$$J/\Psi \to e^+ e^- \qquad \pi^0 \to \gamma\gamma \qquad Z^0 \to \mu^+ \mu^-$$

To be specific, a particle of momentum $\mathbf{P}$, energy E, rest mass m, decays into two particles with $\mathbf{P}_1$, E_1, m_1 and $\mathbf{P}_2$, E_2, m_2. There are many questions we might wish to ask with this

starting point, however we start out with a question near and dear to the heart of somebody with a photon detector. Suppose the heavy particle was travelling in a direction normal to the surface of a PbGl wall, heading toward the detector, when it decayed a distance L from the front surface. What is the distribution in the distance d between the two decay particles when they strike the front surface of the wall? (Would any theorist think up such a question?)

The two decay particles arrive at the wall at lateral distances d_1 and d_2 from where the point of impact of the parent would have been. Since it is a 2 body decay, all three particles lie in the same plane, so that the distance d between the 2 decay particles is simply

$$d = d_1 + d_2 = L(\tan\theta_1 + \tan\theta_2) \tag{7.9}$$

where θ_1, θ_2 are the decay angles of particles 1 and 2 in the lab system and L is the distance of the decay from the detector. In the rest system of the parent, the two particles have equal and opposite momenta, so that

$$x \equiv \cos\theta_1^* = -\cos\theta_2^*$$

and $\sin\theta_1^* = \sin\theta_2^* = \sqrt{1-x^2}$. This causes a few neat cancellations when Eq. (7.3) is substituted in Eq. (7.9) for both particles. In the case of equal masses for the two decay particles ($m_1 = m_2$), the exact result for d has the simple form:

$$\frac{d}{2L} = \beta\beta^* \frac{\sqrt{1-x^2}}{\gamma\left(\beta^2 - \beta^{*2}\,x^2\right)} \tag{7.10}$$

where β^* is the velocity of the decay particles in the rest system of the parent. The case $\beta^* = 1$ is particularly interesting since it involves massless particles in the final state, e.g. photons:

$$\frac{d}{2L} = \frac{\beta\sqrt{1-x^2}}{\gamma\left(\beta^2 - x^2\right)} \tag{7.11}$$

For $|x| \geq \beta$, $d \to \infty$ or is negative (impossible for an inherently positive quantity), which means that one of the photons goes backwards in the laboratory and therefore cannot hit the detector. This is an important reminder that a massless particle can not be turned around by a Lorentz Transformation.

We now consider the distribution in d for two cases: either the total energy of the parent ($E = E_1 + E_2$) is held constant; or the energy of one of the photons (E_1) is held constant. This will be a good example in the use of conditional probability. The energies of the two photons have the same constraint on $x = \cos\theta^*$ as used above, so that the ratio of the energies is easily computed, with the result:

$$r \equiv \frac{E_2}{E_1} = \frac{1-\beta\,x}{1+\beta\,x} \qquad \text{and} \qquad x = \frac{1}{\beta}\,\frac{1-r}{1+r} \tag{7.12}$$

For E fixed, we can ignore the case when one of the photons misses the detector, and the relativistic limit ($\beta \to 1$) of Eq. (7.11) may be taken simply:

$$\frac{d}{2L} = \frac{1}{\gamma\sqrt{1-x^2}} \tag{7.13}$$

For the case E_1 fixed, the variables to use are E_1 and $r = E_2/E_1$. In this case, care must be taken about the divergences, so that terms $\sim 1-\beta^2$ can not be ignored. We solve Eq. (7.12) for $\sqrt{1-x^2}$ in terms of r, in the limit $\beta \to 1$:

$$\sqrt{1-x^2} = \frac{2\sqrt{r}}{1+r}$$

and substitute into Eq. (7.13), using the relation:

$$E = E_1 + E_2 = E_1(1+r) \qquad \gamma = \frac{E}{m} = \frac{E_1}{m}(1+r)$$

to obtain

$$\frac{d}{2L} = \frac{m}{2E_1\sqrt{r - \frac{m^2}{2E_1^2}}} \tag{7.14}$$

Note that the subtraction constant in the square root is due to a term $\sim 1-\beta^2$, and corresponds to the value of $r_\infty = \frac{m^2}{2E_1^2}$, for which d diverges when E_1 is held fixed.

To complete the kinematics at fixed E_1, we note that the minimum value of r occurs when $x = 1$ and both decay photons are collinear with the parent: one going forward in the lab on the same trajectory as the parent and hitting the detector, while the other photon goes exactly backwards on the same trajectory, heading away from the detector. In this case, from Eq. (7.12),

$$r_{\min} = \frac{1-\beta}{1+\beta} = \frac{1-\beta^2}{(1+\beta)^2} \to \frac{1}{4\gamma^2} = \frac{m^2}{4E_1^2} \tag{7.15}$$

With the kinematics out of the way, we can now concentrate on finding the distribution in d.

The case E fixed is easy since it only depends on the angular distribution of decay particles in the parent rest frame, the distribution in $x = \cos\theta^*$. For fixed E there is a minimum separation of the two photons at the wall, which occurs for the symmetric decay, $x = 0$

$$\frac{d_{\min}}{L} = \frac{2m}{E} = \frac{2}{\gamma} \tag{7.16}$$

Use $d_{\min}$ in Eq. (7.13) to eliminate γ and obtain

$$\sqrt{1-x^2} = \frac{d_{\min}}{d}$$

or

$$x = \sqrt{1 - d_{\min}^2/d^2} \tag{7.17}$$

The integral probability that two photons land on the wall separated by a distance $s \le d$ is just given by the integral probability that x lies between $\pm x(d)$, where $x(d)$ is given by Eq. (7.17). For the decay $\pi^0 \to \gamma + \gamma$, the decay is isotropic,

$$\frac{d\mathcal{P}}{dx} = \frac{1}{2}$$

so that

$$\mathcal{P}(s \le d) = \mathcal{P}(-x(d) \le x \le x(d)) = x(d) = \sqrt{1 - d_{\min}^2/d^2} \tag{7.18}$$

For the case in which one of the decay photon energies, E_1, is held constant, the relationship between the spectra of the parent and the decay particles is required. This will be discussed in the following section, after which the distribution in d will be presented.

7.5 The spectra of decay particles—the parent-daughter factor

A parent particle of momentum $\mathbf{P}$, energy E, rest mass m, decays in to two particles, as above. Furthermore, the differential probability to produce a parent particle with momentum P in range dP is given by the function:

$$d\mathcal{P}(P) = f(P)\, P\, dP$$

where for example we take $f(P)$ to be of the form

$$f(P) = A\, P^{-n}$$

so that

$$d\mathcal{P}(P) = A\, P\, P^{-n}\, dP \tag{7.19}$$

The conditional probability of finding a daughter with energy E_1, given a parent with momentum P, depends on the $x = \cos\theta^*$ distribution of the decay:

$$\frac{\partial \mathcal{P}}{\partial E_1}\Big|_P = \frac{\partial \mathcal{P}/\partial x}{\partial E_1/\partial x}$$

For equal mass decay particles,

$$E_1 = \frac{E}{2}(1 + \beta\beta^* x)$$

so that

$$\frac{\partial E_1}{\partial x} = \frac{E\beta\beta^*}{2} = \frac{P\beta^*}{2}$$

and

$$\frac{\partial \mathcal{P}}{\partial E_1}\Big|_P = \frac{2}{P\beta^*}\frac{\partial \mathcal{P}}{\partial x}$$

For a uniform decay distribution

$$\frac{\partial \mathcal{P}}{\partial x} = \frac{1}{2}$$

so that

$$\frac{\partial \mathcal{P}}{\partial E_1}\Big|_P = \frac{1}{P\,\beta^*}$$

The joint probability of finding a parent of momentum P and a daughter of energy E_1 is given by the rules of conditional probability:

$$\partial^2\mathcal{P}(P, E_1) = \partial\mathcal{P}(P)\;\partial\mathcal{P}(E_1)\,|_P = \frac{f(P)}{\beta^*}dP\, dE_1 \tag{7.20}$$

The marginal probability distribution for E_1 is found by integrating over all values of P consistent with E_1. We evaluate the case for photons in the final state, $\beta^* = 1$, and only consider the relativistic limit, ignoring the difference between P and E. A more exact treatment has been given by Sternheimer[24].

$$\partial\mathcal{P}(E_1) = \int_{E_{\min}=E_1(1+r_{\min})}^{\infty} AP^{-n}dP\, dE_1 = (1 + r_{\min})^{-n+1}\,\frac{1}{n-1}\,A\,E_1\,E_1^{-n}\,dE_1 \tag{7.21}$$

When Eq. (7.21), the daughter spectrum, is compared to Eq. (7.19), the parent spectrum, we see that they are precisely the same form (for a power law) but the daughter spectrum is

suppressed by a factor of $1/(n-1)$, for a spectrum falling with the $(n-1)$ power. This is called the **Parent-Daughter Suppression Factor.**

To continue the analysis, we now wish to find the spectrum of the second photon, E_2, for the energy of the other photon, E_1, held constant. The joint probability distribution of E_2 and E_1 is trivially related to the joint probability distribution of E and E_1, since

$$E = E_1 + E_2 \qquad \text{so that} \qquad \partial E_2|_{E_1} = \partial E|_{E_1}$$

The joint probability distribution comes directly from Eq. (7.20)

$$\partial^2 \mathcal{P}(E_1, E_2) = f(E_1 + E_2)\, dE_1\, dE_2 \tag{7.22}$$

We now use a famous rule of conditional probability to find the distribution of E_2 given E_1

$$\mathcal{P}(A, B) = \mathcal{P}(A) \times \mathcal{P}(B)\,|_A$$

Thus the conditional probability for E_2, given E_1, is just the joint probability for both E_1 and E_2 divided by the marginal probability for E_1: or Eq. (7.22) divided by Eq. (7.21).

$$\partial \mathcal{P}(E_2)\,|_{E_1} = \frac{\partial^2 \mathcal{P}(E_1, E_2)}{\partial \mathcal{P}(E_1)} = (1 + r_{\min})^{n-1}\, \frac{n-1}{(1+r)^n}\, dr \tag{7.23}$$

Note that this distribution **scales**—it is only a function of the ratio of the energies of the two photons. This equation can be integrated to find the probability of r in the range $(r_1 \le r \le r_2)$:

$$\mathcal{P}(r_1 \le r \le r_2) = \left(\frac{1 + r_{\min}}{1 + r_1}\right)^{n-1} - \left(\frac{1 + r_{\min}}{1 + r_2}\right)^{n-1} \tag{7.24}$$

This probability is obviously correctly normalized over the range $(r_{\min} \le r \le \infty)$ where $r_{\min}(E_1)$ is given by Eq. (7.15).

7.6 Distribution of d for E_1 fixed

This problem can now be completed by rewriting Eq. (7.14) to relate the distance between the two photons to the ratio of their energies, with E_1 the energy of one of the photons being fixed:

$$r - \frac{m^2}{2E_1^2} = \frac{m^2/E_1^2}{d^2/L^2} \tag{7.25}$$

The probability for d in any range is found by using Eq. (7.25) to find the corresponding values of r for the range and then using Eq. (7.24) to find the probability.

7.7 Why spend such effort on minute kinematic details?

These derivations and problems may seem a bit long-winded; but experimentalists spend most of their time dealing with such details rather than making great discoveries. Of course, if you do not spend enough effort coping with the details, you sometimes find a "discovery" which is nothing but a detail that you didn't work out correctly.

8. High Energy Physics in One Easy Lesson

One of the nice features of the search for the QGP is that it requires the integrated use of many disciplines in Physics: High Energy Particle Physics, Nuclear Physics, Relativistic Mechanics, Quantum Statistical Mechanics... An understanding of the properties of high energy $p-p$ and $p+A$ interactions is vital to the ability to distinguish the "ordinary physics" of relativistic nuclear interactions from the signatures of production of a new state of matter, the QGP. It is also possible that the "ordinary physics" may in itself be quite interesting.

8.1 Multiparticle Production in Nucleon-Nucleon ($p-p$) Collisions

When high energy nucleons collide inelastically, the predominant mode of dissipating the energy is by multiple particle production. The produced particles are distributed relatively uniformly in rapidity, with limited transverse momemtum with respect to the collision axis, leading to a description of the process as "longitudinal phase space" (recall figure 4). The modern view of strong (or nuclear) interactions is that nucleons are composed of 3 valence quarks confined into a bound state by the strong force, Quantum Chromo Dynamics (QCD), which is mediated by the exchange of color-charged vector gluons. The self-interaction of the color-charged gluons, in sharp distinction to the behavior of the uncharged quanta of electrodynamics, is believed to provide the confinement property of QCD and the related property, known as asymptotic freedom, which is the reduction of the effective coupling constant at large momentum transfers. This leads to the perverse situation that the rare "hard scattering"events of inelastic hadron collisions, involving the scattering or production of constituents with large momentum transfer, can be treated very precisely in the framework of perturbative QCD; but that the vast majority of collisions are in the non-perturbative domain and are subject instead to a more qualitative description, based primarily on empirically observed regularities.

The general framework for the study of "soft" multiparticle physics was well in place by the early 1970's [26]. One of the important conceptual breakthroughs was the realization that the distribution of multiplicity for multiple particle production would not be Poisson unless the particles were emitted independently, without any correlation [27,28]. In that era single particle "inclusive" reactions[29] were extensively studied as was the distribution in the total multiplicity per collision, a multiparticle "exclusive" quantity[30,31].

8.2 Single Particle Inclusive Reactions

A single particle inclusive reaction involves the measurement of just one particle coming out of a collision, ignoring all others. The measurements are presented in terms of the (Lorentz) Invariant single particle inclusive differential cross section:

$$\frac{Ed^3\sigma}{dp^3} = \frac{d^3\sigma}{P_T dP_T dy d\phi} = \frac{1}{2\pi}\mathbf{f}(P_T, y) \tag{8.1}$$

A uniform azimuthal distribution is usually assumed, so the integral over azimuth is simply 2π

$$\frac{d^2\sigma}{P_T dP_T dy} = \mathbf{f}(P_T, y) \tag{8.2}$$

The distributions in P_T are measured as a function of rapidity and integrated over P_T to find

$$\frac{d<n(y)>}{dy} = \frac{1}{\sigma_I}\int dP_T\, P_T\, d\phi\, Ed^3\sigma/dp^3 = \frac{1}{\sigma_I}\int dP_T\, P_T\, \mathbf{f}(P_T, y) \tag{8.3}$$

This may be further integrated over all the kinematically possible rapidity to find the mean multiplicity per interaction, $< n >$:

$$< n >= \frac{1}{\sigma_I} \int dy\, dP_T\ P_T\ \mathbf{f}(P_T, y) \tag{8.4}$$

An important point to remember about inclusive single particle cross sections is illustrated in Eq. (8.4) . Integrals of the single particle inclusive cross section are not equal to σ_I the interaction cross section, but rather equal to the mean multiplicity times the interaction cross section : $< n > \times \sigma_I$.

The inclusive charged particle P_T spectra, measured near the rapidity of the nucleon-nucleon c.m. system, y_{cm}^{NN}, (or 90° in the c.m. system in HEP jargon), is shown in figure 16. This figure[32] includes data over nearly the full available range in $\sqrt{s}$. The "high" P_T or "hard scattering" region, above 1 to 2 GeV/c, shows an enormous variation with c.m. energy, while the region below 1 GeV/c, the "soft" physics region which dominates the spectrum, remains essentially unchanged and is reasonably characterized over the full energy range by:

$$\mathbf{f}(P_T, y) = A\left(\sqrt{s}\right) \exp -6P_T\ .$$

This is the reason High Energy Physicists describe particle production as "longitudinal phase space". As the c.m. energy increased, the $< P_T >$ remains relatively constant, while the central plateau (figure 4) tends to expand to fill the available phase space in rapidity. Even at a fixed c.m. energy, the P_T and rapidity distributions are nearly independent. The $< P_T >= 2/6 = 0.333$ GeV/c at y_{cm}^{NN}, and decreases slightly, by less than 10% on the central plateau, as y moves away from y_{cm}^{NN}, then dropping to $\sim$ 220 MeV/c near the projectile rapidity[33]. The mean transverse momentum as a function of rapidity is defined:

$$< P_T > |_y = \frac{\int dP_T\ P_T\ P_T\ \mathbf{f}(P_T, y)}{\int dP_T\ P_T\ \mathbf{f}(P_T, y)} \tag{8.5}$$

The same equation applies to any rapidity region by integrating over rapidity first in both integrals. Note that in Lorentz invariant terms, this is the natural definition of $< P_T >$ so that the $|_y$ is not usually explicitly indicated.

8.3 A Warning—Beware the Seagull Effect

It has taken particle physicists many years to get comfortable with the the differential $dy = dP_L/E$ in the invariant cross section. (Relativistic Heavy Ion physicists are presently undergoing the same trauma.) Much effort was spent by particle physicists on detailed studies before it became clear that rapidity and P_T were the convenient independent variables for describing $p - p$ collisions. There is much work in the literature studying the dependence of the mean transverse momentum on P_L^* or Feynman x Eq(2.8). This creates an artificial variation of $< P_T >$ called the **Seagull Effect**[34], which in simple terms is a consequence of the fact that the transverse momentum cannot exceed the momentum.

The mean transverse momentum at fixed P_L^* is defined by using the **non-invariant** cross section as the probability distribution:

$$\begin{aligned} < P_T > |_{P_L^*} &= \frac{\int P_T\ P_T\, dP_T\ d^3\sigma/dP^3}{\int\ P_T\, dP_T\ d^3\sigma/dP^3} \\ &= \frac{\int P_T\ P_T\, dP_T\ \mathbf{f}(P_T, y)\,/E}{\int\ P_T\, dP_T\ \mathbf{f}(P_T, y)\,/E} \end{aligned} \tag{8.6}$$

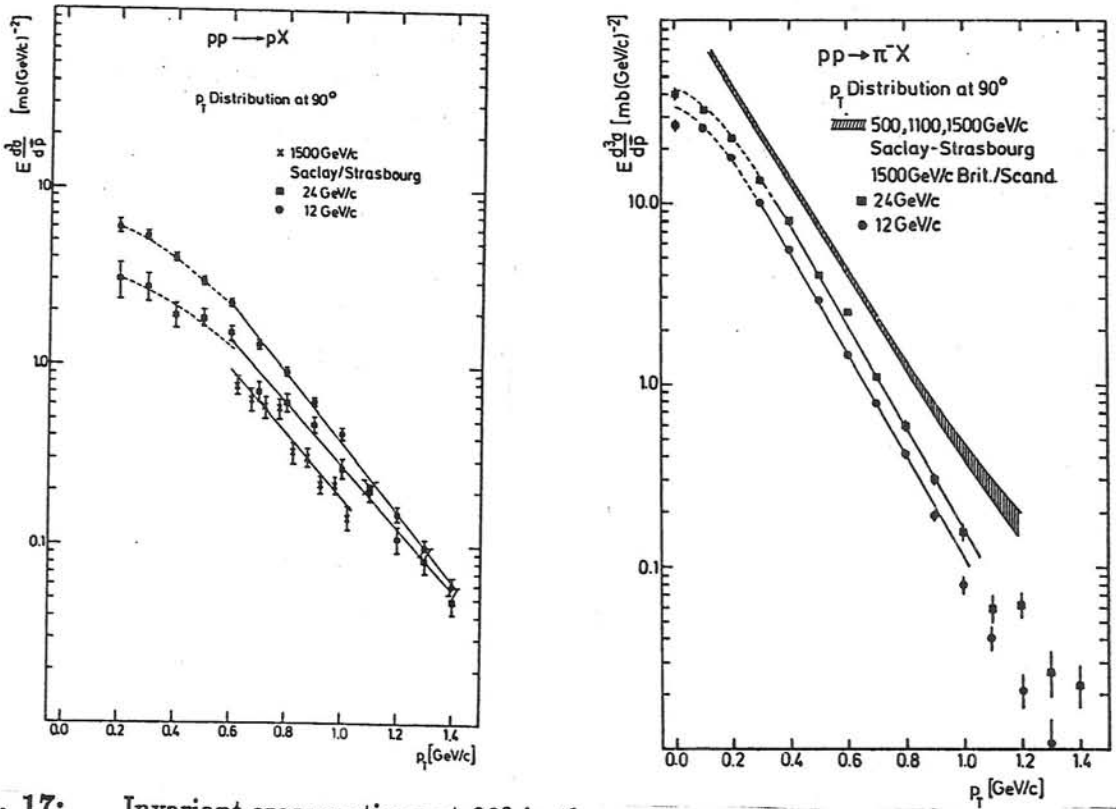

Fig. 17: Invariant cross sections at 90° in the c.m. system for proton and $\pi-$ production from $p-p$ collisions[35]. The solid lines are exponential fits in P_T, while the dashed lines are exponential in m_T.

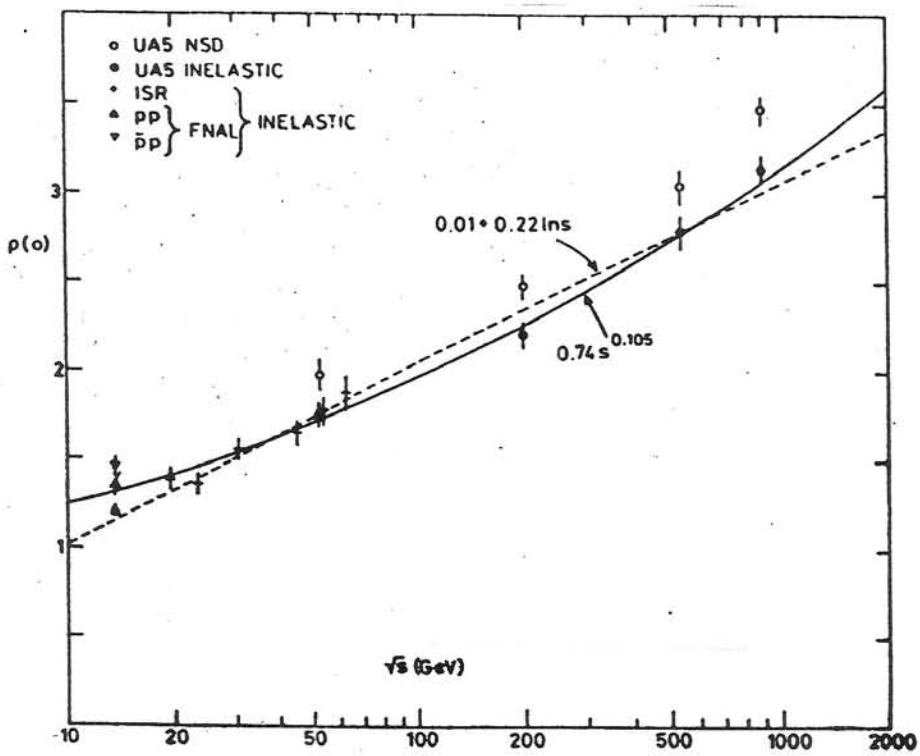

Fig. 18: Central density $\rho(0) = \frac{1}{\sigma_I}\frac{d\sigma}{d\eta}|_{\eta^*=0}$ plotted as a function of c.m. energy for data from Fermilab fixed target to Cern Collider energies. Fits to inelastic data using linear dependence in $\ln s$ or a power law dependence on s are shown[38].

This is equivalent to computing the $< P_T >$ of the distribution $\mathbf{f}/E$ where $\mathbf{f}$ is the invariant cross section. For large values of P_L^*, the energy E becomes equal to P_L^*, which for the purposes of Eq. (8.6) is a constant, so the true $< P_T >$ is obtained. For $x_F = 0$, the weighting distribution is $\mathbf{f}/m_T$ which is obviously steeper in P_T than the unweighted $\mathbf{f}$, resulting in a lower $< P_T >$. As x_F increases away from $x_F = 0$, the $< P_T >$ increases to its true value, producing a beautiful but irrelevant and confusing seagull drawing. (It may prove comforting to some to know that there was at least one thing on which Feynman's intuition was wrong!) This paragraph is placed here as a warning that the definition and plots of $< P_T >$ from the original particle physics work in the 1960's and 1970's may not mean the same thing as we understand them today.

8.4 Do particle physics spectra prefer P_T or m_T?

From the point of view of relativistic kinematics, m_T rather than P_T would seem to be the preferred variable, since under a Lorentz transformation Eq(7.1)

$$E^2 - P_L^2 = m_T^2 = P_T^2 + m^2 \tag{8.7}$$

is conserved. Although the P_T spectra of pions are generally (and conveniently) described as $\exp -6P_T$ (as above), in actual fact the data are better represented as a function of m_T. All spectra in P_T fall below an exponential for values of $P_T \sim m$, so that the spectra are better represented[35] by exponentials in m_T . (See Fig. 17). There is absolutely no change in the differential cross section for this change of variables, since $P_T\, dP_T = m_T\, dm_T$.

8.5 $\sqrt{s}$ dependence of dn/dy

The multiplicity density in rapidity, dn/dy, (Eq. (8.3)) is one of the principal descriptive variables in both high energy and Relativistic Heavy Ion physics. The mean multiplicity in $p-p$ collisions increases logarithmaically with $\sqrt{s}$. In the early 1970's, it was thought[36] that this could be explained if dn/dy on the rapidity plateau reached a constant or limiting value, so that $< n >$, the integral of the distribution (Eq. (8.4)), would just increase as $\ln s$, the available rapidity range :

$$y^*(m)\,|_{\max} = \ln \frac{\sqrt{s}}{m} \tag{8.8}$$

Although the ISR[36] produced the first real evidence for the rapidity plateau, another ISR[37] measurement was the first to show unambiguously that $dn/dy|_{y_{cm}^{NN}}$ was not a constant but rose steadily with increasing $\sqrt{s}$. The best present data[38] on the $\sqrt{s}$ dependence of the central density:

$$\rho(0) = \frac{1}{\sigma_I}\frac{d\sigma}{d\eta}\Big|_{\eta^*=0} \tag{8.9}$$

is shown in figure 18, where η is the pseudo-rapidity. When the lower energy data[35] are included, it becomes clear that the preferred fit over ther range $\sqrt{s} = 5 - 1000$ GeV is:

$$\rho(0) = 0.74\,\left(\sqrt{s\,(GeV)}\right)^{0.210}$$

There is a clear, but very slow increase of $\rho(0)$ with $\sqrt{s}$. Note that the increase in central multiplicity density in going from $\sqrt{s_{NN}} = 5.39$ GeV, which is the nucleon-nucleon c.m. energy for the BNL heavy ion program, to $\sqrt{s_{NN}}$= 19.4 GeV at CERN, is only a factor of 1.31.

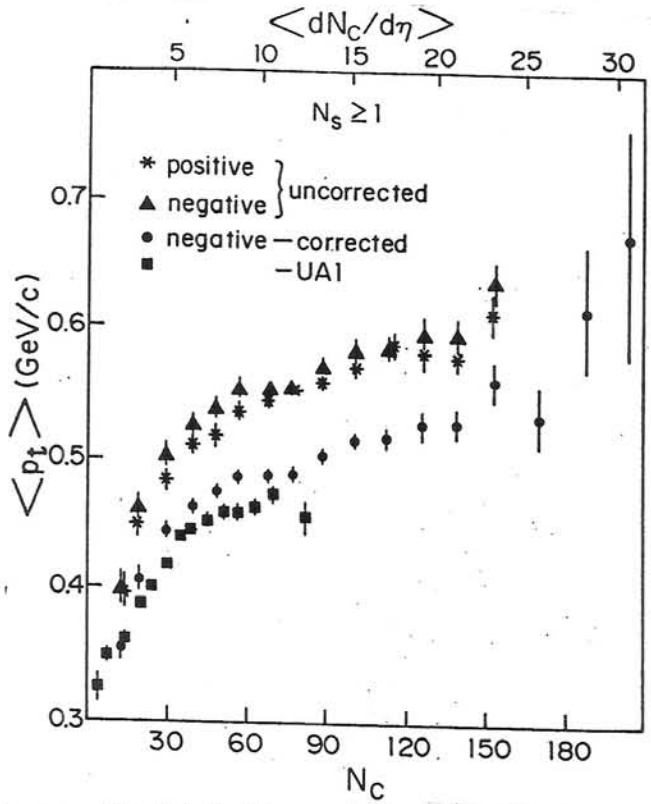

Fig. 19: $< P_T >$ vs. $dN_C/d\eta$ in the central region of $p - \bar{p}$ collisions at $\sqrt{s}$=1.8 TeV[39]. The UA1 data[40] are also shown.

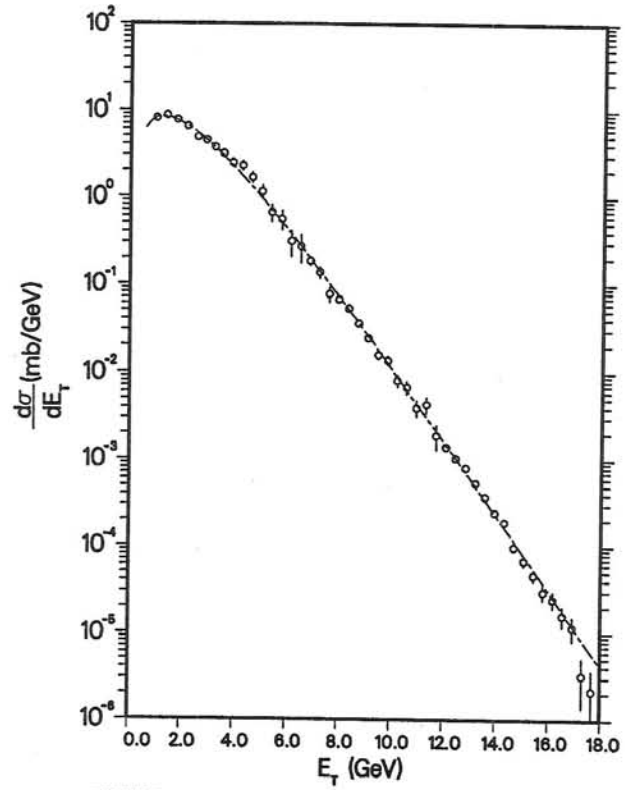

Fig. 20: The NA5 full azimuth E_T spectrum from $p - p$ collisions at 300 GeV incident energy [46] together with the fit to a gamma distribution with $p = 2.39 \pm 0.06$, $< E_T >= 2.2$ GeV, $\sigma_{pp}^{\text{det}} = 24 \pm 1$ mb, $\chi^2 = 62.4/43$ d.o.f.

8.6 Has the QGP already been found in $p-\bar{p}$ collisions ?

An experiment at the FERMILAB $p-\bar{p}$ collider, with the highest available $\sqrt{s} = 1.8$ TeV, has searched for production of the QGP by looking at the dependence on $< P_T >$ as a function of dn/dy on the central plateau[39]. The data show a striking increase of $< P_T >$ with dn/dy (see Fig. 19). This effect was also seen by UA1 at the CERN collider[40] and is expected in hydrodynamical modes[41], but is largely absent[42] at c.m. energies below 63 GeV. The key question from figure 19 is whether the rise in $< P_T >$ for $dN_c/d\eta \geq 25$ is evidence for the "Van Hove" signature of QGP production[11], or is merely a statistical fluctuation. This is left as an exercise for the student.

8.7 Multiparticle inclusive reactions—E_T distributions

In the 1980's, multiparticle inclusive measurements, in which many but not all of the particles from an interaction are measured, became a leading tool in the description of the "soft" reactions which dominate the particle production process in high energy hadron collisions. The two principal multiparticle inclusive variables are the charged particle multiplicity and the transverse energy flow, taken in restricted intervals of rapidity rather than integrated over all phase space, These variables are very closely related, but it some time for this fact to be understood[43]. The multiplicity is one of the classical observables in the study of high energy collisions [44,45], while the original measurements of transverse energy distributions[46] were stimulated by the desire to detect and study the jets from "hard" scattering, with an unbiased trigger. Contrary to early expectations, the transverse energy is dominated by "soft collisions". The transverse energy is made up of a structureless cloud of low transverse momentum (~ 0.40 GeV/c) particles[47]. Jets are swamped[48].

The strong relationship of the multiplicity and transverse energy distributions is a consequence of the fact that the transverse momentum distribution for particle production is largely independent of the rapidity and multiplicity distributions [33]. Thus, an E_T measurement is simply an analog method of counting particles: each particle produced has roughly the same value of $E_i \sin\theta_i \simeq < p_T >$ [49].

The formal definition of the **transverse energy**, $\mathbf{E_T}$, is

$$E_T = \sum_i E_i \sin\theta_i \qquad \text{and} \qquad dE_T(\eta)/d\eta = \sin\theta(\eta)\; dE(\eta)/d\eta \tag{8.10}$$

where the sum is considered to be taken over all particles emitted on an event into a fixed but large solid angle. Following the original work of NA5 [46], the traditional solid angle was typically taken as the full azimuth, $\Delta\phi = 2\pi$, and c.m. pseudo-rapidity interval $\Delta\eta^* \simeq \pm 0.8$. It is important to note that E_T does not have a well defined property under Lorentz transformations. Relativistically preferable quantities have been discussed from time to time [50], but these are rarely used because the above definition of E_T is the most convenient for measurements in segmented calorimeters. In this case, the sum is over the energy E_i measured in the ith calorimeter cell, with average polar angle θ_i.

Three distinct varieties of "E_T" measurements have been reported in the literature. Each technique has its own systematic problems and biases, and the relationship of the quantity "E_T" measured in calorimeters to an idealized quantity (what a theorist would imagine) is not at all straightforward[51–52]. The first and "classical" method [46,48] uses a full azimuth hadron calorimeter, typically 5 to 8 hadron absorption lengths thick, which thus measures all hadrons regardless

of whether they are charged or neutral. The second method uses a track chamber device to reconstruct the momenta of all charged particles and then to construct E_T^c, the transverse energy of charged particles, usually with the assumption that all the particles are pions [53,54]. The third method [55,56] uses an electromagnetic shower counter, typically 15 to 20 radiation lengths thick, to detect the energy of the photons from the decays of neutral mesons ($\pi^0 \to \gamma\gamma$ and $\eta^0 \to \gamma\gamma$) and has thus been called [55]"neutral transverse energy", E_T^0, or "electromagnetic" transverse energy [56], E_T^{em}. The shower counter can be a dedicated detector [55] or the electromagnetic section of a hadron calorimeter [56].

The now "classical" NA5 measurement[46] for 300 GeV $p-p$ collisions is shown in figure 20. This is the first measured E_T distribution in the present day usage of the terminology. The detector was essentially the same hadron calorimeter (ring calorimeter) as used in the NA35 experiment (figure 9), covering the full azimuth and c.m. polar angular interval $54° < \theta^* < 135°$ at 300 GeV incident energy.

9. Relativistic collisions involving nuclei

The study of relativistic collisions involving nuclei has a long tradition in high energy physics, dating from studies in the 1930's of cosmic ray interactions in photographic emulsions and in metal plates inside cloud chambers[44,45]. The subject revived in the early 1970's, when it was again realized that multiple particle production in nuclei is sensitive to the space-time structure of the fundamental nucleon-nucleon particle production process. Also, the concept of the nucleon as a composite system of quarks and gluons was being developed at this time, so there was a desire to study the interactions of a real composite system (the nucleus) whose properties were well known [57,58]. Measurements of the interactions of $\sim$ 100 GeV protons in nuclei were made at FERMILAB, and later at the CERN SPS, and produced results which proved to be much cleaner, and simpler to interpret, than expected.

9.1 Proton-Nucleus interactions at ~100 GeV

When a high energy proton passes through a nucleus, it can make several successive collisions. However, the charged particle multiplicity density, dn/dy, observed in proton+nucleus ($p+A$) interactions is not simply proportional to the number of collisions, but increases much more slowly. The main features of $p+A$ interactions are strikingly illustrated in figure 21, which is the pseudorapidity distribution of relativistic charged particles ($v/c > 0.85$) from 200 GeV proton interactions in targets of various nuclear size [59]. The nuclear size is discussed in terms of $\bar{\nu}$, the average number of collisions, or more properly, absorption mean free paths encountered by an incident particle passing through a nucleus of atomic mass A:

$$\bar{\nu} = \frac{A\sigma_{hp}}{\sigma_{hA}}, \tag{9.1}$$

where σ_{hp} and σ_{hA} are the absorption cross sections for the incident hadron on a nucleon and a nucleus, respectively [57,60]. The targets used covered the range from CH_2 to carbon to uranium, but unfortunately are not indicated on the figure. The most dramatic feature of figure 21 is that there is virtually no change in the forward fragmentation region ($\eta > 5.0$) with increasing A. By contrast, there is tremendous activity in the target region ($\eta \leq 0.5$). In the central

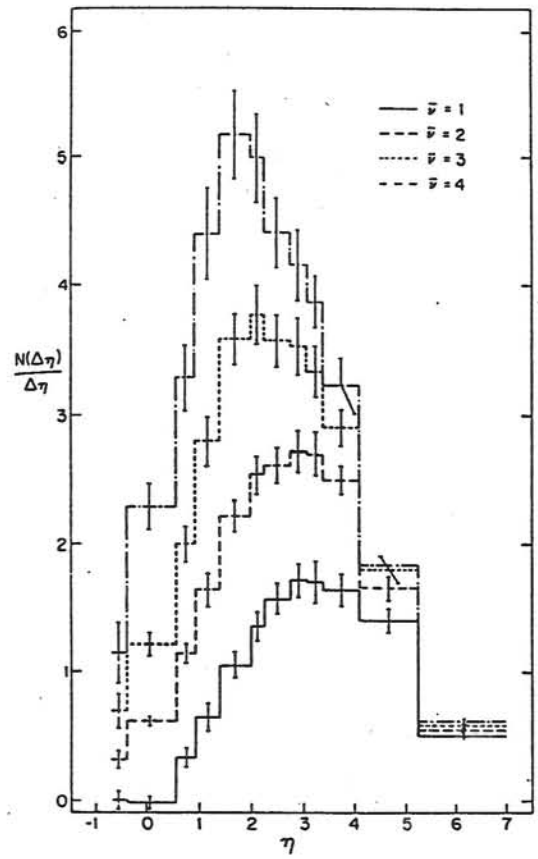

Fig. 21: Pseudorapidity distributions $dn/d\eta$ of relativistic charged particles for various values of $\bar{\nu}$ in 200 GeV/c proton-nucleus interactions [59].

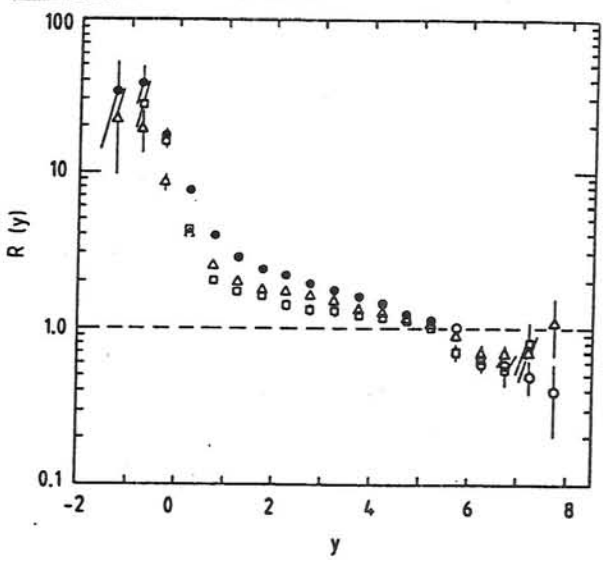

Fig. 23: The charged particle multiplication ratio, $R(y) = (d\sigma/dy)_{pA} / (d\sigma/dy)_{pp}$ for pXe (circles), pAr (triangles), and pNe (squares) interactions versus the rapidity y [61]. [Note: the caption has been copied from reference[61], however it seems that $R(y)$ is really the ratio of dn/dy and not $d\sigma/dy$.]

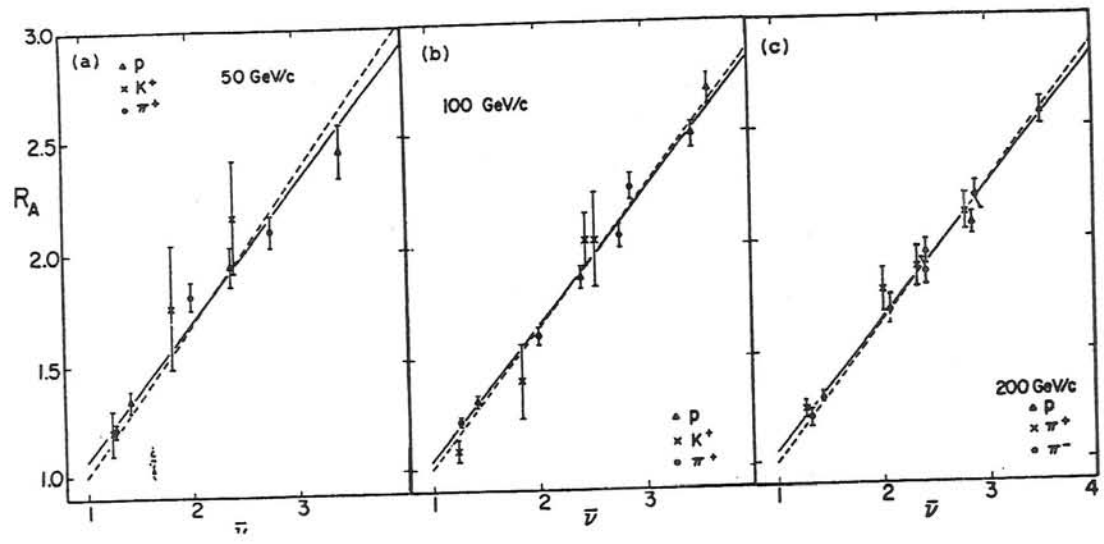

Fig. 22: Scaled average multiplicity R_A as a function of nuclear thickness. The data are for incident p, π^+, π^-, with momenta (a) 50 GeV/c, (b) 100 GeV/c, (c) 200 GeV/c. The solid lines are the result of the fit $R_A = a + b\bar{\nu}$, the dashed lines $R_A = 1 - b + b\bar{\nu}$, for each data set. All the data can be fit to a single linear relation, given in the text [59].

region, $dn/d\eta$ increases with A and the peak of the distribution shifts backwards. The integral of the distribution (the average multiplicity) shows a linear increase with $\bar{\nu}$ independently of the identity of the incident hadron or the nuclear target (figure 22). All the data could be fit by the linear relation [60,59,57]

$< n >_{hA} / < n >_{hp} = (0.45 \pm 0.02) + (0.59 \pm 0.01)\,\bar{\nu}$, or approximately

$$R_A = \frac{< n >_{hA}}{< n >_{hp}} = \frac{1 + \bar{\nu}}{2}. \tag{9.2}$$

The same features are evident in data taken in a streamer chamber at CERN [61] for 200 GeV/c proton interactions on protons, Ne, $Ar\,(\bar{\nu} = 2.3)$ and $Xe\,(\bar{\nu} = 3.3)$. The rapidity distribution dn/dy for all charged particles (including non-relativistic target nucleons) is presented as $R(y)$, the ratio to $p - p$ interactions (figure 23). The division of the rapidity distribution into three distinct domains is clear from this plot: the projectile fragmentation region ($y > 5.0$), the target region ($y < 1.0$), and the central region ($1.0 < y < 5.0$). The dramatic change in slope of $R(y)$ in the target region is a reflection of the kinematic difficulty of producing particles in this region from a $p - p$ collision, as well as an indication of considerable emission of slow protons from the nuclear targets. The total number of "produced particles" [62] as well as $dn/dy|_{y_{cm}^{NN}}$ for all charged particles, where $y_{cm}^{NN} = 3.0$ is the rapidity of the nucleon-nucleon $(N - N)$ c.m. system, both obey the linear relation given above. Also, although the distributions are asymmetric about y_{cm}^{NN}, the asymmetry cancels out when taking integrals of the multiplicity in symmetric intervals of up to $\Delta y = \pm 2$ units about y_{cm}^{NN}, so that the average multiplicities in these symmetric rapidity intervals about y_{cm}^{NN} show precisely the same linear relation(to 1% or 2%) as the "central density" $dn/dy|_{y_{cm}^{NN}}$.

9.2 Models for multiparticle production in Nuclei

The striking features of the ~ 100 GeV hadron-nucleus data could be elegantly explained by models which took into account the time and distance scales of the soft multiparticle production process [58]. A nucleus is considered to be rather transparent, so that a relativistic incident hadron can pass right through, and can make many successive collisions. Once a relativistic hadron interacts inside a nucleus, it becomes an excited hadron, and remains in that state inside the nucleus because the uncertainty principle and time dilation prevent it from fragmenting into particles until it is well outside the nucleus. This feature immediately eliminates the possibility of a cascade in the nucleus from the reinteraction of the secondary fragments. A further assumption is that the excited hadron interacts with the same cross section as an unexcited hadron and that the successive collisions do not affect the excited state or its eventual fragmentation products. This leads to the conclusion that the elementary process for particle production in nuclear collisions is the excited nucleon, and to the prediction that the multiplicity in nuclear interactions should be proportional to the total number of projectile and target participants, rather than to the total number of collisions.

The simplest expression of these ideas and assumptions is the Wounded Nucleon Model (WNM) [63], which describes a large body of data from high energy interactions with nuclei. In this model, the number of nucleons struck in a nuclear interaction is computed from the static (Glauber) nuclear geometry [64]; but a nucleon contributes only once to the production of

particles no matter how many times (≥ 1) it is successively struck. The WNM was originally introduced to explain the behavior of the average multiplicity in nuclear interactions; and was later extended to explain multiplicity distributions [65] and E_T^c distributions [66] in limited intervals of rapidity. The behavior of the average multiplicity is neatly explained in this model: a nucleon-nucleon collision has two wounded nucleons, a nucleon-nucleus interaction has an average of $\bar{\nu}$ collisions, which corresponds to $(1+\bar{\nu})$ wounded nucleons (the incident nucleon plus the $\bar{\nu}$ target nucleons), giving a ratio of the mean multiplicity in $p+A$ to $p-p$ interactions as $R_A = (1+\bar{\nu})/2$. Recently, two of the leading models of soft collisions and fragmentation have been extended to nuclear collisions [67,68]; but the Wounded Nucleon Model, and its close relative, the Addidive Quark (really wounded projectile quark) Model (AQM) [69] retain their popularity because the geometry of the nuclear interaction can be separated from the dynamics of particle production, which can be taken directly from measured distributions [65,66,70,71].

9.3 "Hard" Collisions—Beware the "Cronin Effect"

Further constraints on the models of particle production in nuclei are provided by hard collisions such as lepton-pair production [72] (colloquially known as Drell-Yan [73]) and inclusive single particle production at large P_T [74]. In the constituent picture of hard scattering, the proton is already treated as a composite object, so the extension of this picture to the interactions of nuclei was thought to be straightforward. The transverse distance scale of the collision ($\simeq 1/P_T$) is so small that the constituents should act independently, thus giving a cross section proportional to the total number of constituents in the projectile and target, or proportional to $A_1 \times A_2$ for the interaction of two nuclei [75]. It was therefore somewhat surprising when measurements at FERMILAB in the period 1973-1977 indicated an "anomalous" nuclear enhancement (also known in HEP jargon as the "Cronin Effect"). The ratio of the inclusive cross sections at a given P_T in $p+A$ to $p-p$ interactions could be represented by a power law $A^{\alpha(P_T)}$. The exponent $\alpha(P_T)$ was greater than 1.0 at large P_T and varied with the $\sqrt{s}$, P_T, and the type of particle produced, leading to the description as "anomalous". After much work, over a period spanning 13 years [76], the deviation of the behavior from $A^{1.0}$ was reasonably well understood theoretically as being caused by smearing of the steeply falling hard-scattering P_T spectrum due to multiple scattering of the constituents in the nucleus [77,78].

Suffice it to say that there are no fully relativistic space-time models at this time that explain all facets of the data, and both the hard and soft collisions, although the subject is steadily advancing [79].

9.4 Reaction dynamics studies using E_T distributions.

The development of E_T distributions as a diagnostic tool to study the reaction dynamics of multiparticle production in relativistic nuclear collisions was started at CERN in 1980, when light ions were injected into the ISR. $\alpha-\alpha$ and $p-\alpha$ interactions were studied at nucleon-nucleon c.m. energies ($\sqrt{s_{NN}}$) of 31 GeV for $\alpha-\alpha$ and $\sqrt{s_{NN}} = 44$ GeV for $p-\alpha$. A subsequent run took place in 1983, with $\alpha-\alpha$, $p-\alpha$, $d-d$ and $p-p$ interactions all studied at $\sqrt{s_{NN}} = 31$ GeV. The AFS collaboration led the way in analyzing the charged multiplicity [65] and E_T^c distributions [54] in terms of the Wounded Nucleon Model (WNM) [66]. Excellent fits were obtained to the $\alpha-\alpha$ and $p-\alpha$ E_T^c distributions, in the symmetric rapidity range $|y| < 0.8$ in the nucleon-nucleon

c.m. system, using $p-p$ data in the same interval to determine the spectrum of a "wounded nucleon", (see figure 24). The fit covers more than three orders of magnitude in cross section and extends to E_T^c values of 3 or 4 times the $< E_T^c >$.

The high luminosities of the second ISR light ion run allowed the BCMOR collaboration to extend measurements of E_T^0 distributions to over 10 orders of magnitude in cross section and to values of E_T^0 more than 10 times the average [70]. The spectrum of total neutral energy emitted in the central region was measured using an electromagnetic shower counter which detected, but did not separately resolve, the photons from the decays of neutral mesons ($\pi^0 \rightarrow \gamma\gamma$ and $\eta^0 \rightarrow \gamma\gamma$). A vertex with at least two charged tracks was reqired, and the spectra were corrected for the energy deposited by charged particles. The c.m. acceptance in which the neutral energy was detected covered 90% of 2π in azimuth with an average c.m. pseudorapidity acceptance inside this region of $|\eta| \leq 0.9$. Distributions in both the "transverse neutral energy" E_T^0 and the "total neutral energy" $E_{\rm TOT}^0$ observed in the detector were obtained for $p-p$, $d-d$ and $\alpha-\alpha$ interactions all at the same $\sqrt{s_{NN}} = 31$ GeV (see figure 25). Note that the shapes of the spectra are essentially identical in both $E_{\rm TOT}^0$ and E_T^0. This illustrates that, in a limited rapidity interval, the "energy flow" or the "transverse energy flow" are equivalently useful, since they are simply related by $< \sin\theta >$ in the interval ($\simeq 0.87$ for the data of figure 25), so long as the rapidity distribution of the transverse energy does not change over the spectrum.

One noteworthy feature of the spectra in figure 25 is that the $\alpha-\alpha$ data extend beyond the $p-p$ kinematic limit. This clearly indicates a multiple collision process. In the first published measurements of E_T distributions in nuclei, from $p+A$ interactions at FERMILAB [80], the A dependence of the spectra at a given E_T was parameterized as a power law, $A^{\alpha(E_T)}$, like the single particle inclusive spectra. It is evident that this parameterization makes no sense for the data in figure 25, since the ratio to $p-p$ collisions is undefined beyond the kinematic limit. The formalism of hard scattering is, once again, inappropriate for the soft multiparticle physics of E_T distributions; and analysis in terms of the WNM or AQM was thought to be more reasonable. The spectrum of a wounded nucleon (or quark) was determined from the measured $p-p$ distribution (figure 25), while the relative probability distribution of wounded nucleons or wounded projectile quarks was computed from the nuclear geometry of the α–particle [71]. Although the WNM successfully accounts for the increase of the observed integrated cross section and $< E_{\rm TOT}^0 >$ from the $p-p$ to the $\alpha-\alpha$ data, it leads to the wrong functional form for the high-energy tail of the $\alpha-\alpha$ distribution over a range of more than 6 orders of magnitude in cross section [70] (dot dash line). The Additive Quark Model [71] (solid line) seems to provide a much better description of the $\alpha-\alpha$ data, as does the DPM [67]; and it is tempting to speculate whether this implies that the quark substructure of nucleons can be inferred from these studies of soft collision effects in nuclei[81].

9.5 Empirical Observations may be more useful than Models

A surprising result was obtained during the analysis of this data when it was realized [70] that a simple gamma distribution represented both the $p-p$ and the $\alpha-\alpha$ spectra as well as, if not better than, the models of multiple nucleon-nucleon collisions (figure 26a). In addition,

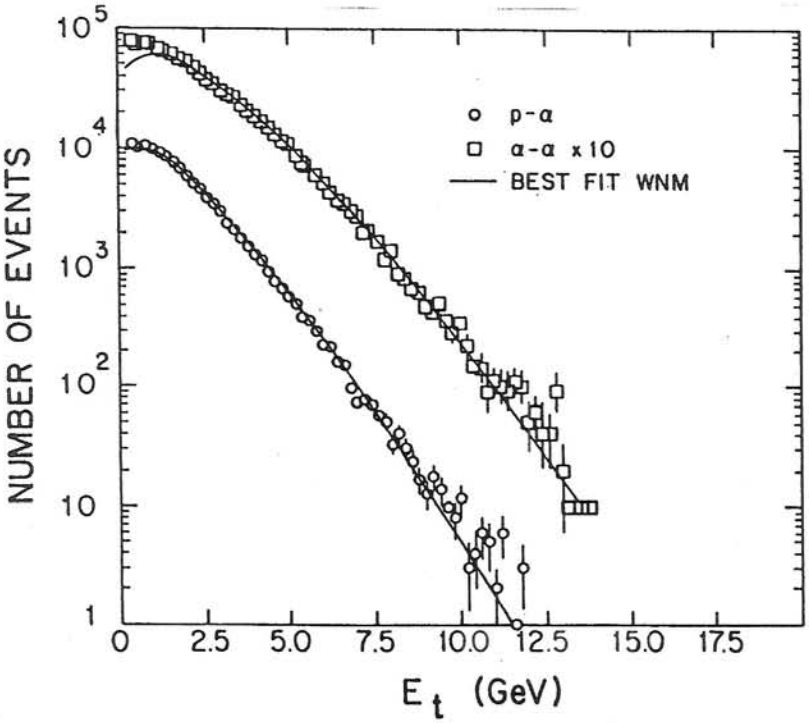

Fig. 24: Comparison of the $p-\alpha$ and $\alpha-\alpha$ charged particle yields, presented as E_T^c, obtained by the AFS collaboration, together with the WNM fits [66].

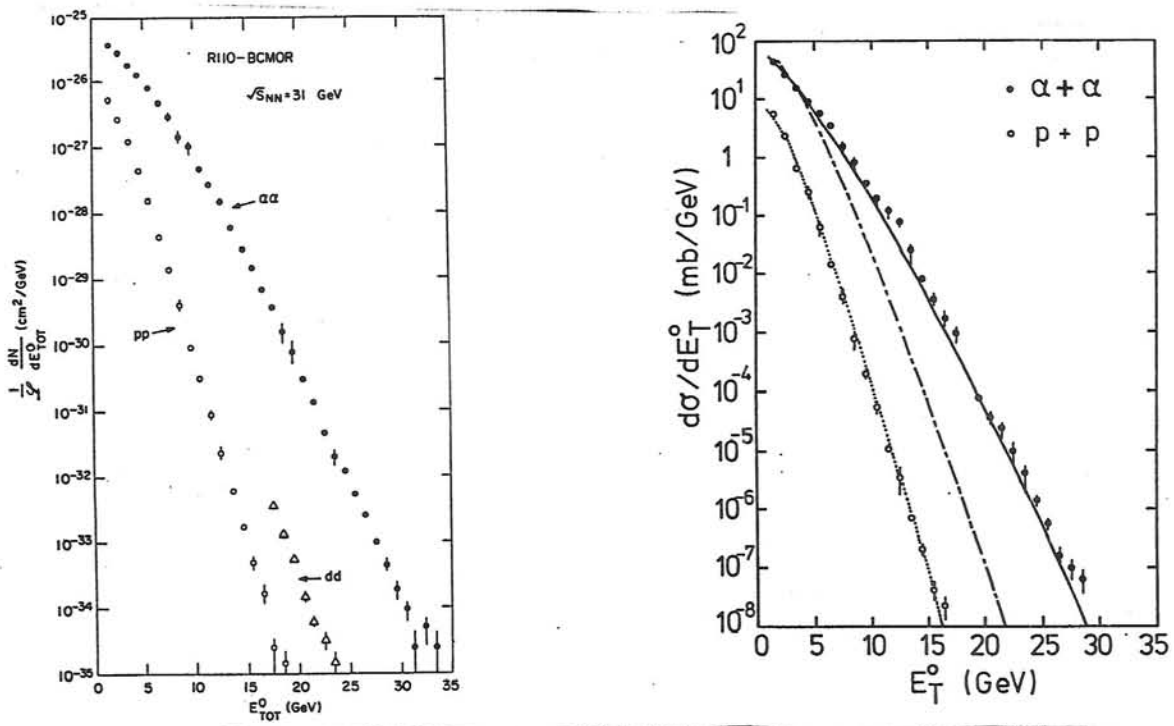

Fig. 25: The neutral energy spectra[70] for $p-p$, $d-d$, and $\alpha-\alpha$ interactions at $\sqrt{s_{NN}} = 31$ GeV. (a) Total neutral energy, $E^0_{\rm TOT}$. (b) Transverse neutral energy, E^0_T for $\alpha-\alpha$ and $p-p$ interactions together with the Wounded Nucleon Model fit (dot-dash line) and the Additive Quark Model fit (solid line). The dotted line is a fit of the $p-p$ data to a gamma distribution, with $p = 2.50$ and $<E^0_T>= 1.57$ GeV [71]. Only the statistical errors are shown on the figures. The systematic errors for the $E^0_{\rm TOT}$ spectra are small. For technical reasons the systematic errors for the measurement of E^0_T are larger [70].

the values of the parameter p of the gamma distribution:

$$< E > f(E) = \psi(z) = \frac{p}{\Gamma(p)} (pz)^{p-1} e^{-pz} \qquad \text{where} \qquad z = \frac{E}{< E >} \tag{9.3}$$

were practically identical for both spectra, namely $p = 2.50 \pm 0.06$ for $p-p$ and $p = 2.48 \pm 0.05$ for $\alpha - \alpha$, which meant that the $E^0_{\rm TOT}$ spectra for $p-p$ and $\alpha - \alpha$ interactions at the same nucleon-nucleon c.m. energy obey a sort of KNO scaling [82]. A much more graphic illustration of the KNO scaling is obtained by making a KNO-plot of both the $p-p$ and $\alpha-\alpha$ data (figure 26b). The $E^0_{\rm TOT}$ spectra plotted in this way are nearly indistinguishable over 10 orders of magnitude! In particular the tails of the $p-p$ and $\alpha-\alpha$ distributions are the same, when measured in units of the average value of the energy $< E^0_{\rm TOT} >$, in each case. This appears to indicate some unexpected coherence in the multiple collisions involved in the $\alpha - \alpha$ scattering, and is quite opposite from the behavior predicted in the extreme-independent-collision hypothesis of the WNM and the AQM, where the energy emitted on the independent collisions would be combined at random. Since the AQM also appears to fit the data, it is possible that the effect is simply an accident of the geometry of the multi-quark collisions. In order to address this question, 3 or 4 additional(!) orders of magnitude of cross section sensitivity would be required, so that the geometrical effect of the quarks would be exhausted and the dynamics would take over [83,84].

10. Details of the multiple-collision analysis.

The analyses of E_T distributions in light nuclei at the CERN ISR, by the AFS and BCMOR collaborations, proved to be complementary to the systematic studies of multiplicity in limited intervals of rapidity by the UA5 collaboration [85], and led to a whole new empirical formalism to for the description of soft multiparticle physics in proton-(anti)-proton collisions as well as in nuclei.

The multiparticle measures, E_T and multiplicity, are additive in the case of multiple collisions, either in the good sense, when they can be used to analyze the effects of multiple collisions in nuclei, or in the bad sense, when they are sensitive to the random pile-up of multiple events in time. In the extreme-independent-collision models of nuclear scattering, the effects of the nuclear geometry of the interaction can be calculated independently of the dynamics of particle production, which can be taken directly from experimental measurements. The calculation of the distribution in the number of basic elements of particle production — be they wounded nucleons, or wounded projectile and/or target nucleons or wounded projectile quarks, or number of $N-N$ collisions — is performed in the static (Glauber) approximation [64] by averaging over the impact parameter of the nucleus-nucleus scattering, usually by a simple Monte Carlo method [65,66,70,71]. Woods-Saxon densities [86]:

$$\rho(r) = \frac{1.0}{1.0 + e^{(r-c)/a_0}}, \tag{10.1}$$

and in some cases the actually measured form-factors, are used for the spatial distributions of nucleons in the projectile and target nuclei. Sometimes, a hard core, or the minimum allowable distance between the centers of two nucleons in a nucleus, is also imposed. The only free parameter is these "geometrical" calculations is the effective $N-N$ inelastic cross section,

σ_{NN} (or quark-nucleon cross section σ_{qN}), used to compute the absorption mean free path of a nucleon (or quark) in the nucleus. A collision is defined when the center of a nucleon (or quark) in the projectile intercepts the center of a nucleon in the target nucleus at a distance $r \leq \sqrt{\sigma/\pi}$.

The separation of the "geometry" from the dynamics allows experimental measurements to be used to derive the fundamental E_T spectrum of the elementary collision process, which is then used as the basis of the analysis of a nuclear scattering as the result of multiple indpendent collisions. Let $f_1(E)$ represent the differential probability for the emission of energy E in dE into the detector for the elementary collision process. Then $f_n(E_0)\,dE_0$, the probability of observing E_0 in dE_0 for n such collisions, independently overlapped, is given by the n-fold convolution of $f_1(E)$. This is easy to understand by writing $f_n(E_0)$ in the recursive form

$$f_n(E_0) = \int_0^{E_0} dE\ f_1(E)\ f_{n-1}(E_0 - E) \tag{10.2}$$

where $0 \leq E_0 \leq n\sqrt{s_{NN}}$. Here, E_0 represents the energy emitted on n collisions. The first term inside the integral is the probability of emitting energy E on one collision, and the second term is the probability of emitting a total of $E_0 - E$ on $n-1$ collisions.

It is important to realize that all the n-collision spectra are normalized to unity; only the shapes are determined. The spectra can be weighted according to the probability or cross section for n simultaneous collisions, as given by the "geometrical" calculation. Alternatively, the data can be used to fit for the n-collision cross sections σ_n, $n = 1, 2, \cdots, m$ as parameters:

$$\frac{d\sigma}{dE} = \sum_{n=1}^{m} \sigma_n\, f_n(E) = \sigma^{\text{det}} \sum_{n=1}^{m} r_n\, f_n(E) \tag{10.3}$$

where r_n is the relative probability for n collisions and σ^{det} is the integral of the observed spectrum.

The analysis is greatly facilitated by using a gamma distribution to represent the energy spectrum of the elementary process:

$$f_1(E) = \frac{b}{\Gamma(p)}\,(bE)^{p-1}\,e^{-bE}. \tag{10.4}$$

It should be noted that $p > 0$, $b > 0$, $f_1(E)$ is normalized to unity over the range $0 \leq E \leq \infty$ and that $\Gamma(p)$ is the gamma function of p, $= (p-1)!$ if p is an integer. The moments of the distribution are given in terms of the two parameters p and b:

$$\mu = p/b \quad \sigma = \sqrt{p}/b \quad \gamma_1 = 2/\sqrt{p} \quad \gamma_2 = 6/p \tag{10.5}$$

where the moments are the mean (μ), the standard deviation about the mean (σ) and the first two cumulants (γ_1, γ_2). The gamma distribution is used because of its elegant convolution property. The n-fold convolution of the gamma distribution $f_1(E)$ is simply given by the function

$$f_n(E) = \frac{b}{\Gamma(np)}\,(bE)^{np-1}\,e^{-bE}, \tag{10.6}$$

i.e. $p \to np$ and b remains unchanged. Furthermore, the convolution of a gamma distribution (parameters p, b) with another gamma distribution (parameters q, b) is simply a gamma distribution with parameters $p + q$, b. The convolution property of the gamma distribution allows

the elementary spectrum to be "deconvoluted" from a measured spectrum, e.g. from $p-p$ collisions, and then re-convoluted to obtain the spectrum of the nuclear scattering.

This analysis is particularly straightforward in the case of E_T spectra of symmetric nuclei measured in a symmetric rapidity interval about y_{cm}^{NN}. The observed $p-p$ spectrum is treated as the probability function for the collision of two nucleons:

$$f_1(E) = \frac{1}{\sigma_{pp}^{\rm det}} \frac{d\sigma_{pp}}{dE}, \tag{10.7}$$

where $\sigma_{pp}^{\rm det}$ is the integral of the observed spectrum

$$\sigma_{pp}^{\rm det} = \int_0^{\sqrt{s}} dE \;\; d\sigma_{pp}/dE. \tag{10.8}$$

The spectrum is then fit to a gamma distribution for the parameters b and p. For instance, for the data of figure 25a, the fit to the $p-p$ E_{TOT}^0 spectrum is excellent (see figure 26a), with parameters $b = 1.41 \pm 0.01\,{\rm GeV}^{-1}$,

$$\begin{aligned} p &= 2.50 \pm 0.06, \qquad & < E_{\rm TOT}^0 > &= 1.77 \pm 0.3\,{\rm GeV}, \\ \sigma_{pp}^{\rm det} &= 13.1 \pm 0.3\,{\rm mb}, \qquad & \chi^2 &= 24.6/15\,{\rm d.o.f.}. \end{aligned} \tag{10.9}$$

Since the configuration is symmetric, the two wounded nucleons produce identical distributions in the detector, so that the spectrum of a wounded nucleon is derived from the proton-proton spectrum by a deconvolution into two equal spectra [87], $p \rightarrow \frac{1}{2}p$; and the WNM prediction for the $\alpha-\alpha$ data is obtained by summing over the convolutions of the wounded nucleon spectrum, weighted by the relative probabilities, r_n, from the "geometrical" calculation. The same principles apply to analyses done in terms of wounded projectile quarks, multiple $N-N$ collisions, etc.

Some technical points of the convolution analysis deserve to be emphasized. The asymptotic slope, b, is the same for all the convoluted spectra, while the mean value increases linearly with n, and the standard deviation about the mean increases as the $\sqrt{n}$. Once the energy is high enough so that the spectrum is dominated by the maximum number of collisions, the asymptotic slope becomes equal to the asymptotic slope of the elementary process. This is clearly illustrated by the slope of the WNM prediction in figure 25b, which is parallel to the $p-p$ spectrum. The slope of the $\alpha-\alpha$ data is quite different from the asymptotic $p-p$ slope and from the WNM prediction. This qualitative feature makes it possible to overcome the uncertainty in the geometrical calculation due to the value assumed for the only free parameter, σ_{NN}. The WNM fails qualitatively in figure 25b, independently of the details of the calculation [70]! The uncertainty of the calculation can become especially acute when, as in the case of figure 25, the observed cross-section in the detector for $p-p$ collisions is only 13 mb, or less than half of the actual cross section[43].

10.1 A new empirical description of soft multiparticle physics.

The use of gamma distributions to fit E_T spectra in $p-p$ collisions was driven by the convolution property for multiple collisions, and also by the fact that the gamma distributions fit the spectra rather well. For instance, the famous NA5 full azimuth E_T spectrum is nicely

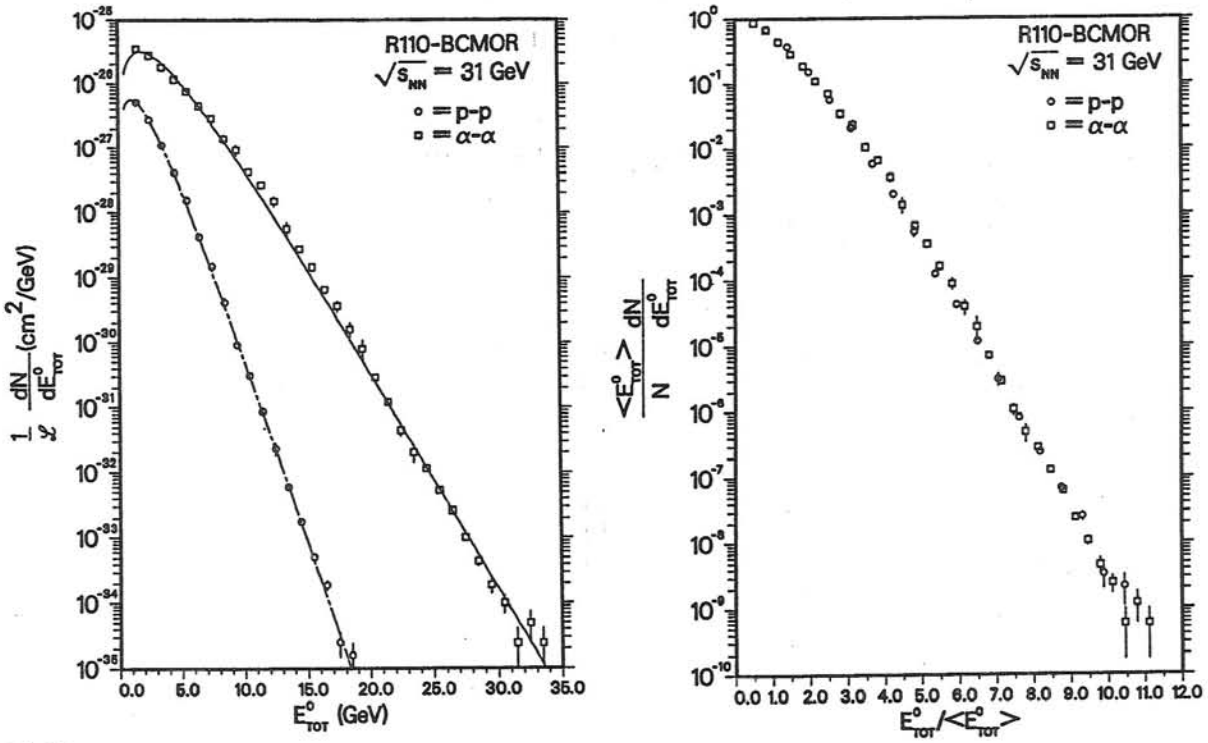

Fig. 26: The $E^0_{\rm TOT}$ spectrum of figure 25a for $\alpha - \alpha$ and $p - p$ interactions: (a) together with fits to a simple gamma distribution. The parameter $p = 2.50 \pm 0.06$ for the $p - p$ data (dot-dash line) and $p = 2.48 \pm 0.05$ for the $\alpha - \alpha$ data (solid line). (b) The same distributions replotted in the scaled energy variable, $z = E^0_{\rm TOT} / < E^0_{\rm TOT} >$, where $< E^0_{\rm TOT} >$ is the average value of the energy for each distribution.

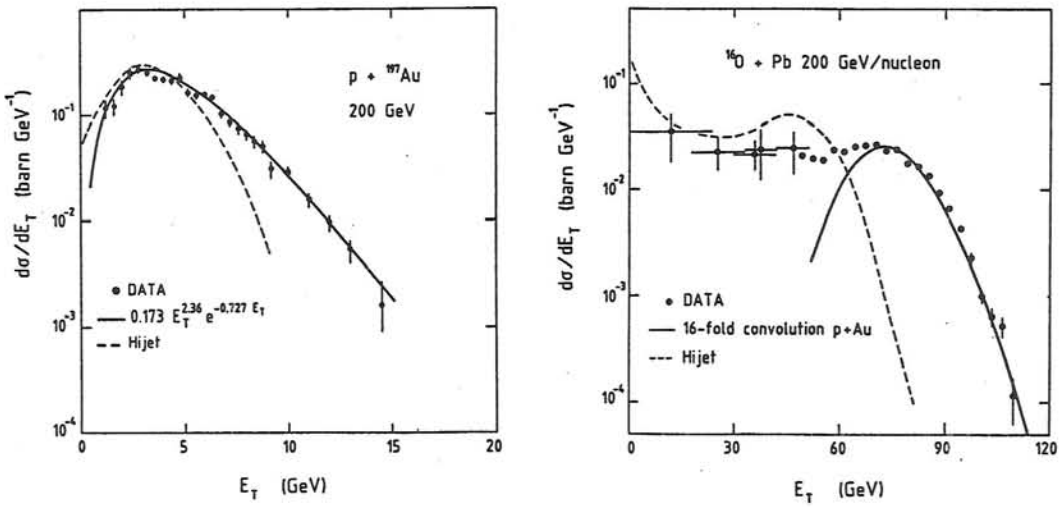

Fig. 27: The mid rapidity transverse energy distribution of $p + Au$ interactions (a) and $^{16}O + Pb$ interactions(b), all at 200 GeV/nucleon, measured in the same apparatus. The dashed curve gives the predictions of a Monte Carlo event generator Hijet [90] for both reactions. The solid curve on the $^{16}O + Pb$ data is the 16-fold convolution of the $p + Au$ fit. The analytical fit to the $p + Au$ data is given on the figure and is a gamma distribution with $p = 3.36$, $\sigma^{\rm det} = 1.44$ barn, and $< E_T >= 4.6$ GeV.

fit by a gamma distribution (recall figure 20). A similar regularity was discovered by the UA5 collaboration [85] in their study of multiplicity distributions in limited regions of rapidity, which are closely related to E_T distributions. A simple function, the negative binomial distribution (NBD), was found to provide an excellent representation of the multiplicity data. In a given pseudorapidity interval, with mean multiplicity $< n >$, the distribution of multiplicity, $P(n)$, can be fit by:

$$P(n) = \frac{-k!}{n!(-k-n)!}\left(\frac{-< n >}{k}\right)^n \left(1 + \frac{< n >}{k}\right)^{-(k+n)} \tag{10.10}$$

where k is a parameter. In the limit of large $< n > /k$, the NBD becomes a gamma distribution in the scaled variable $z = n/ < n >$. Thus, a simple representation exists to describe "soft" multiparticle physics in terms of systematic variations of three parameters: the integrated cross section in a rapidity interval, the mean multiplicity (or $< E_T >$) in the interval, and the parameter k (or p) for the interval. At the present time, the underlying explanation for the success of these simple functions in describing the data remains a mystery [88].

11. A new era — relativistic heavy ion (RHI) interactions

A new era in the study of relativistic collisions involving nuclei opened up in the Fall of 1986 with the advent of beams of high energy heavy ions at CERN and at Brookhaven National Laboratory (BNL). At BNL, beams of ^{16}O and ^{28}Si have been provided at momenta of 14.6 GeV/c per nucleon; while at CERN, beams of ^{16}O and ^{32}S at 200 GeV per nucleon have been used. At both laboratories, some measurements were also made at lower incident momenta.

The main experimental challenge in the study of RHI interactions is to cope with the very high multiplicities produced (recall figure 3). In general, this is not a problem for the highly segmented calorimeters used in the study of E_T distributions, since these are analog devices. So long as the energy response of the detector is linear, and does not saturate, the problem of measuring E_T distributions in nucleus-nucleus interactions is no more difficult than in proton-proton collisions. For this reason, measurements of E_T distributions have been among the first results from this new field, and have played a leading role in the study of the reaction dynamics.

11.1 First results from CERN

The first result in this field was submitted for publication by the NA35 collaboration at CERN in November 1986, barely 2 months after the first 3 day test run [6]. The NA35 experiment consisted of a 2 by 1.2 by 0.72 m^3 streamer chamber in a $1.5T$ superconducting magnet located upstream of a segmented calorimeter (recall figure 9). A contributing factor to the speedy success of this experiment was that all the NA35 calorimeters (except for the intermediate calorimeter covering the angular range $0.3° \leq \theta \leq 2.5°$, and used only as a passive absorber in this measurement) had been used in previous experiments (NA5 [46], NA24 [89]) so that their behavior and calibration was well understood. The differential E_T distributions, as summed from the PPD and Ring Calorimeters, were obtained for the interactions of 200 GeV/nucleon ^{16}O in a Pb target and 200 GeV protons in an Au target, both measured in the same setup (see figure 27). The acceptance covered the lab-pseudorapidity interval $2.3 \leq \eta \leq 3.8$, which excluded the innermost ring of the Ring Calorimeter. At 200 GeV/nucleon incident energy, the

nucleon-nucleon ($N-N$) c.m. energy is $\sqrt{s_{NN}} = 19.4$ GeV and the rapidity of the $N-N$ c.m. system is $y_{cm}^{NN} = 3.03$.

The results from this first ^{16}O test run were very striking. A most interesting and unexpected feature of this data was that the 16-fold convolution of the measured $p+Au$ spectrum beautifully reproduced the high energy edge of the $^{16}O + Pb$ spectrum (see figure 27).

11.2 Closely followed by BNL

These striking results were confirmed at BNL during the commisssioning period of the AGS-Tandem complex in November 1986. A small experiment was assembled using components of E802, one of the three major experiments at the facility[91], and measurements were made using a ^{16}O beam of momentum 14.6 GeV/c per nucleon [92]. The small experiment consisted of a full azimuth electromagnetic shower counter — an array of 96 blocks of lead-glass (PbGl) — placed 1 m downstream of the target. The array was 10 blocks wide by 10 high with a 2 by 2 block hole in the center for the beam to pass through. Each SF5 lead-glass block was 14.5 cm by 14.5 cm in area, and 17 radiation lengths thick (40 cm), viewed end on by a 5 inch photomultiplier. These blocks had been used previously in the CCR and successor experiments at the CERN ISR [55,70].

The PbGl array measured the electromagnetic energy emitted in a laboratory polar angular interval $10° \leq \theta \leq 32°$, corresponding to the laboratory pseudorapidity interval $1.25 < \eta < 2.44$ or roughly -0.5 to +0.7 in the $N-N$ c.m. system. At 14.6 GeV/c per nucleon incident momentum, the $N-N$ c.m. energy is $\sqrt{s_{NN}} = 5.4$ GeV and the rapidity of the $N-N$ c.m. system is $y_{cm}^{NN} = 1.72$. The observed energy was denoted $E_{\rm TOT}^0$, keeping with the ISR[55,70] notation, since the PbGl responds primarily to neutral mesons, π^0 and η^0, which are detected via their two-photon decay. Relativistic charged hadrons ($v/c > 0.8$) also emit Cerenkov light in the PbGl, equivalent to approximately 500 MeV per particle [94], and contribute, in this particular configuration, on the average, about 50% of the observed energy [92,93]. The response of the PbGl to Cerenkov light is linear to $< 1\%$, whatever the source, so that no attempt was made to correct $E_{\rm TOT}^0$ for the Cerenkov light from charged hadrons. The relative scale variation of $E_{\rm TOT}^0$ is better than $\pm 1\%$ for the ^{16}O data and $\pm 5\%$ for the proton data. The absolute scale of $E_{\rm TOT}^0$ was set by calibration in an electron beam.

In figure 28, the spectrum of energy observed in the PbGl is shown for ^{16}O interactions on Au, Cu, and mylar ($C_5H_4O_2$) targets and for positive hadron (80% proton) [92] interactions on an Au target, all measured at 14.6 GeV/c per nucleon in the same experimental arrangement. The PbGl detector covers a restricted pseudorapidity interval near y_{cm}^{NN}. Because of the restricted acceptance, the transverse and total energy recorded in the detector are highly correlated. If the transverse energy density in pseudorapidity is constant over the detector, then the transverse energy and total energy observed in the detector are simply related by a contant factor of $< \sin\theta >= 0.29$, which seems to be the case[81]. Because the segmentation of the PbGl was relatively crude in this small experiment, the transverse resolution is difficult to unfold, so the $E_{\rm TOT}^0$ spectrum is used for further discussion.

The $E_{\rm TOT}^0$ spectrum for $^{16}O + Au$ shows an initial fall-off and then a broad plateau, a peak centered at 40 GeV and then a sharp drop-off until the yield runs out at ~ 70 GeV (see figure 28). The $^{16}O + Cu$ data also show evidence of considerable energy emission, even though the

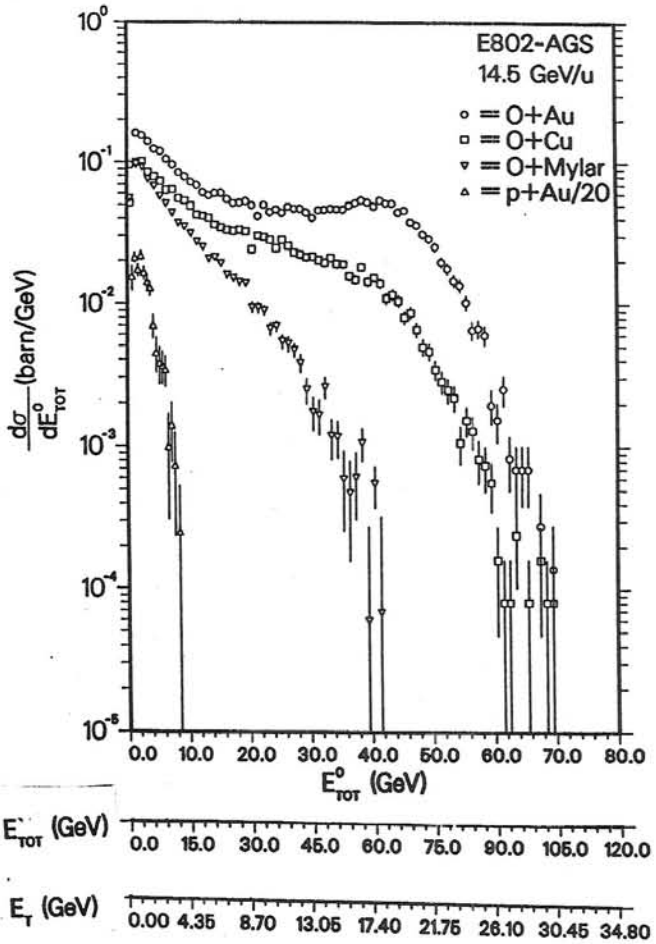

Fig. 28: Differential cross sections in $E^0_{\rm TOT}$, the energy recorded in the PbGl, for ^{16}O interactions on Au, Cu and Mylar ($C_5H_4O_2$) targets and for proton interactions on an Au target. The $p + Au$ cross section has been divided by a factor of 20 for clarity of presentation. The two lower scales on the figure correspond approximately to the total energy and transverse energy falling on the detector and have been estimated with an average correction $E^0_T \simeq 0.29\, E^0_{\rm TOT}$, $E_T \simeq 3/2\, E^0_T$, as discussed in the text [92,93].

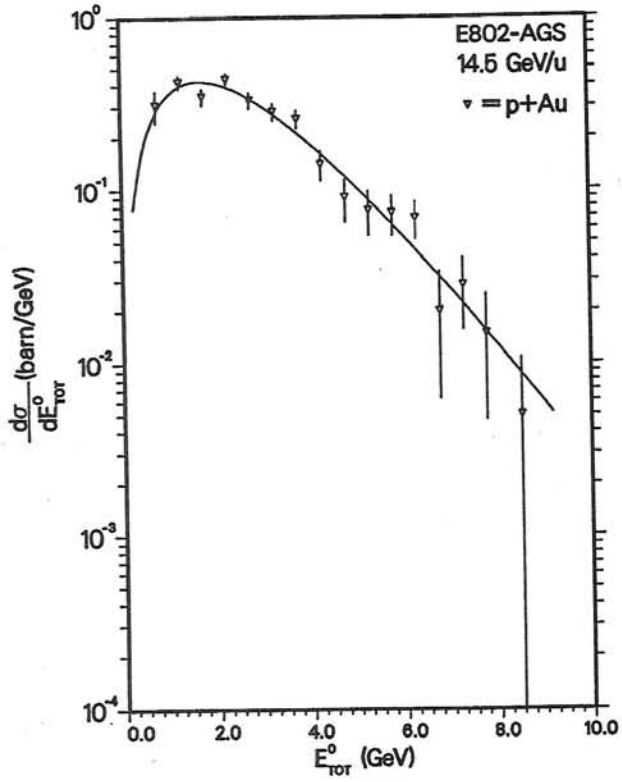

Fig. 29: Fit [92,93] of the $p + Au$ spectrum to a single gamma distribution (solid curve) with $\sigma^{\rm det} = 1.44 \pm 0.77$ barn, $b = 0.95 \pm 0.09 GeV^{-1}$, $p = 2.60 \pm 0.24$, with average energy $< E^0_{\rm TOT} >= p/b = 2.73 GeV$.

maximum thickness of a Cu nucleus is only $\sim 2/3$ that of Au. It is of particular interest that the edges of the $^{16}O + Cu$ and $^{16}O + Au$ spectra become virtually identical above 50 GeV if the Cu cross section is multiplied by a factor of ~ 6.

These features can be described by a simple, geometrical model, motivated by the original NA35 observation that the high energy edge of the $^{16}O + Pb$ spectrum is just the 16-fold convolution of the $p + Au$ spectrum. This idea was extended to provide a description of the entire $^{16}O + Cu$ and $^{16}O + Au$ spectra in E802 [92,93,95]. The observed $p + Au$ spectrum was fit to a gamma distribution (figure 29) and then convoluted from 1 to 16 times, with weights for the n-fold convolutions obtained from a geometrical calculation which averaged over the impact parameter of the nucleus-nucleus scattering to obtain the distribution in the number of projectile nucleons which interact at least once in the target. An $N - N$ inelastic cross section of 30 mb was used in the calculation, corresponding to an absorption mean free path of ~ 2.2 fm. Excellent representations of both the $^{16}O + Au$ and $^{16}O + Cu$ spectra were obtained from this "wounded-projectile-nucleon" (WPN) model (see figure 30). It then appears that the peak in the $^{16}O + Au$ spectrum and the identical shape of the high-energy edges of the $^{16}O + Au$ and $^{16}O + Cu$ spectra arise from events in which all 16 projectile nucleons interact.

Although the WPN model seems quite reasonable and fits the $E^0_{\rm TOT}$ data rather well, the analysis contains some potential inconsistencies. The observed $p + Au$ spectrum, which is necessarily averaged over all impact parameters, was used for the 16-fold convolution, whereas, it would seem that a "centrally averaged" $p+Au$, or $p+Cu$ spectrum would be more appropriate. Also, the WPN model is in serious contradiction with the understanding of relativistic nuclear interactions gleaned from proton-nucleus collisions at higher energies, where nuclei appear to be relatively transparent.

A simple resolution of these inconsistencies is to presume that an incoming 14.6 GeV/u nucleon loses most of its energy in the first few collisions. The subsequent lower energy collisions are unlikely to produce energy observable in the PbGl (neutral-mesons). In this way the energy emitted in a $p + A$ interaction would not depend much on impact parameter or nuclear size, and it is appropriate to use the experimental $p + Au$ spectrum to analyze the $^{16}O + Cu$ and $^{16}O + Au$ data. The maximum energy observed in these reactions occurs when all sixteen projectile nucleons interact: i.e., for events in which the impact parameter is sufficiently small to allow complete overlap of the $^{16}O + Au$ or $^{16}O + Cu$ nuclei. The cross sections for maximum energy deposit in Au and Cu are then in the ratio of these impact parameters squared, $\left[R(Au) - R\left(^{16}O\right)\right]^2 / \left[R(Cu) - R\left(^{16}O\right)\right]^2$, a factor of $\sim$ 5, which is close to the measured factor of ~ 6.

The observation that the maximum energy emitted in $^{16}O + Cu$ interactions is essentially the same as in $^{16}O + Au$ interactions, together with the success in reproducing the observed ^{16}O spectra from the $p + Au$ spectrum by a simple geometrical model, was cited as compelling evidence by the E802 collaboration [92] that ^{16}O projectiles at 14.6 GeV/c per nucleon can be sufficiently stopped in Cu so that pion emission effectively ceases.

11.3 Further E_T results at BNL and CERN

Additional results in support of "energy stopping" at BNL energies are provided by measurements from the full setup[91] of E802 , for ^{28}Si interactions in a variety of targets. For this

series of measurements, the PbGl was composed of 245 six inch square SF5 blocks, located 3 m downstream of the target, covering a laboratory polar angular interval of 8.0° to 32.0° , or $1.3 < \eta_{lab} < 2.5$ in pseudorapidity. This is roughly the same η coverage as the small experiment, with 3 times finer segmentation. However, only 1/2 of the azimuth was covered; the other half of the azimuth being occupied by a magnetic spectrometer with full particle identification[96].

Because of the excellent segmentation in the full setup, measurements of the energy flow in the PbGl can be presented interchangeably in terms of either the total energy, E_{TOT}^{PbG}, or the transverse energy E_T^{PbG} observed in the detector. (Previously, these quantities had been denoted E_{TOT}^0 and E_T^0). These variables are highly correlated: the distribution in $E_T^{PbG}/E_{TOT}^{PbG} \equiv < \sin\theta >_{eff}$ is Gaussian, with an rms width of $\sim$ 10% of the mean value of 0.285 ± 0.003. The systematic variation of $< E_T^{PbG}/E_{TOT}^{PbG} >$ as a function of E_{TOT}^{PbG} is less than 5 %

Although the data analysis is not yet complete, conclusions on "energy stopping" can be drawn already from the "trigger" distributions, figure 31, for ^{28}Si interactions on ^{27}Al, ^{64}Cu, ^{108}Ag and ^{197}Au targets. These distributions have not been target out subtracted, and may differ in absolute scale by 5 % compared to previous data[93]. However, the relative scale is better than 1 % for all targets; and the target empty correction is negligible for $E_T^{PbG} > 2$ GeV, and is the same for all the targets, which are 3 % of an interaction length for this figure. The upper edges of the $Si + Cu$ and $Si + Ag$ spectra differ from the $Si + Au$ spectrum by roughly 15 % , and 5 % in E_T^{PbG}, whereas the target nuclear thicknesses differ by 40 % and 20 % respectively . It should be noted that E_T spectra are very sensitive to the region of pseudorapidity in which they are measured[97,91]. However, E_T spectra measured in the central rapidity region at AGS energies appear to differ qualitatively from comparable spectra measured at CERN.

The NA35 E_T spectra from the full ^{16}O run in Fall 1986 [98] are shown in figure 32 for four targets, Au, Ag, Cu and Al. The acceptance for these data covers the central pseudorapidity range $2.28 < \eta < 3.94$, where the $dE_T/d\eta$ distribution is expected to be relatively constant. All the spectra are characterized by a "rapidly varying cross section for peripheral collisions, followed by a long plateau which ends in a steep fall-off" [98]. The upper edges of the spectra show a substantial increase in E_T with increasing target nuclear size. Particularly striking in comparison to the E802 data (figures 28, 31) is that the NA35 data (figure 32) indicate $\sim$ 35% more energy emission for $^{16}O + Au$ interactions compared to $^{16}O + Cu$. The spectra in electromagnetic transverse energy, E_T^{em} were also obtained by NA35 from the PPD (recall Fig. 9). The NA35 distributions in (total) transverse energy, E_T, and the electromagnetic component only, E_T^{em}, show essentially the same characteristics.

Some observations on the systematic errors of E_T measurements can be made from the NA35 data. A comparison of the $^{16}O + Au$ E_T spectrum in figure 32 [98] with the $^{16}O + Pb$ E_T spectrum in figure 27 [6] shows $\sim$ 40% more E_T in figure 32, compared to figure 27, with only a 10% increase in acceptance. These data were taken by the same group, in the same detector, at the same incident momentum, only 2 months apart. This discrepancy exceeds considerably the systematic error on the overall E_T scale, which is estimated to be 15% .

In spite of systematic differences between data sets, which happens to be obvious in the case of NA35, many useful conclusions can be drawn from such data by making comparisons within sets of measurements which all share the same overall systematic effects. Two comparisons

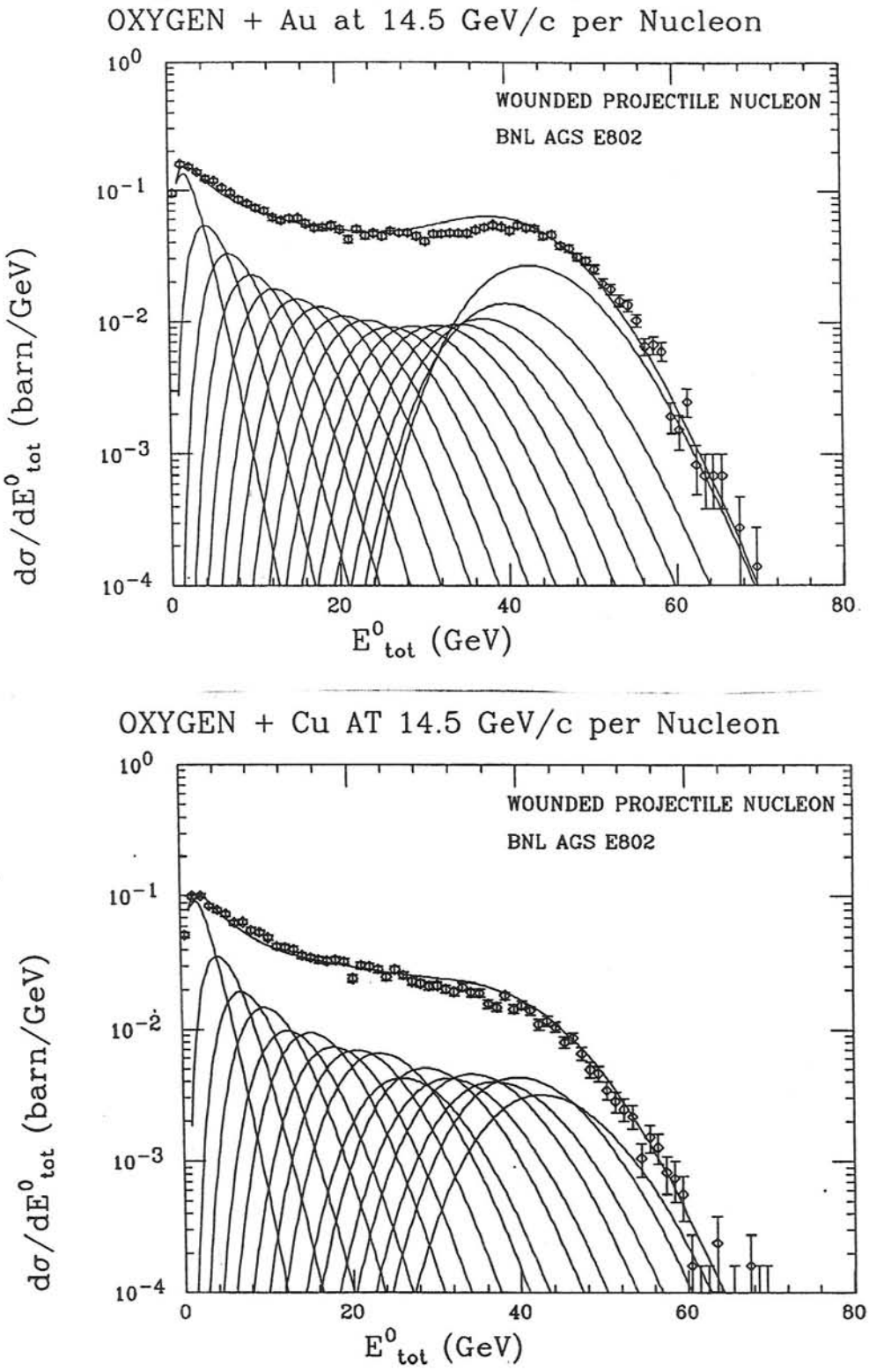

Fig. 30: The $E^0_{\rm TOT}$ spectra of figure 28 for ^{16}O interactions on Au (a) and Cu (b) together with the sum of 1 to 16-fold convolutions of the measured $p + Au$ spectrum weighted according to the probability for 1,2,...16 of the projectile nucleons to interact in the target. The individual components of the sum are also shown. The curves have been normalized to the observed cross-section for each target, $\sigma^{\rm det} = 3.27$ barn for $^{16}O + Au$ and $\sigma^{\rm det} = 1.66$ barn for Cu [92,93].

emphasized by the NA35 collaboration are the ratio of E_T emission at 60 GeV/nucleon incident energy to that at 200 GeV/nucleon, and the ratio of E_T^{em} emission in ^{32}S and ^{16}O interactions at 200 GeV/nucleon in an Au target.

The E_T and E_T^{em} spectra were obtained by NA35 at 60 GeV/u as well as at 200 GeV/u. It should be noted that the NA35 calorimeters were moved for the 60 GeV/u run, so that the pseudorapidity acceptance covered $2.08 < \eta < 3.72$, in an attempt to remain relatively centered about $y_{cm}^{NN} = 2.43$ at $\sqrt{s_{NN}} = 10.7$ GeV. A spectacular illustration of the simple scaling of the NA35 E_T spectra for the two different c.m. energies is given in figure 33, where the $^{16}O + Au$ E_T spectrum at 60 GeV/nucleon is compared to the corresponding 200 GeV/nucleon spectrum scaled down in E_T by a constant factor of 0.58. The excellent agreement in spectral shapes in figure 33 tends to imply that only the $< E_T >$ changes with $\sqrt{s_{NN}}$ over this range, with the gamma distribution shape parameter p remaining constant (recall figure 27), i.e. another example of KNO scaling[30].

Another first by NA35 was a study of the dependence of transverse energy production on projectile mass at fixed incident energy/nucleon in the same detector [98]. In figure 34, the first data from the Fall 1987 200 GeV/nucleon ^{32}S run at CERN is compared to the corresponding $^{16}O+Au$ data. The transverse electromagnetic energy E_T^{em} seen by the PPD shows an increase of $\sim 77\%$ for central collisions, for a doubling of the projectile mass. Thus, the original observation that the upper edge of the $^{16}O + Pb$ spectrum was simply the 16-fold convolution of the $p + Au$ spectrum [6] (recall figure 27) breaks down for the ^{32}S projectile [98]. This latter observation (figure 34) is more in accord with the previous understanding of the interactions of nuclei in this energy range, where transparency was the dominant feature [58]. The lack of transparency at lower energies was also not unexpected [99].

12. Measurements of the Forward Energy—E_F

The correlation of forward and transverse energy was exploited, primarily by the WA80 Collaboration at CERN[101], to analyze the E_T distributions in $A+A$ interactions without recourse to $p - p$ or $p + A$ data. The usefulness of forward energy (E_F) measurements rests on the assumption that the forward calorimeter detects only projectile spectators, thus making the forward energy an extremely sensitive probe of geometry of the $A + A$ collision. Thus, the solid angle of the forward calorimeter is set to a very small forward cone around the beam direction $\eta \gtrsim Y^{beam}$. The ideal aperture would allow the zero-degree-calorimeter (ZDC) to measure the full kinetic energy of the projectile, in the case of no interaction, and to measure zero energy for any nucleon in the projectile that suffered an inelastic collision. Thus the energy recorded in the ZDC should be proportional to the number of non-interacting nucleons ("spectators") in the projectile. In the real world the situation is somewhat more complicated, since some of the interacting nucleons may suffer very little transverse deflection, and remain within the ZDC accceptance; or some of the spectator nucleons may have unexpectedly large transverse deflection and fall outside of the ZDC.

The energy distributions measured in a ZDC offer a different sensitivity to the nuclear collision geometry than E_T measurements; and the interpretation of E_F spectra would seem more straightforward in the ideal case, since they should only depend on whether the projectile

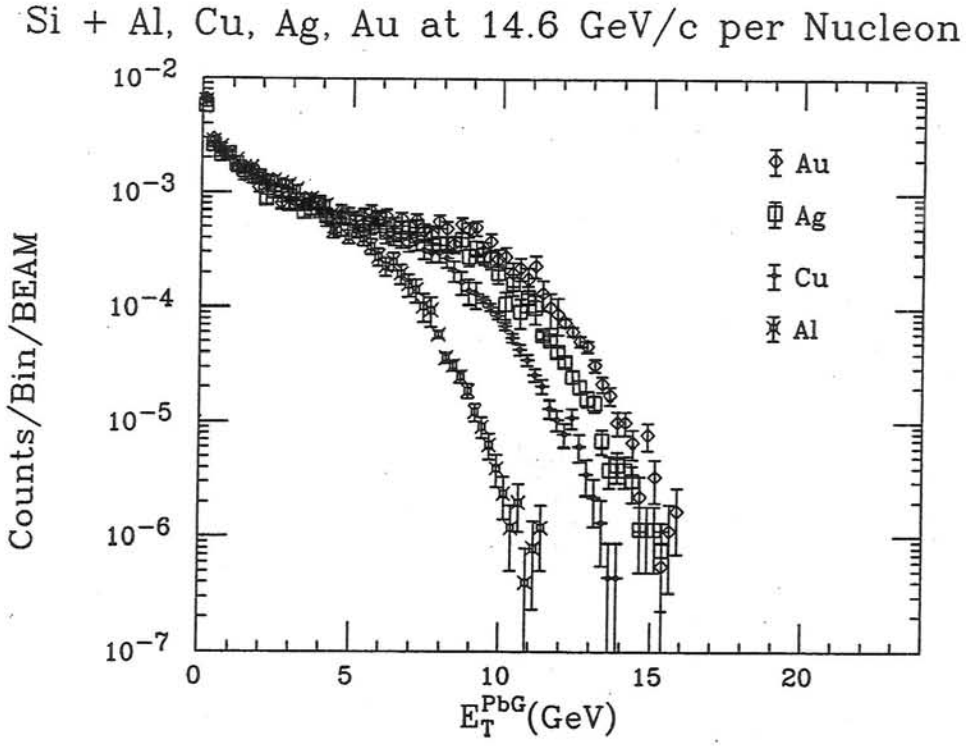

Fig. 31: Preliminary E802 E_T^{PbG} spectra in the 1/2 azimuth PbGl for interactions of 14.6 GeV/c per nucleon ^{28}Si projectiles in targets of *Au*, *Ag*, *Cu* and *Al*. Note that the target-out background has not been subtracted in this figure; and that the data are not in cross section units, but are in units more natural for a "trigger" counts per bin per incident beam particle[105].

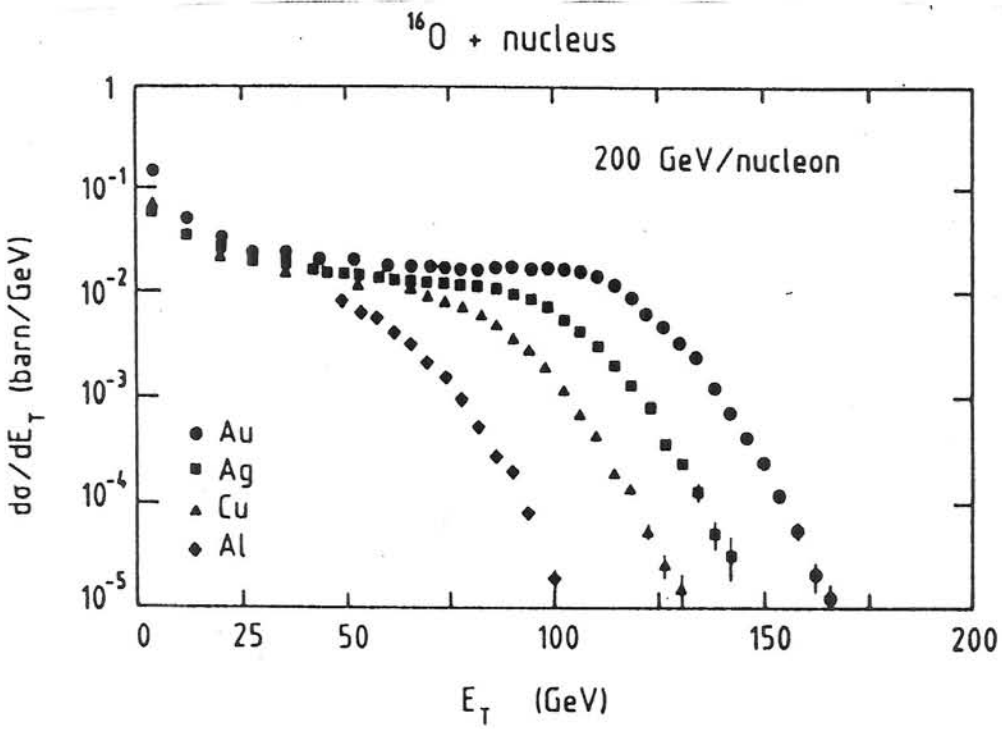

Fig. 32: Transverse energy spectra for ^{16}O on *Au* (circles), *Ag* (squares), *Cu* (triangles) and *Al* (diamonds) at 200 GeV/nucleon as seen in the NA35 acceptance [98].

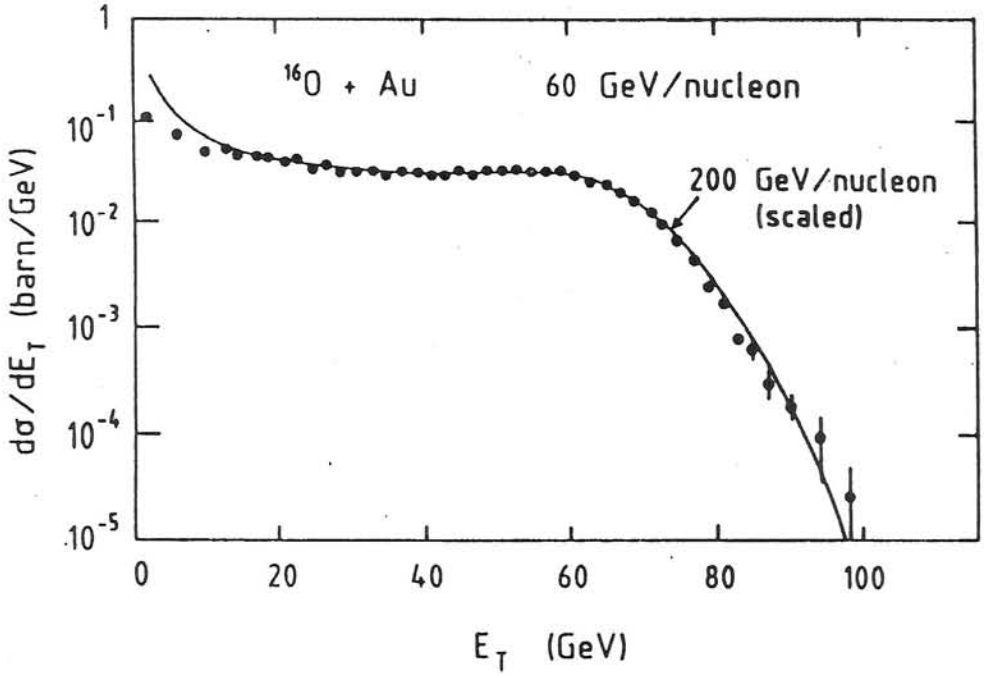

Fig. 33: NA35 transverse energy spectrum for $^{16}O + Au$ for 60 GeV/nucleon (circles) together with a fit (solid line) to the corresponding spectrum at 200 GeV/nucleon scaled down in E_T by a factor of 0.58 [98].

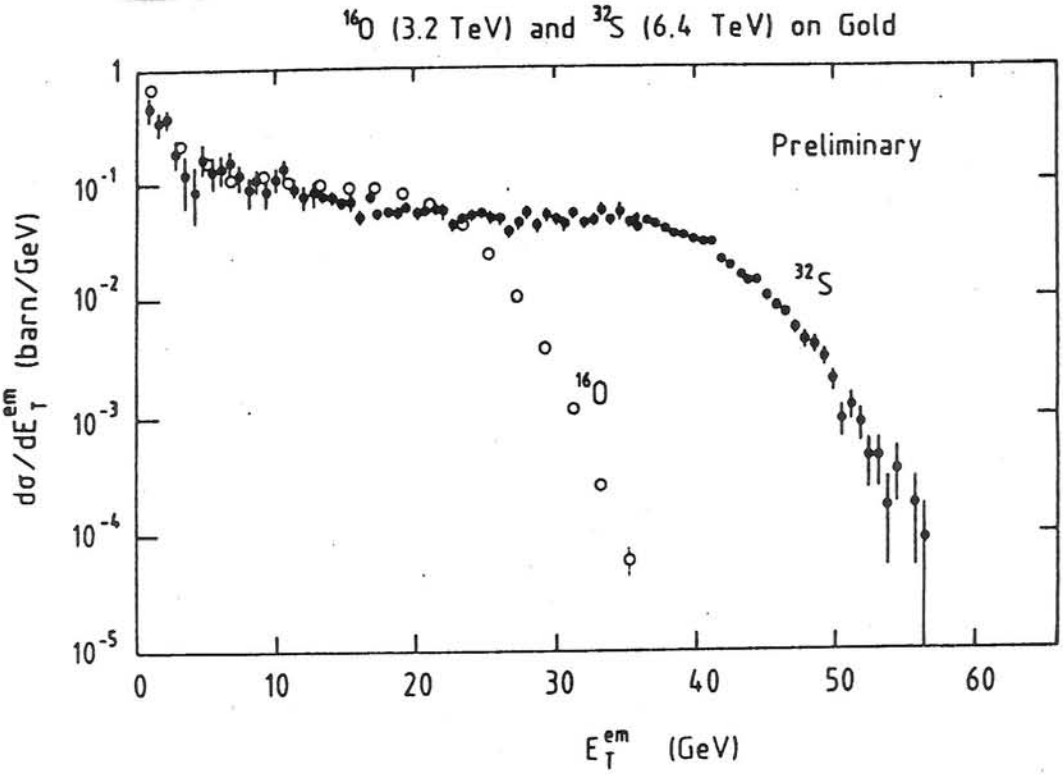

Fig. 34: Differential cross section $d\sigma/dE_T^{em}$, seen in the NA35 PPD for $^{32}S + Au$ (solid circles) with the corresponding spectrum for $^{16}O + Au$ (open circles) for comparison at 200 GeV/nucleon. The ^{32}S spectrum is preliminary [98].

nucleons interact and not how or how many times they interact. The ZDC spectra from the WA80 Collaboration [101] for ^{16}O interactions at 60 and 200 GeV/nucleon are shown in figure 35a. The full beam kinetic energy should appear at 960 (3200) GeV for the 60 (200) GeV/nucleon data but has been suppressed by a "minimum-bias" trigger requirement that less than 88% of the full projectile energy be measured by the ZDC. The $^{16}O + ^{12}C$ data at 200 GeV/nucleon show essentially no cross section for events depositing a small amount of energy in the ZDC because, even in the most central collision, there are many projectile "spectators" since the target nucleus is too small to fully overlap the projectile. By contrast, a pronounced peak is seen at small ZDC energies in the data from $^{16}O + Au$ interactions, where full overlap does occur on central collisions, and there is a large probability for all the projectile nucleons to interact. The acceptance of the ZDC was effectively more restrictive at 60 GeV/nucleon, and closer to the ideal, because the WA80 calorimeters remained fixed for the two incident energies so that the ZDC acceptance ($\eta > 6.0$) effectively moved considerably forward of $Y^{beam} = 4.85$ at 60 GeV/nucleon. The peak in the $^{16}O + Au$ data becomes more pronounced and moves to zero E_{ZDC}, at 60 GeV/nucleon, indicating the absence of projectile spectators for a large fraction of the interactions. An increase of events with low values of $E_{\rm ZDC}$ is also observed for the Ag and Cu targets. The authors of WA80 compare their data to the Lund-FRITIOF Monte Carlo calculation [68] (solid line on figure 35a), and it is amusing to note that the agreement is not particularly good for the lighter targets, where "there is a clear tendency for FRITIOF to underestimate the cross section for small values of $E_{\rm ZDC}$" [101]. This tendency is more apparent at 60 GeV/nucleon.

12.1 Correlations between transverse energy E_T and forward energy E_F.

A new diagnostic tool in relativistic heavy ion interactions has been provided by the study of the correlation between forward and transverse energy emission. At first glance, the correlation appears to be a trivial consequence of energy conservation: the energy not observed in the forward direction will be observed as "transverse energy" [102]. Early measurements[98,101] clearly demonstrated the anti-correlation between E_T and $E_{\rm ZDC}$; and confirmed the intuitive notion that "central collisions" exhibit small forward energies and large transverse energies. However, the detailed shape of the correlation curve, as a function of projectile and target atomic masses, can provide stringent constraints on the reaction dynamics of collisions in nuclei.

The energy recorded in an ideal zero-degree-calorimeter corresponds to the number of projectile "spectators", and thus directly determines the number of projectile "participants". The participating projectile nucleons may make more than one $N - N$ collision in the target nucleus, with the number of successive collisions being proportional to the nuclear thickness. The relationship between wounded projectile nucleons and $N - N$ collisions, or wounded projectile nucleons and wounded target nucleons, is a characteristic, simply, of the nuclear geometry of the interaction, and is easily computed. The data then may be directly compared to the geometrical calculations to see which, if any, model of the fundamental element of E_T emission in nuclear collisions is preferred.

The forward-transverse correlation measurements at the incident energies available at CERN seem to track very well with the nuclear participant geometry. The WA80 Collaboration [101] divides their $< E_T >-E_{\rm ZDC}$ correlation data by the corresponding nuclear participant geometry

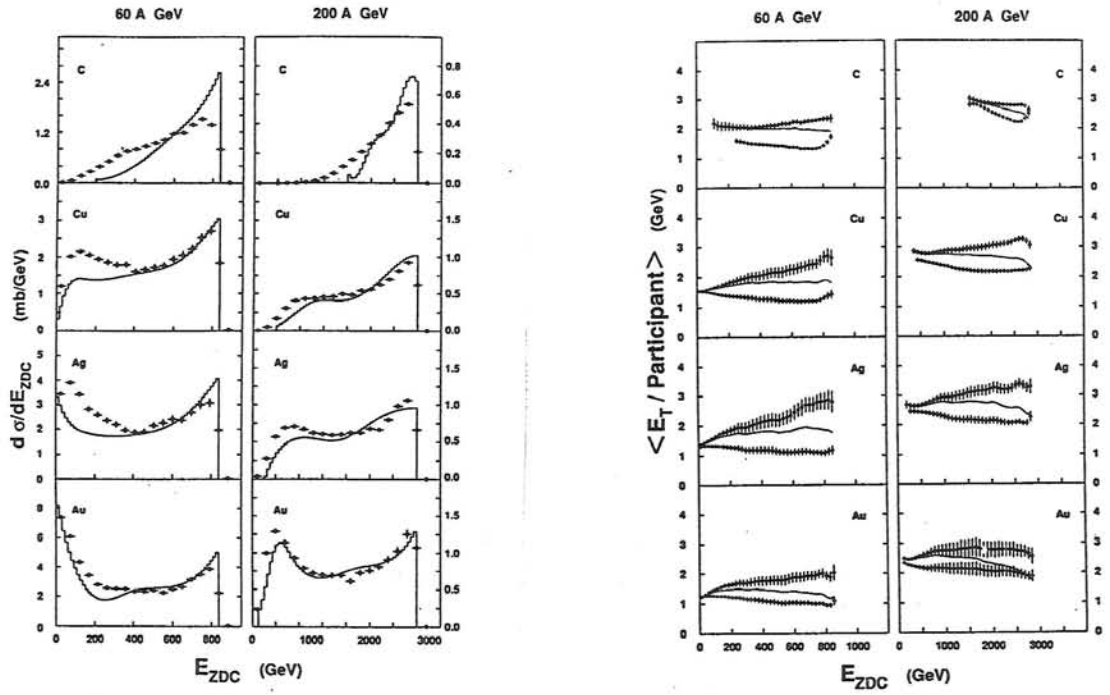

Fig. 35: (a) Energy spectra measured in the WA80 zero-degree-calorimeter (filled circles) in ^{16}O induced reactions. The histograms give the results of the Lund Model (FRITIOF) [68,101]. (b) Determination, by WA80, of the average values of E_T/participant as a function of the energy measured in the zero-degree-calorimeter. The pseudorapidity range used in the E_T determination is $1.6 < \eta < 5.5$. The solid line and the open circles represent different nuclear geometry calculations (see [101] for details).

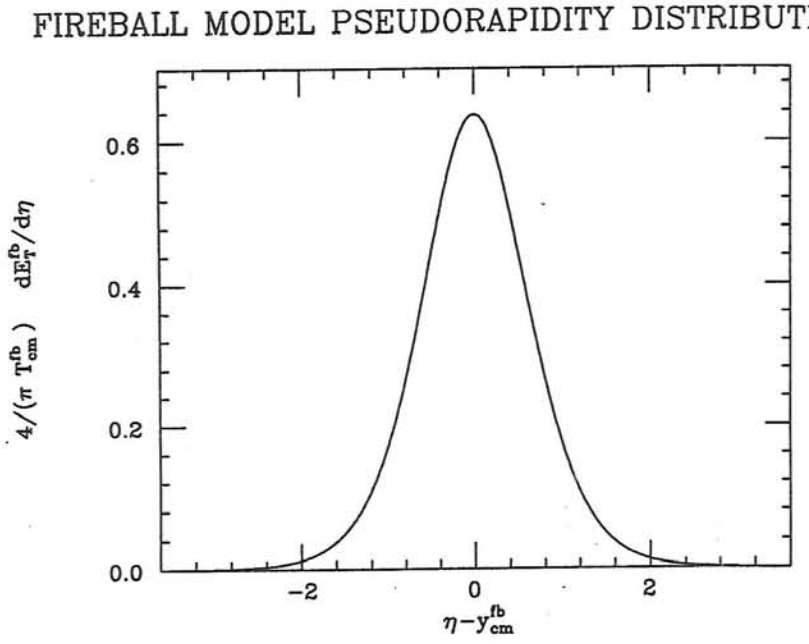

Fig. 36: Universal pseudorapidity distribution of $dE_T/d\eta$, in the fireball model, relative to the rapidity of the fireball center of mass.

calculation to obtain the $< E_T/\text{Participant} >$ integrated over their pseudorapidity acceptance (see figure 35b). While the 200 (60) GeV/nucleon data appear to be consistent with a constant $< E_T/\text{Participant} >$ of 2 (1.3) GeV, the conclusion is not compelling, due to the large systematic uncertainty of the "nuclear geometry" calculations. However, a new analysis of these data, including results of 200 GeV/nucleon ^{32}S interactions in the same targets, appears to be compatible with a constant value of $< E_T/\text{Participant} > \simeq 2$ GeV, in the pseudorapidity interval $2.4 < \eta < 5.5$, for all targets and both projectiles at 200 GeV/nucleon [103]. This preliminary result would be striking corroboration of the WNM for $< E_T >$ at CERN energies, if it holds up; and an interesting extension would be to see whether the detailed shapes of the E_T spectra also support a WNM explanation.

Unlike the results at CERN energies, the forward-transverse energy correlation measurements of the E802 collaboration [105,104], for 14.6 GeV/c per nucleon ^{28}Si interactions do not simply follow a nuclear geometry calculation, either wounded projectile nucleons as for $E^0_{\rm TOT}$ (recall figure 30) or the WNM. No doubt, the forward-transverse energy correlation provides enhanced sensitivity to the different models of E_T production in relativistic nuclear collisions; and will continue to be exploited. However, this is a new technique, unique to the field of Relativistic Heavy Ion interactions; and the analysis and interpretation of the data (in the real world) is more complicated than in the idealized case, and has taken longer than anticipated to complete.

13. Pseudorapdity distributions, $dE_T/d\eta$ and the issue of "nuclear stopping"

The issue of "nuclear stopping" continually surfaces in discussions of the data from relativistic heavy ion interactions. The degree of "nuclear stopping" is an important element in estimates of the temperature, energy density and baryon density of the large volume of hot, compressed, nuclear matter remaining after a "central" nuclear collision. The formation of a new state of matter, the Quark Gluon Plasma (QGP) is expected to take place when the temperature exceeds a critical value $T_c \gtrsim 250$ MeV, or the baryon or energy density exceeds the value 1.0 to 3.0 GeV/fm^3. [2,3]

Pseudorapidity distributions of transverse energy emission play an important role in the discussions of "nuclear stopping" because one of the simplest concepts of stopping is that the projectile and target "participants" merge into a hadronic "fireball", which then decays isotropically [6,51,98,101,97]. This would be quite distinct from the normal "longitudinal phase space" behavior of the "soft" multiparticle production processes that predominate in high energy collisions, in which produced particles have limted transverse momentum ($< p_T > \simeq \frac{1}{3}$ GeV/c) and very broad and flat rapidity distributions.

13.1 The Fireball Model—I

The "fireball model" contains three distinct assumptions.

- The number of participants is calculated assuming a head-on, collision in which the projectile interacts with all nucleons in a "cylinder cut through the center of the target nucleus" [97]. For spherical nuclei, with B nucleons in the projectile and A in the target ($B \leq A$), the number of projectile participants is $n^P_{\rm part} = B$ and the

number of target participants is given by

$$n_{\text{part}}^{T} = A\left(1 - \left(1 - (B/A)^{\frac{2}{3}}\right)^{\frac{3}{2}}\right). \tag{13.1}$$

- The center-of-mass system and the available c.m. kinetic energy T_{cm}^{fb} are calculated as if a solid projectile, of mass B nucleons, containing the full beam energy, interacted with a solid target of mass n_{part}^{T} nucleons.
- The total available c.m. energy T_{cm}^{fb} is dissipated by isotropic emission in the fireball rest frame.

Thus in the fireball model, the relevant symmetry point is not the rapidity of the $N-N$ c.m. system, y_{cm}^{NN}, but the rapidity of the $B + n_{\text{part}}^{T}$ fireball, y_{cm}^{fb}. Also, the "isotropic" assumption has a very neat and striking consequence: the pseudorapidity distribution of transverse energy emission, in the fireball model, is a universal curve about the symmetry point, $\eta = y_{cm}^{fb}$, for all projectiles, targets, and incident energies (see figure 36).

It is instructive to work out this distribution from the isotropic probability for energy emission in the fireball c.m. system:

$$\frac{d\mathcal{P}(\theta^*, \phi^*)}{d\Omega^*} = \frac{1}{4\pi} = \frac{d\mathcal{P}(\theta^*, \phi^*)}{\sin\theta^*\, d\theta^*\, d\phi^*} \tag{13.2}$$

Thus,

$$\frac{d\mathcal{P}}{\sin\theta^*\, d\theta^*} = \frac{1}{2} \tag{13.3}$$

The probability is evidently normalized. The available energy distribution is:

$$\frac{dT}{d\theta^*} = T_{cm}^{fb}\frac{d\mathcal{P}}{d\theta^*} = \frac{T_{cm}^{fb}}{2}\sin\theta^* \tag{13.4}$$

Now, use the definition of E_T :

$$\frac{dE_T}{d\theta^*} \equiv \sin\theta^*\frac{dT}{d\theta^*} = \frac{T_{cm}^{fb}}{2}\sin^2\theta^* \tag{13.5}$$

Integrate over θ^* to find the total $E_T^{\text{integrated}}$

$$E_T^{\text{integrated}} = \int_0^{\pi}\frac{dE_T}{d\theta^*}\,d\theta^* = \int_0^{\pi} d\theta^*\,\frac{T_{cm}^{fb}}{2}\left(\frac{1-\cos 2\theta^*}{2}\right) = \frac{\pi}{4}T_{cm}^{fb} \tag{13.6}$$

The pseudorapidity distribution of E_T is determined from Eq. (13.5)

$$\frac{dE_T}{d\eta} = \frac{dE_T/d\theta^*}{d\eta/d\theta^*} \tag{13.7}$$

where

$$\eta = -\ln\tan\theta^*/2 \qquad \frac{d\eta}{d\theta^*} = -\frac{1}{\sin\theta^*} \tag{13.8}$$

so that

$$\frac{dE_T}{d\eta} = -\frac{T_{cm}^{fb}}{2}\sin^3\theta^* \tag{13.9}$$

whereupon , from Eq (2.5)

$$dE_T^{fb}/d\eta = \frac{T_{cm}^{fb}}{2}\ \mathrm{sech}^3\left(\eta - y_{cm}^{fb}\right) \tag{13.10}$$

A cultural division between nuclear and particle physicists arises when it comes to discussing the pseudorapidity distribution of charged multiplicity in the fireball model. The particle physicist says that $< P_T >$ is constant, so that

$$dn^{fb}/d\eta = \frac{1}{< P_T >} dE_T^{fb}/d\eta$$

i.e. the $dn/d\eta$ and $dE_T/d\eta$ distributions are identical. The nuclear physicist says that the temperature is constant, which implies that the $< E >$ per particle is constant, so that

$$dn^{fb}/d\eta = \frac{1}{< E >} dE^{fb}/d\eta = \frac{T_{cm}^{fb}}{2 < E >}\ \mathrm{sech}^2\left(\eta - y_{cm}^{fb}\right) \tag{13.11}$$

This latter point of view is correct in the strict thermal model.

Another, less unique, conseqence of the fireball model is that the symmetry point, y_{cm}^{fb}, the position of the maximum $dE_T/d\eta$, should move systematically backwards in a $B+A$ interaction, as the target atomic mass A increases. The prediction of the shift in the position of $dE_T/d\eta|_{\max}$ is quantitatively precise in the fireball model; but is qualitatively predicted in all multiple collision models, since the rapidity of an excited nucleon will decrease, as its effective mass or transverse momentum increases, even without any loss of energy [106].

Although the fireball model will turn out to have little applicability in the regime of relativistic heavy ion collisions presently under study, its predictions serve as a guide on how to characterize and evaluate measured pseudorapidity distributions. It is convenient to characterize the pseudorapidity distributions by $\eta|_{\max}$ and $dE_T/d\eta|_{\max}$, the position and value of the maximum of the distribution, and by $\Delta\eta_{\mathrm{FWHM}}$, the full width of the distribution at half maximum. For most pseudorapidity distributions, the integral of $dE_T/d\eta$ over all η is well approximated by

$$\int_{\text{all }\eta} d\eta\ dE_T/d\eta \equiv E_T^{\text{integrated}} \simeq dE_T/d\eta|_{\max} \times \Delta\eta_{\mathrm{FWHM}}. \tag{13.12}$$

In the fireball model, $dE_T/d\eta|_{\max} = T_{cm}^{fb}/2$, $E_T^{\text{integrated}} = \frac{\pi}{4} T_{cm}^{fb}$, and the FWHM of the distribution is universal: $\Delta\eta_{\mathrm{FWHM}}$=1.41. For the "particle physicist" the multiplicity distribution has the same FWHM as the E_T distribution; for the "nuclear" physicist, $dn/d\eta$ has $\Delta\eta_{FWHM}$=1.75.

13.2 The Fireball model fails—$dn/d\eta$ isn't universal

A direct comparison of pseudorapidity distributions for ^{16}O interactions at 14.5 GeV/c per nucleon, 60 GeV/nucleon and 200 GeV/nucleon is available, for charged particle multiplicity, from E808 [109], an emulsion experiment at the AGS and CERN. The distributions of shower particles ($v/c > 0.7$) measured in central collisions of ^{16}O with $AgBr$ are shown in figure 37. There is approximate scaling in the target fragmentation region and the distributions show a longitudinal expansion to larger η as the projectile energy increases. These distributions appear to be very symmetric about y_{cm}^{NN}, for all 3 incident energies, and do not indicate any backward shift of $\eta|_{\max}$, as seen in comparable results from $p+A$ interactions [59] (recall figure 21), although

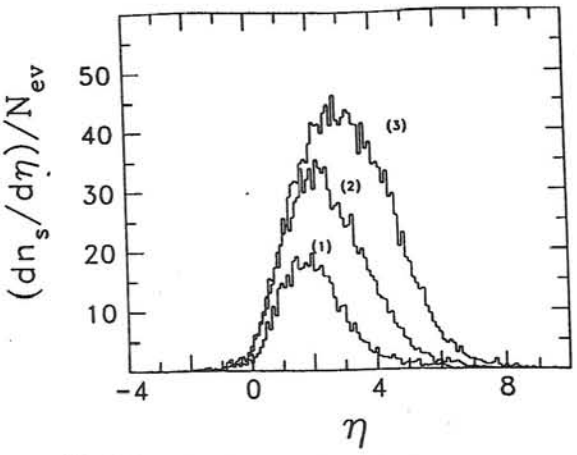

Fig. 37: Normalized pseudorapidity distributions of shower particles ($v/c > 0.7$) from central $^{16}O + Ag/Br$ interactions in an emulsion at three energies (1) 14.6, (2) 60, and (3) 200 GeV/nucleon. The central selection corresponds to $\sim 30\%$ of the Ag/Br interaction cross section[109].

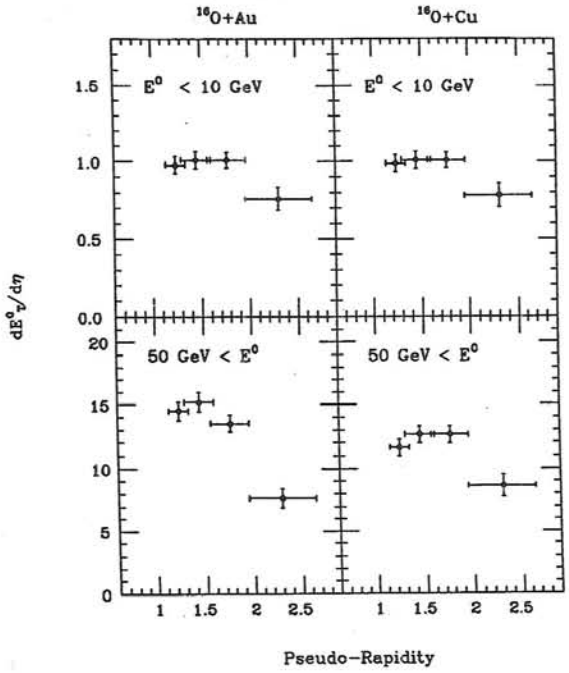

Fig. 38: The pseudorapidity dependence of the transverse energy recorded in the E802 full azimuth PbGl detector for 14.5 GeV/c per nucleon ^{16}O interactions in Au, and Cu targets [91].

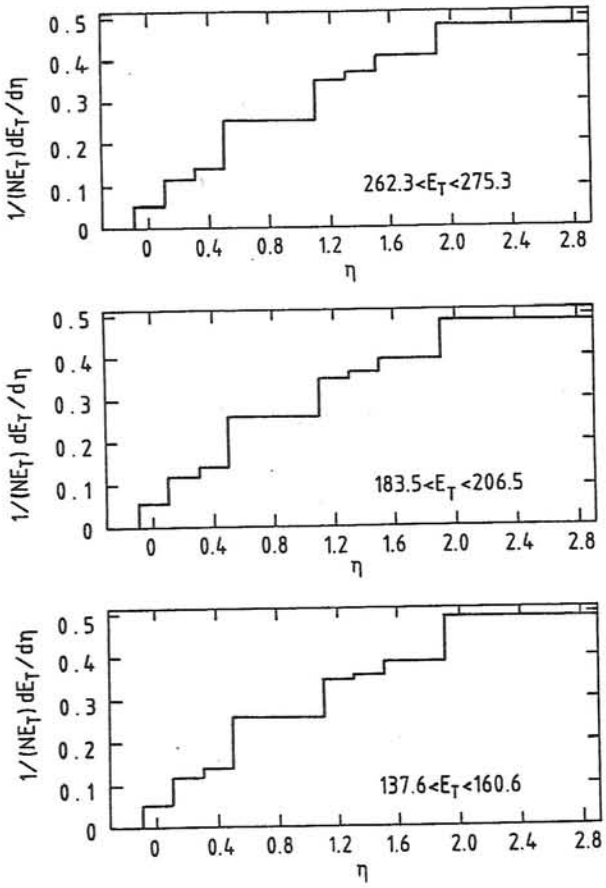

Fig. 39: NA34-Helios $dE_T/d\eta$ normalized by the integrated E_T in the acceptance $-0.1 < \eta < 2.9$ for $^{32}S + W$ at incident energy of 200 GeV/nucleon [100].

perhaps the $\bar{\nu} = 2.4$ for the emulsion [107] is not sufficiently large for the effect to be visible. The principal disagreement with the fireball model comes from the systematic increase of $\Delta\eta_{\rm FWHM}$ from 2.4 to 3.0 to 3.6 with increasing projectile energy, and the fact that all of these values are considerably wider than the universal fireball model prediction of 1.41, or 1.75.

A measurement of the pseudorapidity distribution was obtained by E802 from the small early setup with a 14.6 GeV/c per nucleon ^{16}O beam[91] (recall figure 28). Although the segmentation of the detector in η was rather crude, the transverse energy flow, $dE_T^0/d\eta$ could be obtained in four broad η intervals, for windows of total energy, $E_{\rm TOT}^0$, observed in the PbGl detector (see figure 38). The PbGl detector responds only to relativistic particles ($v/c > 0.8$), so these distributions should be directly comparable to the emulsion data in figure 37. The PbGl distributions are roughly gaussian with $\Delta\eta_{\rm FWHM} \simeq 2.0$ for the $^{16}O+Au$ and $^{16}O+Cu$ distributions, in agreement with the emulsion results. For peripheral collisions, $E_{\rm TOT}^0 < 10GeV$, the distributions are symmetric about y_{cm}^{NN}=1.7. For the Cu data, there is the hint of a shift backward of the peak for "central collisions", $E_{\rm TOT}^0 > 50GeV$, to 1.6. For the $^{16}O + Au$ data, the peak shifts steadily backwards with increasing centrality ($E_{\rm TOT}^0$), from ~ 1.6 at low values to ~ 1.4 for the most "central collisions". These data show that the flow in energy gets more transverse with increasing target atomic mass and with increasing observed total energy $E_{\rm TOT}^0$, particularly for the Au target. This is indicative that there is some, albeit small, effect of more than one collision of the projectile in the target nucleus, even at AGS energies.

At CERN, NA34 presented[51,100,108] a relatively comprehensive set of $dE_T/d\eta$ measurements, for fixed values of E_T in the range $-0.1 < \eta < 2.9$, for $p + Pb$, $^{16}O + W$ and for $^{32}S + W$ (see figure 39). These data are reasonably consistent with the characteristic shape from $p - p$ minimum bias collisions and with the emulsion data (recall figure 37). It is difficult to discern a difference in these distributions as a function of centrality (E_T) or projectile. The data at 200 GeV/nucleon appear to show $\Delta\eta_{\rm FWHM} \simeq 3.0$, and and appear to peak backwards of y_{cm}^{NN}; but it is difficult to make definitive conclusions about $\eta|_{\rm max}$ with this data. Measurements, with full pseudorapidity coverage, are expected in the near future.

13.3 A success—the relative endpoints of the E_T distributions

Although, the fireball model utterly fails to represent the shape of any of the pseudo-rapdity distributions shown above, the WA80 Collaboration presents their measurements of $dE_T/d\eta|_{\rm max}$ for central collisions of ^{16}O projectiles at 60 and 200 GeV/nucleon as a ratio to the fireball model prediction [101]. The "mid-rapidity energy stopping" ratio, $S_{\rm mid}$, was defined as the ratio of $dE_T^{\rm cent}/d\eta|_{\rm max}$, the measured value of the maximum in the pseudorapidity distribution for central collisions, to $T_{cm}^{fb}/2$ is the fireball model prediction. Amazingly, the fireball model prediction scaled out the target dependence very well, at both incident energies, and also scaled out the projectile dependence at 200 GeV/nucleon. The upper edges of the spectra for ^{16}O interactions in ^{27}Al, ^{64}Cu, ^{108}Ag, and ^{197}Au, could be simply characterized as $S_{mid} \simeq$35% (26%) at 60 (200) GeV/nucleon for all the targets. The fireball model prediction for the ratio of $dE_T^{cent}/d\eta|_{max}$ in $^{32}S + Au$ to $^{16}O + Au$ interactions is 1.77, which is close to the value observed by NA35[98], and not far from the values $\simeq$1.65 observed by NA34[100] and $\simeq$ 1.60 by WA80[101].

13.4 But it's probably just the Wounded Nucleon Model

The success of the fireball model in representing the target (and projectile) dependences of the upper edges of the E_T spectra is striking in comparison to its utter failure in representing the shape of the pseudorapidity distributions. This is probably because the target scaling and the projectile scaling in the fireball model correspond very closely to the the predictions of the Wounded Nucleon Model (WNM), in which E_T scales simply as the total number of participating nucleons. There are slight differences in the predictions because the WNM uses an $N-N$ absorption mean free path to calculate the number of participants, while the fireball model simply assumes that all the central nucleons interact. The WNM prediction for the ratio of the upper edges of the E_T spectra in $^{32}S+Au$ and $^{16}O+Au$ reactions is 1.77, the ratio of the number participants for central collisions. In the fireball model, the ratio of participants is 1.65, while the ratio of $T_{cm}^{fb}/2$ is 1.77. It is clear that a new level of systematic precision will have to be achieved by the experiments, before these fine distinctions in models can be sorted out.

14. Systematic Comparison of all experiments–a surprise

The discussion of pseudorapidity distributions suggests a systematic way to compare the E_T distributions from all the experiments. The NA34–Helios [51] definition is used to estimate E_T^{cent}, the E_T observed in "central collisions" (a factor of two in cross section down from the "knee" of the distribution), for all experiments. Then, the value of $dE_T^{cent}/d\eta|_{maz}$ at the maximum in the pseudorapidity distribution can be estimated[43]. The results are shown in figure 40, as a function of the nucleon-nucleon c.m.energy $\sqrt{s_{NN}}$ for $^{16}O+Au\,(W)$ reactions. The broken line on the figure is $dn/d\eta|_{y_{cm}^{NN}}$ for $p-p$ collisions [38] (recall figure 18). If geometry were the only nuclear effect, then the $\sqrt{s_{NN}}$ dependences would be identical in the $p-p$ and the $^{16}O+Au$ reactions. However, $dE_T^{cent}/d\eta|_{maz}$ in $^{16}O+Au$ increases by a factor of 3 from $\sqrt{s_{NN}}$= 5.4 to 19.4 GeV, which is much greater than the corresponding increase of a factor of 1.31 of the multiplicity density in $p-p$ collisions. The relative increase of $3/1.3=2.3$ is roughly equal to $(1+\bar{\nu})/2 \simeq 2.4$ for Au, which is consistent with the observation of "energy stopping" at the AGS, in contrast to the full "transparency", at $\sqrt{s_{NN}}=19.4$ GeV, where all the successive collisions in an Au nucleus are likely to be equally effective in producing transverse energy. Although, the estimates of E_T^{cent} are clearly dominated by systematic effects, the most notable being between the two NA35 measurements[6,98], a similar conclusion on the relative $\sqrt{s_{NN}}$ dependence of nucleus-nucleus and $p-p$ collisions can be drawn from the emulsion data[109] in figure 37. $dn/d\eta|_{maz}$ increases by a factor of 2.4 from $\sqrt{s_{NN}}$ =5.4 to 19.4 GeV, an increase of a factor of 1.8 relative to $p-p$, which is again close to the value of $(1+\bar{\nu})/2 \simeq 1.7$ for $AgBr$.

It is evident from these considerations, that systematic comparision of the data from nucleus-nucleus, $p+A$, and $p-p$ interactions at AGS and CERN energies can lead to quantitative conclusions, without detailed recourse to particular models.

15. Measurements of inclusive spectra of identified charged particles

The "energy stopping" observed at the AGS, may raise hopes that a baryon rich system has been created with a density approaching 3–5 times the normal nuclear density. The particle

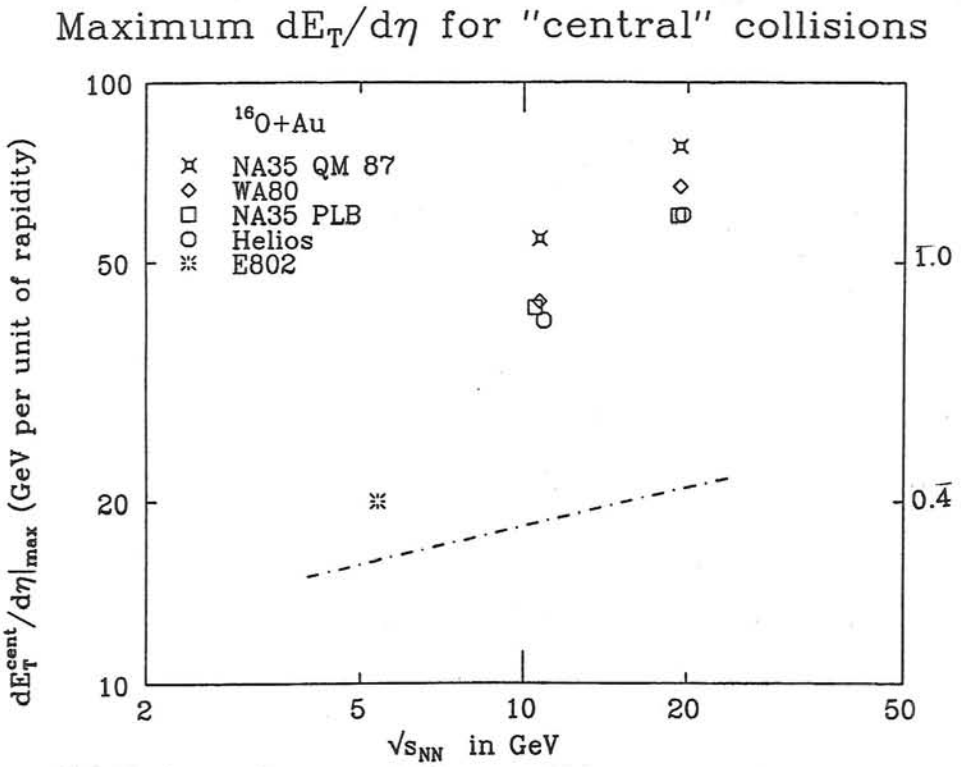

Fig. 40: Comparison of estimated [43] values at the maximum in the pseudorapidity distribution, $dE_T/d\eta|_{max}$, for central collisions, in all relativistic heavy ion experiments, plotted against nucleon-nucleon c.m. energy $\sqrt{s_{NN}}$. The broken line is $dn/d\eta|_{y_{cm}^{NN}}$ for $p-p$ collisions[38]

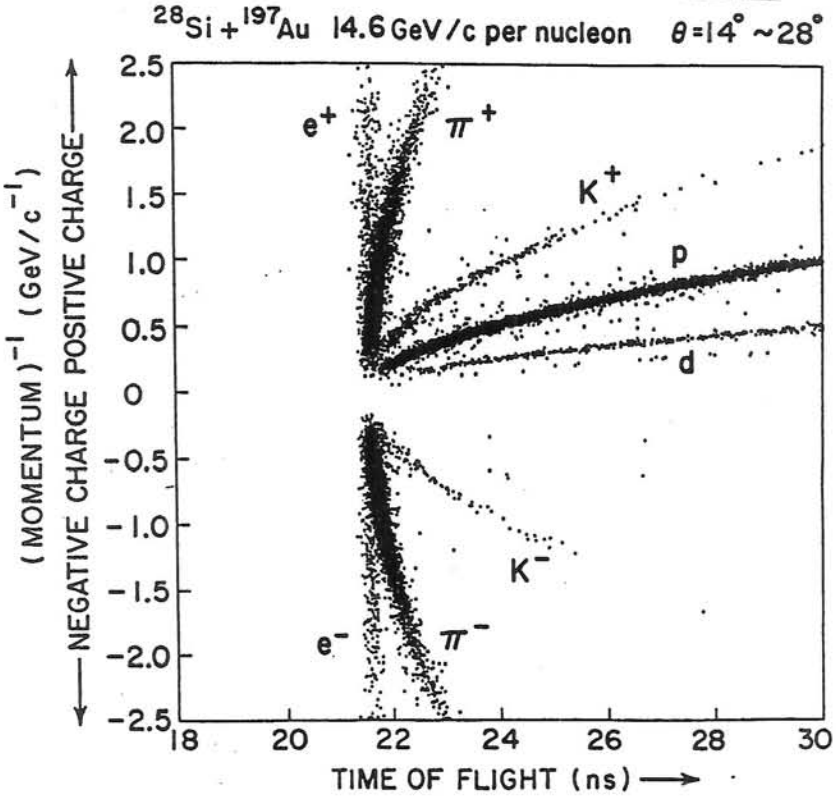

Fig. 41: Scatter plot of inverse momentum versus time of flight, for positively and negatively charged particles emitted from Si+Au interactions.

composition, particularly production of strange particles, has been proposed as a signature for the QGP[16,17]. Thus, a measurement of the particle composition and momentum spectra could provide essential input for understanding the reaction dynamics of nucleus-nucleus collisions in this stopping regime. The first results for momentum distributions of identified charged particles from such collisions in this energy regime have recently been obtained in the E802 magnetic spectrometer[96,110] (recall figure 12).

Semi–inclusive transverse momentum distributions of $\pi^{\pm}$, $K^{\pm}$, and p have been measured as a function of rapidity for central collisions (hence the **semi–inclusive** nomenclature) of 14.6 GeV/c per nucleon ^{28}Si with an ^{197}Au target of $\approx 3\%$ interaction length. The characterization of central collision events is obtained by requiring a high charged–particle multiplicity (upper 7% of the distribution) in the target–multiplicity array (TMA) $(-1.3 \leq \eta \leq 3.0)$.[91,96]

The experimental apparatus consists of a rotatable magnetic spectrometer with 25 msr solid angle, covering about 0.6 units of rapidity for pions at mid-rapidity at a given angle setting. Particle tracking is provided by 40 planes of projective drift chambers, divided evenly on each side of a bending magnet with a maximum integrated field of 1.5 Tm. The momentum resolution, which is limited by multiple scattering, is $\Delta P/P \leq 1.4\%$. Particle identification is provided by measuring particle flight time between a thin plastic scintillator beam counter (timing resolution σ=40 ps) and a 160 slat plastic scintillator array located behind the tracking system at 6.5 m from the target.[111] The quality of the particle identification is shown in the scatter plot (Fig. 41) of inverse momentum versus time–of–flight for charged particles at the pion mid–rapidity setting of the spectrometer. The combined timing resolution of 75 ps (1σ) provides adequate K–π separation up to 2.2 GeV/c. In this momentum range the mean separation between particle types is at least 5 times the σ for a given group. The only contamination of particle types occurs for the pions, for which there is a small contribution due to electrons. The electrons are completely separable up to $P = 0.7$ GeV/c; based on extrapolating the electron/pion ratio, the electron contamination at larger P is no greater than 5%.

15.1 Relativity really works!

In figure 41, the measured quantity $1/P$ is plotted against the measured time of flight (recall figure 15). The characteristic shape of the curves for the different particles is a pretty illustration of relativistic kinematics. Recall that the momentum of a particle of mass m is

$$P = \gamma\beta m \qquad \gamma = \frac{1}{\sqrt{1-\beta^2}}$$

The velocity is determined from the measured time of flight t over the known distance s

$$\beta = \frac{s}{ct}$$
$$t = \frac{s}{c}\left(\frac{1}{\beta}\right) \tag{15.1}$$

so that

$$\frac{1}{P} = \frac{\sqrt{\left(\frac{1}{\beta}\right)^2 - 1}}{m} = \frac{\sqrt{\left(\frac{c}{s}t\right)^2 - 1}}{m} \tag{15.2}$$

For low values of β (long times), the non-relativistic limit is obtained, and the relationship between momentum and velocity is linear: $1/P$ is linearly proportional to $(1/\beta)$, or to the time

t. For large values of $\beta \rightarrow 1$, the γ dependence takes over, and the linear dependence of $1/P$ on t curves over and becomes a square root dependence, for low values of t, as indicated in Eq. (15.2) and nicely shown in figure 41.

15.2 Results for the P_T spectra and $dn(y)/dy$

The compactness of the spectrometer allows a measurement of the kaon momentum spectra down to 0.5 GeV/c; below that, the fraction that survives decay is too small (~20%). Note that the fraction of kaons surviving after a proper time t_P (in the kaon rest frame), corresponding to $t = \gamma t_P$ in the lab system is

$$\mathcal{P}_{\text{surv}} = \exp -t_P/\tau = \exp -\frac{s}{c\tau}\left(\frac{1}{\gamma\beta}\right) = \exp -\left(\frac{s}{c}\frac{m}{P} \Big/ \tau\right) \tag{15.3}$$

where τ is the lifetime of the particle (as measured in its rest frame).

The track-reconstruction efficiency was determined from a manual reconstruction of 200 events and from Monte-Carlo simulations. The single particle position resolution of 150 μm (1σ) and pulse pair resolution of 2 mm, together with the large redundancy in the tracking system, allows a track reconstruction efficiency of 85±5%. This efficiency is only weakly dependent on multiplicity, namely a loss of ≤2.5% for each additional track for the observed range of multiplicities. At mid-rapidity, the average multiplicity in the spectrometer for events where there is at least one track is 1.5, with 99% of events having multiplicity ≤ 6. Decay and acceptance corrections have been performed on a track-by-track basis, assuming that a particle will be lost if it decays. Monte-Carlo calculations, however, indicate that some muons from pion decay will be mis-identified as pions, and thus be accepted as valid tracks. The inclusion of these particles in the pion spectra causes a negligible change in the slope of the pion momentum distribution and increases the pion integrated yield by no more than 10% from its correct value.

The measured momentum distributions for pions, kaons, and protons in the rapidity interval $1.2 < y < 1.4$ are shown in Fig. 42. The error estimates are statistical uncertainties only; there is no additional uncertainty in the relative normalization, but the overall normalization is uncertain to ±10%. The distributions are shown in terms of the invariant cross section, per trigger, as a function of the transverse kinetic energy $T_T = m_T - m_o$, where $m_T = \sqrt{P_T^2 + m_o^2}$ is the transverse mass, P_T is the transverse momentum, and m_o is the rest mass. For each rapidity interval, fits were performed using three possible types of distributions: $A_o exp(-m_T/T_o)$, the Boltzmann form $A_B\, m_T\, exp(-m_T/T_B)$, and $A_p exp(-P_T/T_p)$, where the parameters A and T are determined for each interval. As in $p-p$ collisions, the momentum distributions are found to be better described by exponentials in m_T than in p_T. The quality of the fits to the present data for all particle species is good for both the exponential and Boltzmann dependence on m_T. The best fit values of $T_o\,(MeV)$ for the "mid-rapidity" interval shown in figure 42 are: π^+ 162 ± 10, π^- 161 ± 10, K^+ 203 ± 15, K^- 175 ± 25, p 215 ± 5.

The measured values of T_o (or T_B) at mid-rapidity are similar for the different particle species, but progressively increase with the mass of the emitted particle: $T_o\,(\pi) \leq T_o\,(K^+) \leq T_o$(p). This order is different from the Bevalac results[112] with beams at 2.1 A·GeV/c, namely $T_o\,(\pi) \leq T_o$(p)$\leq T_o\,(K^+)$. For $p-p$ collisions at 12 GeV/c at mid-rapidity[35], $T_o\,(\pi)$ and T_o(p) are both equal to 150 MeV to within the 2% statistical uncertainty. The present data set, due

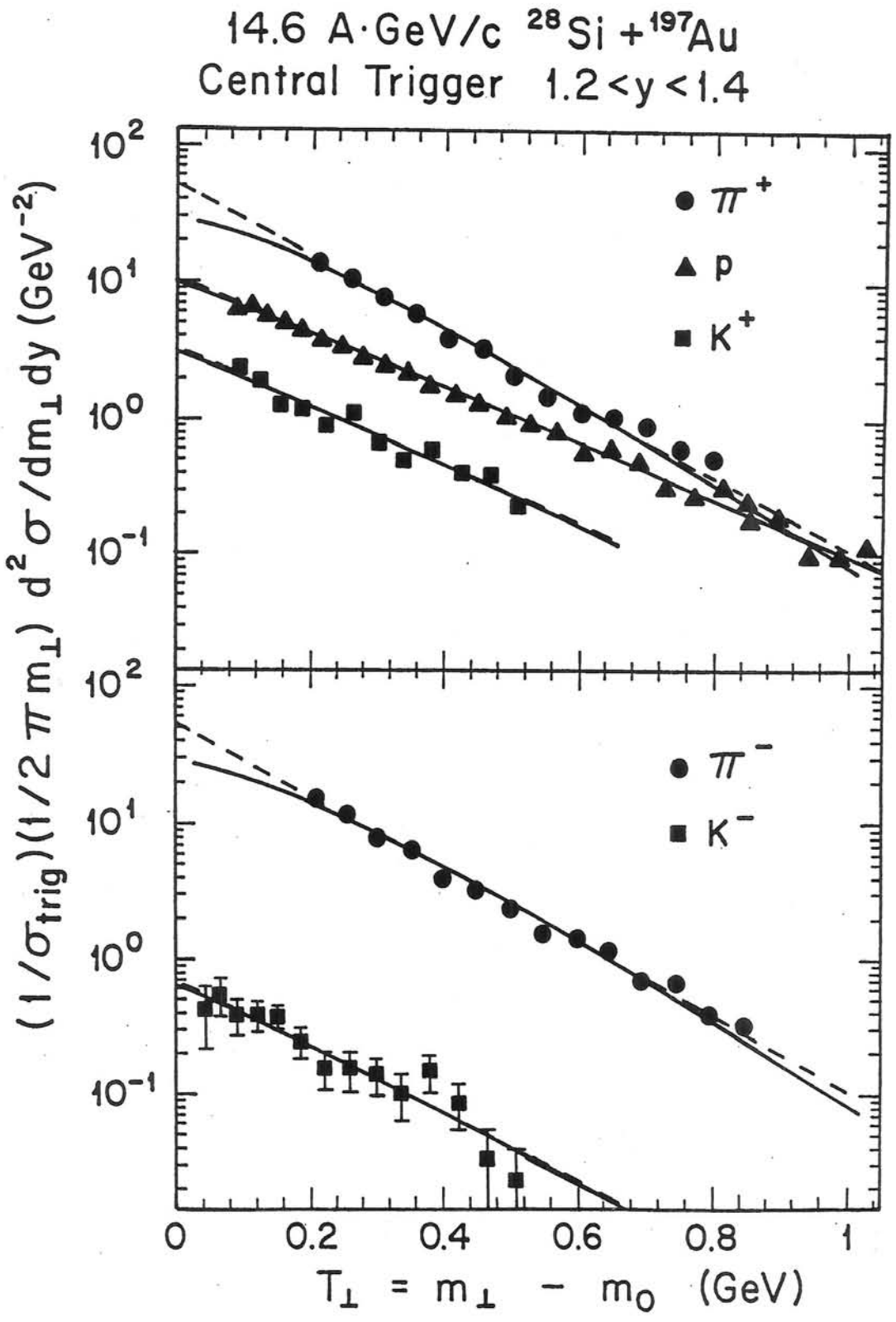

Fig. 42: Invariant cross section per central trigger as a function of $T_\perp$ for $\pi^\pm$, $K^\pm$, and protons for the rapidity interval $1.2 < y < 1.4$. The dashed lines show the exponential fits to the data; the solid curves show fits to Boltzmann distributions. The uncertainties in the data are either shown or are of the size of the drawn points.

to limited statistics, allows only a poor determination of the slope parameters for K^- and for only a limited range in y for K^+. The inverse slope parameters given above are obtained from fits to data in the same T_T range. If one wishes to compare the inverse slope parameters for fits to data in the same m_T range, then the extracted T_B (or T_o) values for the pions are increased by 10-20 MeV.

The rapidity dependences of T_o and T_B for π^- are shown in Fig. 43. The data appear to indicate a variation in inverse slope of about 40 MeV with y. However, the fits to the momentum distributions are made in different ranges of m_T for the different rapidity intervals, the range being shown in the upper panel of Fig. 43. It is estimated that a systematic change in slope of 10-20 MeV may occur over the rapidity range as a result of this restriction in m_T range. This restriction has the effect of decreasing the T_B (or T_o) in Fig. 43 at larger y. If the data were fit with the same m_T range for each rapidity interval, it would likely lead to a flatter rapidity distribution of the inverse slopes. For reference, indicated on Fig. 43 are two values of rapidity: y_{cm}^{NN}, the rapidity of the nucleon-nucleon c.m. system; and y_{cm}^{geom} i.e. $y_{cm}^{fb} = 1.25$, the rapidity of a system of $\approx$103 nucleon participants, composed of the incident Si and a core of 75 Au nucleons swept out by the Si nucleus in a head–on collision. **The Fireball Model strikes again!**

The rapidity distribution, dN/dy is obtained by integrating the transverse momentum distributions over m_T, using all 3 forms of the distribution to bound the systematic errors in the extrapolation. The values depend on the chosen method of extrapolation, but agree within $\pm$13%. The dN/dy distributions, obtained by integrating the Boltzmann form, are shown in Fig. 44 for protons, kaons and pions. The distributions for π^+ agree with those for π^- within the statistical uncertainty of 4% and are broadly peaked. The shape of the $\pi^\pm$ distribution also agrees very well with the $dE_T^0/d\eta$ distribution in the PbGl for central collisions in Au (recall figure 38). The distribution for protons rises dramatically near the target rapidity, consistent with the expected contribution of target spectator protons. By comparing the integrated spectra one also obtains the particle yield ratios. For the mid-rapidity interval $1.2 < y < 1.4$, the integrated ratios are 19.2$\pm$3% for K^+/π^+ and 3.6$\pm$0.8% for K^-/π^-, including the systematic error in the extrapolation to $T_T = 0$. These values are somewhat smaller than those given in a preliminary report[96]; the difference arises solely from the extrapolation to $T_T = 0$ used here, instead of the low p cutoff of 0.5 GeV/c used in the preliminary version[96].

The K^-/π^- ratio for p–p collisions at the same rapidity is $\approx$ 2.4$\pm$2.0%, the large uncertainty arising from the low yield of K^-. Because of this large uncertainty one cannot determine whether this ratio is different in heavy-ion collisions. The π^+/π^- ratio is 1.00 ± 0.04, whereas it is ≈ 1.6 for $p - p$ reactions[35]. This result presumably reflects the contribution of $n - n$ and $n - p$ interactions as well as $p - p$ interactions in $Si + Au$ interactions. The value for K^+/π^+ is much larger than the corresponding ratio of 4-8% measured in $p - p$ collisions[113]. Analysis of data for $p + A$ reactions indicates a K^+/π^+ ratio that is intermediate between the $p - p$ and $Si + Au$ results, albeit for a somewhat different kinematic range[113]. An enhancement of K^+ production, called the K^+ distillation effect[114], has been predicted to occur if either very high baryon density matter or a quark-gluon plasma is formed[16,17]. However, more mundane mechanisms are also possible. For example, the rescattering of the reaction products $\pi^+ n \rightarrow K^+ \Lambda$ could provide a mechanism for the K^+ enhancement[96,115].

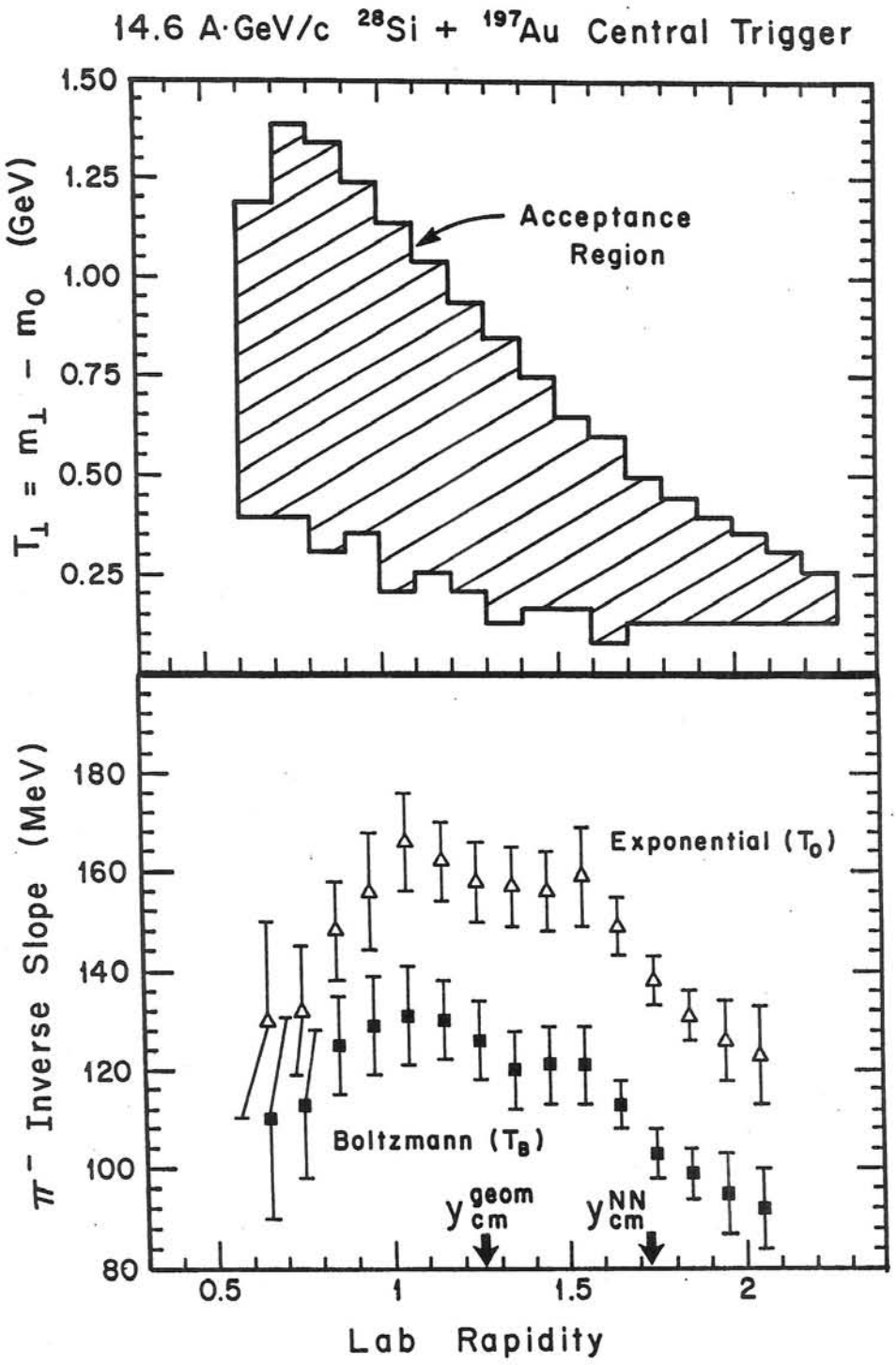

Fig. 43: The upper panel shows the range in $T_\perp$ for which the pion data are fitted to obtain inverse slope parameters in each rapidity interval. The lower panel shows the inverse slope parameters for the π^- distributions, for both exponential and Boltzmann distribution fits. The uncertainties include an estimate of the systematic errors. The participant c.m. rapidity $y^{geom}_{cm} = 1.25$ and nucleon-nucleon c.m. rapidity $y^{NN}_{cm} = 1.72$ are indicated.

15.3 The Fireball Model II— for single particle inclusive spectra

A simple prediction for the rapidity dependence of dn/dy is given by the single source Boltzmann distribution[116], a more elegant version of the fireball model. The solid curve on Fig. 44 is a fit to the pion distributions, with parameters $y_o = 1.46$ and $T = 125MeV$, where y_o is the rapidity of the thermal source with temperature T. For a thermal distribution one expects a common temperature T for all species of emitted particles, provided they freeze out at the same time. No such dependence is seen in the above data. A variety of possible mechanisms have, however, been proposed to postulate different effective temperatures for different species....

It is once again a useful exercise, to work out the predictions of the single source Boltzmann model for inclusive single particle distributions. Assume that particle emission is isotropic with a thermal distribution:

$$d^3n/dp^3 = \frac{C}{e^{(E-\mu)/T} \pm 1}$$

where the + sign is for particles which obey Fermi-Dirac statistics and the - sign for Bose-Einstein statistics. C is a constant and μ is called the chemical potential[116]. Usually, the limit of a Maxwell-Boltzmann distribution is taken:

$$d^3n/dp^3 = A\, e^{-E/T} \tag{15.4}$$

where $A = C\, e^{\mu/T}$ is taken as a constant for each particle species [117]. The total number of particles (of a given species), N, is obtained by integrating d^3n/dp^3 over all space and over all particle energies above the minimum energy for a given mass particle, $E = m$.

$$N = A \times 4\pi m^2 T\, K_2(m/T) \tag{15.5}$$

where K_2 is a Macdonald or modified Hankel function.

For single particle inclusive distributions, the fireball model gives distinctive predictions for the number of particles per unit rapidity and the "effective Temperature" as a function of rapidity. Starting with the non-invariant probability:

$$d^3n/dp^3 = A\, e^{-E/T}$$

the invariant probability is obtained by multiplying both sides of the equation by E:

$$E\, d^3n/dp^3 = A\, E\, e^{-E/T} \tag{15.6}$$

Expressed in terms of rapidity and m_T,

$$E = m_T \cosh y \qquad \text{and} \qquad d^3p = m_T\, dm_T\, dy d\phi$$

and the differential distribution is obtained:

$$\frac{E\, d^3n}{dp^3} = \frac{1}{2\pi}\frac{d^2n}{m_T dm_T dy} = A\, m_T \cosh(y - y_o)\, \exp\left(\frac{-m_T \cosh(y - y_o)}{T}\right) \tag{15.7}$$

where y_o is the rapidity of the fireball rest system. In simple terms, Eq. (15.7) says that the transverse momentum distribution at fixed rapidity has the form $E\, d^3n/dp^3 \simeq m_T\, e^{-m_T/T_B}$ where $T_B = T/\cosh(y - y_o)$. Thus, the fireball model predicts the form of the P_T distribution

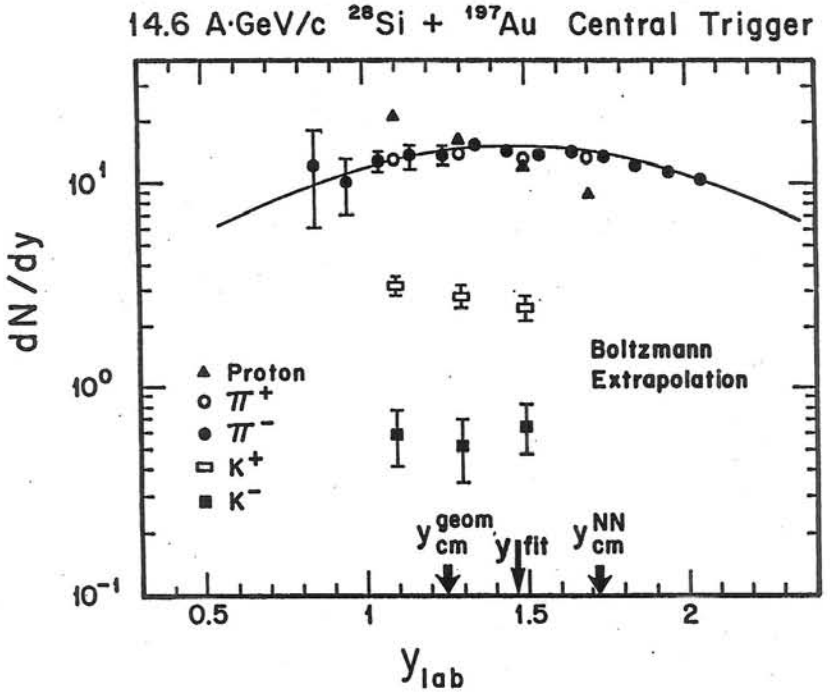

Fig. 44: Rapidity distributions dN/dy per trigger for $\pi^{\pm}$, $K^{\pm}$, and protons, assuming a Boltzmann form to extrapolate to $T_{\perp} = 0$. The errors shown are relative errors only; there is an overall uncertainty of $\pm 10\%$ due to the absolute normalization. The values for π^+ and π^- are the same within the measured uncertainties for all rapidity intervals. The solid curve shows the fit to Eq. (15.8), for a source located at y_{fit} =1.46 and $T = 125$ MeV.

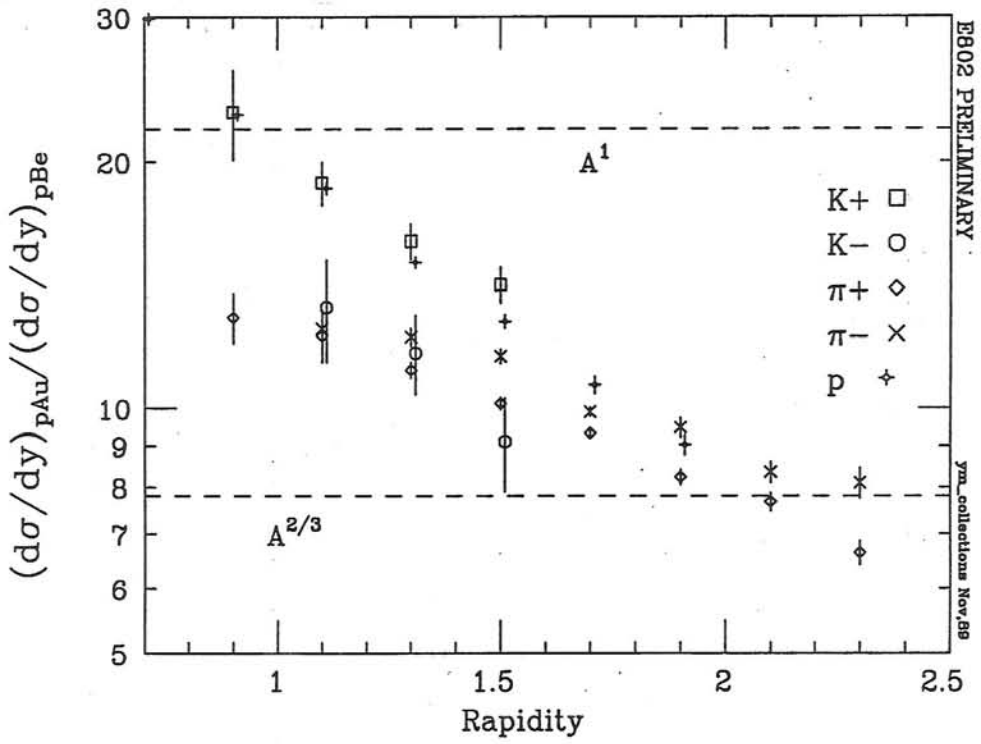

Fig. 45: Preliminary E802 results for the ratio of the inclusive cross sections (no central trigger) $d\sigma/dy$ as a function of rapidity for $p + ^{197}Au$ and $p + ^{9}Be$ reactions at 14.6 GeV/c.

and the variation of the effective temperature $T_B(y)$ with rapidity. Furthermore, the equation may be integrated over m_T to obtain dn/dy :

$$\frac{dn}{dy} = 4\pi\, A\, T\, e^{-m_o/T_B(y)}\, [T_B^2(y) + m_o\, T_B(y) + m_o^2/2] \tag{15.8}$$

where again,

$$T_B(y) = T/\cosh(y - y_o) \tag{15.9}$$

y_o is the rapidity of the thermal source of temperature T and m_o is the rest mass of the particle produced. The predicted variation of dn/dy with rapidity (Eq. (15.8))is slightly more complicated than that of the effective temperature $T_B(y)$. However, both should exhibit a maximum at the rapidity of the source y_o. Note also, that in the limit $m_0 \to 0$, $dn/dy \to dn/d\eta$ in agreement with the previous treatment Eq (13.11).

15.4 Further results on K^+/π^+

Preliminary results have recently been obtained in the E802 spectrometer from a run, in November 1988, with 14.6 GeV/c protons on a variety of nuclear targets. The ratio of the inclusive cross sections (no central trigger), $d\sigma/dy$, as a function of rapidity, has been measured for $p + ^{197}\,Au$ and $p + ^{9}\,Be$ reactions (see figure 45). Note that the inclusive cross section is plotted: thus, if dn/dy stayed the same for both reactions, the cross sections would be in the ratio $A^{2/3}$, as shown on the figure. The data for $\pi^{\pm}$ and K^- look rather similar to the ~100 GeV data[61] (recall figure 23). The ratio for protons increases dramatically toward the target, faster even than the ratio of the total number of target nucleons available. What is particularly surprising about the data is that the K^+ ratio exhibits nearly precisely the same dramatic increase toward the target as the protons, indicating a common origin for both K^+ and proton production. Could this, at last, be an indication of the importance of rescattering in the AGS energy range[96,115,118].

16. Conclusion

I have tried to leave the impression that this is a new and still dynamic field, with much ongoing activity and many unexplored facets. Regrettably, I have had to totally ignore many aspects of this broad field, one case in point being the effects of the large Z of relativistic heavy ions, the Coulomb reactions (the domain of E814[97] at the AGS), and another being identical particle Interferometry, already observed at CERN, and just now being seen in the large aperture E802 spectrometer.

The present round of experiments has been largely descriptive and exploratory, establishing the framework for understanding the interactions of Relativistic Heavy Ions. With the Au and Pb beams expected in 1992 at BNL and CERN, and with RHIC expected to be approved for construction in 1991, the future looks bright.

I find it particularly intriguing (and challenging) that **virtually all of the signatures of the QGP discussed above, have already been observed** in the first round of exploratory experiments. Naturally, I do not believe that the QGP has yet been discovered. In the case of the real QGP, all the signatures would have to turn on and turn off in a predictable, reproducible controllable and unified way. There is still much work to be done!

References

1. W.J. Willis in Proceedings of the XVI International Conference on High Energy Physics, Chicago-Batavia, Ill., USA, 1972, eds. J.D. Jackson and A. Roberts (NAL, Batavia, Ill. 1973), Vol. 4, pp 321-331. Note particularly the suggestion attributed to G. Cocconi on page 323 that "new states of matter might be produced when hadrons could be concentrated at high densities for a sufficiently long time".
2. Proceedings of the Sixth International Conference on Ultra-Relativistic Nucleus-Nucleus Collisions–Quark Matter 1987, eds. H. Satz et al., Z. Phys. C- Particles and Fields 38 (1988) 1; and previous proceedings in this series;
see also J.C. Collins and M.J. Perry, Phys. Rev. Lett. 34 (1975) 1353;
N. Cabibbo and G. Parisi, Phys. Lett. 59B (1975) 67.
3. R. Anishetty, P. Koehler and L. McLerran, Phys. Rev. D22 (1980) 2793.
4. U. Heinz et al., Phys. Rev. Lett. 58 (1987) 2292.
5. G. Baym and S.A. Chin, Phys. Lett. 62B (1976) 241;
G. Chapline and M. Nauenberg, Phys. Rev. D16 (1977) 450;
H.Satz, Ann. Rev. Nucl. Part. Sci. 35 (1985) 245.
6. NA 35 Collaboration, A. Bamberger et al., Phys. Lett. B184 (1987) 271.
7. W. Thomé et al., Nucl. Phys. B129 (1977) 365.
8. J. D. Bjorken, Phys. Rev. D27 (1983) 140.
9. P. Hut, Nucl. Phys. A418 (1984) 301c.
10. L. Van Hove, Nucl. Phys. A461 (1987) 3c.
11. L. Van Hove, Phys. Lett. 118B (1982) 138.
12. L. Van Hove, Z. Phys. C21 (1983) 93.
13. R. Hwa and K. Kajantie, Phys. Rev. D32 (1985) 1109;
K. Kajantie, J. Kapusta, L. McLerran and A. Mekjian Phys. Rev. D34 (1986) 2746.
14. G. Goldhaber, S. Goldhaber, W. Lee and A. Pais, Phys. Rev. 120 (1960) 300.
15. M. Gyulassy, Phys. Rev. Lett. 48 (1982) 454.
16. J. Rafelski and B. Muller, Phys. Rev. Lett. 48 (1982) 1066.
17. T. Matsui, B. Svetitsky and L. McLerran, Phys. Rev. D34 (1986) 2047.
18. T. Matsui and H. Satz, Phys. Lett. B178 (1986) 416.
19. W. M. Geist, Phys. Lett. B211 (1988) 233.
20. John. F. Donoghue and K. S. Sateesh, Phys. Rev. D38 (1988) 360.
21. A more complete treatment of this subject is found in the following references:;
Review of Particle Properties, Phys. Lett. B204 (1988);
Richard Fernow, *Introduction to experimental particle physics*, (Cambridge, 1989);
R. M. Sternheimer,*Methods of experimental physics*, ed. L. C. L. Yuan and C. S. Wu, (Academic Press, New York, 1963), vol. 5A, p 1.
22. Y. S. Tsai, Rev. Mod. Phys. 46 (1974) 815.
23. C. W. Fabjan and T. Ludlam, Ann. Rev. Nucl. Part. Sci. 32 (1982) 335.

24. R. M. Sternheimer, Phys. Rev. 99 (1955) 277.

25. L. Van Hove, preprint CERN-TH.4353/85, to be published in the Proceedings of the Neils Bohr Centenary Symposium, Copenhagen, 4-7 October 1985.

26. For example see A.H. Mueller in Proceedings of the XVI Int. Conf. on High Energy Physics, Chicago-Batavia, Ill., USA, 1972, eds. J.D. Jackson and A. Roberts (NAL, Batavia, IL 1973), Vol. 1, pp 347-388;
M. Jacob, ibid., Vol. 3, pp 373-458;
L. Van Hove, Phys. Reports 1C (1971) 347.

27. A.H. Mueller, Phys. Rev. D4 (1971) 150;
see also L. Caneschi, Nucl. Phys. B35 (1971) 406.

28. L. Foa, Phys. Reports 22 (1975) 1;
see also R. Panvini in Proceedings of the XVI Int. Conf. on High Energy Physics, Chicago-Batavia, Ill., USA, 1972, eds. J.D. Jackson and A. Roberts (NAL, Batavia, IL, 1973), Vol. 1, pp 330-346.

29. H. Bøggild and T. Ferbel Ann. Rev. Nucl. Part. Sci. 24 (1974) 451.

30. Z. Koba, H.B. Nielsen and P. Olesen, Nucl. Phys. B40 (1972) 317.

31. P. Slattery, Phys. Rev. D7 (1973) 2073.

32. F. Abe et al., Phys. Rev. Lett. 61 (1988) 1819.

33. e.g. see G. Giacomelli and M. Jacob, Phys. Repts. 55 (1979) 1;
P. Capiluppi et al., Nucl Phys B79 (1974) 189, ibid. B70 (1974) 1.

34. H. Bøggild, et al., Nucl Phys B57 (1973) 77.

35. V. Blobel, et al., Nucl Phys B69 (1974) 454.

36. For the flavor of the period, see Maurice Jacob's Eulogy for the ISR in CERN report 84-13, (CERN, SIS, Geneva 1984).

37. K. Guettler, et al., Nucl Phys B116 (1976) 77.

38. UA5 Collaboration, G.J. Alner et al., Z. Phys. C 33 (1986) 1.

39. T. Alexopoulos, et al., Phys. Rev. Lett. 60 (1988) 1622.

40. UA1 Collaboration, G. Arnison et al., Phys. Lett. 118B (1982) 167.

41. G.N. Fowler et al., Phys. Lett. 145B (1984) 407.

42. ABCDHW Collaboration, A. Breakstone et al., Phys. Lett. 132B (1983) 463.

43. M. J. Tannenbaum, Int. J. Mod. Phys. A. 4 (1989) 3377.

44. W.B. Fowler et al., Phys. Rev. 95 (1954) 1026. In the very early days it was not at all clear that a nucleon-nucleon collision could lead to the production of more than one meson;
See R.E. Marshak, *Meson Physics* (McGraw-Hill, New York,1952), chapter 8. Also see reference [45].

45. U. Camerini, W.O. Lock and D.H. Perkins in *Progress in Cosmic Ray Physics*, Volume I, ed. J.G. Wilson, (North-Holland, Amsterdam,1952), pp 1-34.

46. C. DeMarzo et al., Phys. Lett. 112B (1982) 173.

47. C. DeMarzo et al., Nucl. Phys. B211 (1983) 375.

48. UA1 Collaboration, G. Arnison et al., CERN-EP-82/122, presented to the XXI International Conference on High Energy Physics, Paris, 1982 (unpublished);
See also UA1 Collaboration, G. Arnison et al., Phys. Lett. 107B (1981) 320.

49. In detail the situation is somewhat more complicated. The many subtleties and details of "soft"physics [33] have been glossed over in this discussion but they do not change the essential relationship between E_T and multiplicity.

50. W. Ochs and L. Stodolsky, Phys. Lett. 69B (1977) 225;
H. Fesefeldt, W. Ochs and L. Stodolsky, Phys. Lett. 74B (1978) 389;
W. Ochs, Physica Scripta 19 (1979) 127.

51. HELIOS Collaboration, T. Åkesson et al., Z. Phys. C38 (1988) 383.

52. R. Wigmans, Nucl. Instrum. Meth. A259 (1987) 389.

53. AFS collaboration, H. Bøggild et al., CERN-EP-82/104, submitted to the XXI International Conference on High Energy Physics, Paris, 1982 (unpublished).

54. AFS Collaboration, H. Gordon et al., Phys. Rev. D28 (1983) 2736.

55. COR Collaboration, A.L.S. Angelis et al., Phys. Lett. 126B (1983) 132;
see also J. de Physique 43 (1982) C3-134, figure 8.

56. B.C. Brown et al., Phys. Rev. D29 (1984) 1895.

57. P.M. Fishbane and J.S. Trefil, Phys. Rev. D3 (1971) 238;
see also A. Dar and J. Vary, Phys. Rev. D6 (1972) 2412.

58. P.M. Fishbane and J.S. Trefil, Phys. Rev. D9 (1974) 168, Phys. Lett. 51B (1974) 139;
K. Gottfried, Phys. Rev. Lett 32 (1974) 957;
A.S. Goldhaber, Phys. Rev. D7 (1973) 765;
see also A. Białas and W. Czyż, Phys. Lett. 51B (1974) 179;
B. Andersson and I. Otterlund, Nucl. Phys. B88 (1975) 349.

59. J.E. Elias et al., Phys. Rev. D22 (1980) 13;
C. Halliwell et al., Phys. Rev. Lett. 24 (1977) 1499.

60. W. Busza et al., Phys. Rev. Lett. 34 (1975) 836.

61. C. De Marzo et al., Phys. Rev. D29 (1984) 2476; ibid. D26 (1982) 1019. Note that the streamer chamber and many of the collaborators are from the NA5 experiment, reference [46].

62. "Produced particles"are defined in reference [61] as the particles below 600 MeV/c which are not identified as protons, and all particles with momenta larger than 600 MeV/c. The produced particles are treated as pions.

63. A. Białas, A. Błeszynski and W. Czyż, Nucl. Phys. B111 (1976) 461.

64. R. Glauber in *Lectures in Theoretical Physics*, Volume I (1958), eds. W.E. Brittin and L.G. Dunham, (Interscience, New York, 1959), pp 315-414; R.J. Glauber in *High-Energy Physics and Nuclear Structure*, ed. S. Devons, (Plenum, New York, 1970)pp 207-264. See also R. Glauber and G. Matthiae, Nucl. Phys B21 (1970)123, and references therein.

65. AFS Collaboration, T. Åkesson et al., Phys. Lett. 119B (1982) 464.

66. H. Brody, S. Frankel, W. Frati and I. Otterlund, Phys. Rev. D28 (1983) 2334;
see also AFS collaboration, reference [54]; and B. Callen et al., Proc. Quark Matter 1984, ed. K. Kajantie (Springer, Berlin 1985), pp 133-142.

67. Dual Parton Model: see A. Capella and J. Tran Thanh Van, Z. Phys. C38 (1988) 177;
Also see: K. Werner, ibid. C38 (1988) 193;
J.P. Pansart, Nucl. Phys. A461 (1987) 521c;
J. Ranft, Phys. Lett. B188 (1987) 379.

68. Lund Model: see B. Andersson, G. Gustafson, B. Nilsson-Almqvist, Nucl. Phys. B281 (1979) 289;
Also see: B. Andersson, G. Gustafson, Z. Phys. C3 (1980) 223;
B. Andersson, G. Gustafson, G. Ingelman, T. Sjöstrand, Phys. Rep. 97 (1983)31.

69. A. Białas and E. Białas, Phys. Rev. D20 (1979) 2854;
A. Białas, W. Czyż and L. Lesniak, Phys. Rev. D25 (1982) 2328.

70. BCMOR Collaboration, A.L.S. Angelis et al., Phys. Lett. 168B (1986) 158; 141B (1984) 140;
see also, M.J. Tannenbaum et al., Proc. Quark Matter 1984, ed. K. Kajantie (Springer, Berlin 1985), pp 174-186.

71. T. Ochiai, Z. Phys. C35 (1987)209; Phys. Lett. B206 (1988) 535, and references therein.

72. J.H. Christenson, G.S. Hicks, L.M. Lederman, P.J. Limon, B.G. Pope and E. Zavattini, Phys. Rev. Lett. 25 (1970) 1523; Bull. Am. Phys. 15 (1970)579.

73. S.D. Drell and T-M. Yan, Phys. Rev. Lett. 25 (1970) 316.

74. J.W. Cronin et al., Phys. Rev. D11 (1975) 3105;
D. Antreasyan et al., Phys. Rev. D19 (1979) 764, and references therein.

75. J. Pumplin and E. Yen, Phys. Rev. D11 (1975) 1812;
P.M. Fishbane and J.S. Trefil, Phys. Rev. D12 (1975) 2113.

76. e.g. see BCMOR Collaboration, A.L.S. Angelis et al., Phys. Lett. B185 (1987) 213, and references therein.

77. M. Lev and B. Petersson, Z. Phys. C21 (1983) 155.

78. U.P. Sukhatme and G. Wilk, Phys. Rev. D25 (1980) 1978;
see also J.H. Kuhn, Phys. Rev. D13 (1976) 2948.

79. e.g. see S. Frankel and W. Frati, Nucl. Phys. B308 (1988) 699;
S.J. Brodsky and A.H. Mueller, Phys. Lett. B206 (1988) 685;
K. Werner, BNL-41500, to be published in Phys. Rev. D;
Y. Iga, R. Hamatsu, S. Yamazaki, H. Sumiyoshi, Z. Phys. C38 (1988) 557;
G. Gatoff, A.K. Kerman, and D. Vautherin, Phys. Rev. D38 (1988) 96;
A. Białas and M. Gyulassy, Nucl. Phys. B291 (1987) 793.

80. B. Brown et al., Phys. Rev. Lett. 50 (1983) 11;
AFLMPRW Collaboration, H.E. Miettinen et al., Nucl. Phys. A418 (1984) 315c;
see also C. Bromberg et al., Phys. Rev. Lett. 42 (1979) 1202.

81. M. J. Tannenbaum, in *Proceedings of Hadronic Matter in Collision*, Tucson, AZ, USA, 6-12 October 1988, ed. P. Carruthers, J. Rafelski (World Scientific, Singapore).

82. Recall that KNO scaling originally was defined as "scaling in the mean" of the charged multiplicity distribution as a function of c.m. energy $\sqrt{s}$. See reference [30] .

83. Note that the AFS collaboration, using a full hadron calorimeter, did not initially confirm the fit to a simple gamma distribution or the KNO scaling, but preferred the WNM fit to their data (see B. Callen et al. [66]). After extensive analysis of the energy response of the calorimeter, the corrected E_T spectra in $|\eta| \leq 0.7$ now fit the simple gamma distribution, and are relatively close to KNO scaling, with $p = 2.78 \pm 0.01$ for the $p-p$ data and $p = 2.48 \pm 0.08$ for the $\alpha - \alpha$ data [84] .

84. S. Frankel, in *Proceedings of Hadronic Matter in Collision*, Tucson, AZ, USA, 6-12 October 1988, ed. P. Carruthers, J. Rafelski (World Scientific, Singapore);
B.W. Callen, thesis, (Univ. of Pennsylvania, Philadelphia, PA, 1988).

85. UA5 Collaboration, G.J. Alner et al., Phys. Rep. 154 (1987) 247.

86. e.g. see M.A. Preston and R.K. Bhaduri, *Structure of the Nucleus* (Addison Wesley, Reading, MA, 1975).

87. Note that in the case of an asymmetric rapidity interval, the projectile and target can be assigned different weights, so that the deconvolution is ϵp and $(1-\epsilon)p$ for the projectile and target wounded nucleons respectively, where ϵ and $(1-\epsilon)$ are the fractions of the total energy contributed by the projectile and the target wounded nucleons in a given rapidity interval. Alternatively, more complicated algorithms can be used; e.g. see M. Kutschera, J. Hüfner and K. Werner, Phys. Lett. B192 (1987) 283. See also S. Frankel and W. Frati, reference [79] .

88. e.g. see A. Giovannini and L. Van Hove, Z. Phys. C30 (1986) 391;
P. Carruthers and C.C. Shih, Phys. Lett.165B (1985) 209, and references therein;
K. Fiałkowski, Phys. Lett. 169B (1986) 436;
see also P.A. Carruthers, M.Plümer, S. Raha and R.M. Weiner, Phys. Lett. B212 (1988) 369;
E.R. Nakamura and K. Kudo, ibid. 381.

89. C. De Marzo et al., Phys. Rev. D36 (1987) 8,16.

90. T.W. Ludlam, BNL Report 51921 (1985) 373.

91. eg. see M.J. Tannenbaum, Nucl. Phys. A488 (1988) 555c.

92. E802 Collaboration, T. Abbott et al., Phys. Lett. B197 (1987) 285.

93. E802 Collaboration, L.P. Remsberg, M.J. Tannenbaum et al., Z. Phys. C38 (1988) 35.

94. D.E. Alburger et al., Nucl. Instrum. Methods A254 (1987) 88.

95. A similar analysis for the NA35 data [6] was performed by J. Ftacnik et al., Phys. Lett. B188 (1987) 279.

96. E802 Collaboration, Y. Miake, G.S.F. Stephans, et al., Z. Phys. C38 (1988) 135;
See also E802 Collaboration, T. Abbott, et al., BNL-43459, Submitted to Nucl. Instr. and Meth. A (1989).

97. E814 Collaboration, P. Braun-Munzinger et al., Z. Phys C38 (1988) 45.

98. NA35 Collaboration, W. Heck et al., Z. Phys. C38 (1988) 19.

99. R. Anishetty, P. Koehler and L. McLerran, Phys. Rev. D22 (1980) 2793;
S. Date, M. Gyulassy and H. Sumiyoshi, Phys. Rev. D32 (1985) 619.

100. Helios Collaboration, T.Åkesson et al., CERN-EP/88-121, Phys. Lett. B214 (1988) 295.

101. WA80 Collaboration, S.P. Sorensen et al., Z. Phys. C38 (1988) 3, 51;
WA80 Collaboration, R. Albrecht et al., Phys. Lett. B199 (1987) 297.

102. P.V. Landshoff and J.C. Polkinghorne, Phys. Rev. D18 (1978) 3344.

103. WA80 Collaboration, G.R. Young et al., presented at the 7th International Conference on Ultra-Relativistic Nucleus-Nucleus Collisions (Quark Matter '88), September 1988, Lenox, Mass. To appear in the proceedings.

104. E802 Collaboration, E. Duek et al., "Projectile Energy Degradation at 14.5 GeV/u", submitted to 3rd International Conference on Nucleus-Nucleus Collisions, St. Malo, France, June 1988, (BNL-41447). See also reference [91] .

105. E802 Collaboration, M.J. Tannenbaum et al., Proceedings of the 23rd Rencontre de Moriond, *Current Issues in Hadron Physics*, ed. J. Tran Thanh Van, (Editions Frontieres, Gif-sur-Yvette, France, 1988).

106. Recall that $\cosh y = E/m_T$; and see also Frankel and Frati, reference [79] .

107. e.g. see W. Busza and R. Ledoux, Ann. Rev. Nucl. Part. Sci. 38 (1988) 119.

108. T. Åkesson et al., Z. Phys. C38 (1988) 397; see also Nucl. Phys. A447 (1985) 475c.

109. L.M. Barbier et al., Phys. Rev. Lett. 60 (1988) 405.

110. E802 Collaboration, T. Abbott, et al., submitted to Phys Rev Letters, (1989).

111. T. Sugitate et al. , Nucl. Inst. and Meth. A249 (1986) 354.

112. S. Nagamiya and M. Gyulassy, *Advances in Nuclear Physics*, (Plenum, New York, 1984), vol. 13, p. 201..

113. J. V. Allaby et al., CERN Preprint 70-12 (1970);
D. Dekkers et al., Phys. Rev. 137 (1965) B962;
U. Becker et al. , Phys. Rev. Lett. 37 (1976) 1731.

114. C. Greiner, D -H. Rischke,H. Stöcker, and P. Koch, Phys. Rev. D38 (1988) 2797.

115. R. Mattiello, H. Sorge, H. Stöcker and W. Greiner, Phys. Rev. Lett. 63 (1989) 1459.

116. S. Das Gupta and A. Z. Mekjian, Physics Reports 72 (1981) 131.

117. In principle, in a strict thermal model, C should be taken as a constant and the A parameters for the different particle species should vary according to their chemical potentials $A_i = C\, e^{\mu_i/T}$.

118. G. Baym, P. Braun-Munzinger and V. Ruuskanen, Phys. Lett. B190 (1987) 29;
A.D. Jackson and H. Bøggild, Nucl. Phys. A470 (1987) 669.